

# Multi-year simulations at kilometre scale with the Integrated Forecasting System coupled to FESOM2.5/NEMOv3.4

Thomas Rackow<sup>1,2</sup>, Xabier Pedruzo-Bagazgoitia<sup>1</sup>, Tobias Becker<sup>1</sup>, Sebastian Milinski<sup>1</sup>, Irina Sandu<sup>1</sup>, Razvan Aguridan<sup>1</sup>, Peter Bechtold<sup>1</sup>, Sebastian Beyer<sup>2</sup>, Jean Bidlot<sup>1</sup>, Souhail Boussetta<sup>1</sup>, Willem Deconinck<sup>1</sup>, Michail Diamantakis<sup>1</sup>, Peter Dueben<sup>1</sup>, Emanuel Dutra<sup>3</sup>, Richard Forbes<sup>1</sup>, Rohit Ghosh<sup>2</sup>, Helge F. Goessling<sup>2</sup>, Ioan Hadade<sup>1</sup>, Jan Hegewald<sup>4</sup>, Thomas Jung<sup>2,5</sup>, Sarah Keeley<sup>1</sup>, Lukas Kluff<sup>6</sup>, Nikolay Koldunov<sup>2</sup>, Aleksei Koldunov<sup>2</sup>, Tobias Kölling<sup>6</sup>, Josh Kousal<sup>1</sup>, Christian Kühnlein<sup>1</sup>, Pedro Maciel<sup>1</sup>, Kristian Mogensen<sup>1</sup>, Tiago Quintino<sup>1</sup>, Inna Polichtchouk<sup>1</sup>, Balthasar Reuter<sup>1</sup>, Domokos Sármany<sup>1</sup>, Patrick Scholz<sup>2</sup>, Dmitry Sidorenko<sup>2</sup>, Jan Streffing<sup>2</sup>, Birgit Sützl<sup>1</sup>, Daisuke Takasuka<sup>7,8</sup>, Steffen Tietsche<sup>1</sup>, Mirco Valentini<sup>1</sup>, Benoît Vannière<sup>1</sup>, Nils Wedi<sup>1</sup>, Lorenzo Zampieri<sup>9</sup>, and Florian Ziemer<sup>10</sup>

<sup>1</sup>European Centre for Medium-Range Weather Forecasts (ECMWF), Bonn, Germany; Reading, UK

<sup>2</sup>Alfred Wegener Institute, Helmholtz Centre for Polar and Marine Research (AWI), Bremerhaven, Germany

<sup>3</sup>Portuguese Weather Service (IPMA), Lisbon, Portugal

<sup>4</sup>Gauß-IT-Zentrum, Braunschweig University of Technology (GITZ), Braunschweig, Germany

<sup>5</sup>Department of Physics and Electrical Engineering, University of Bremen, Bremen, Germany

<sup>6</sup>Max-Planck-Institute for Meteorology (MPI-M), Hamburg, Germany

<sup>7</sup>Department of Geophysics, Tohoku University, Sendai, Japan

<sup>8</sup>Japan Agency for Marine-Earth Science and Technology (JAMSTEC), Yokohama, Japan

<sup>9</sup>Foundation Euro-Mediterranean Center on Climate Change (CMCC), Bologna, Italy

<sup>10</sup>Deutsches Klimarechenzentrum (DKRZ), Hamburg, Germany

*Correspondence to:* Thomas Rackow (thomas.rackow@ecmwf.int)

**Abstract.** We report on the first multi-year km-scale global coupled simulations using ECMWF’s Integrated Forecasting System (IFS) coupled to both the NEMO and FESOM ocean-sea ice models, as part of the H2020 Next Generation Earth Modelling Systems (nextGEMS) project. We focus mainly on an unprecedented IFS-FESOM coupled setup, with an atmospheric resolution of 4.4km and a spatially varying ocean resolution that reaches locally below 5km grid-spacing. A shorter coupled IFS-FESOM simulation with an atmospheric resolution of 2.8km has also been performed. A number of shortcomings in the original NWP-focused model configurations were identified and mitigated over several cycles collaboratively by the modelling centres, academia, and the wider nextGEMS community. The main improvements are (i) better conservation properties of the coupled model system in terms of water and energy budgets, which benefit also ECMWF’s operational 9 km IFS-NEMO model, (ii) a realistic top-of-the-atmosphere (TOA) radiation balance throughout the year, (iii) improved intense precipitation characteristics, and (iv) eddy-resolving features in large parts of the mid- and high-latitude oceans (finer than 5km grid-spacing) to resolve mesoscale eddies and sea ice leads. New developments at ECMWF for a better representation of snow and land use, including a dedicated scheme for urban areas, were also tested on multi-year timescales. We provide first examples of significant advances in the realism and thus opportunities of these km-scale simulations, such as a clear imprint of resolved Arctic sea ice leads on atmospheric temperature, impacts of km-scale urban areas on the diurnal temperature cycle in cities, and better propagation and symmetry characteristics of the Madden-Julian Oscillation.

## 36 **1 Introduction**

37 Current state-of-the-art climate models with typical spatial resolutions of 50-100km still rely heavily on parametrizations for  
38 under-resolved processes, such as deep convection, the effects of sub-grid orography and gravity waves in the atmosphere, or  
39 the effects of meso-scale eddies in the ocean. The emerging new generation of km-scale climate models can explicitly represent  
40 and combine several of these energy-redistributing small-scale processes and physical phenomena that were historically  
41 approximated or even neglected in coarse-resolution models (Palmer 2014). The advantage of km-scale models thus lies in  
42 their ability to more directly represent phenomena such as tropical cyclones (Judt et al. 2021) or the atmospheric response to  
43 small-scale features in the topography, e.g. mountains, orography gradients, lakes, urban areas, and cities. The distribution and  
44 intensity (and particularly the extremes) of precipitation (Judt and Rios-Berrios 2021), winds, and potentially also temperature  
45 will be different at improved spatial resolution. Importantly, features of deep convection start to be explicitly resolved at km-  
46 scale resolutions. This does not only improve the local representation of the diurnal cycle, convective organisation, and the  
47 propagation of convective storms (Prein et al., 2015; Satoh et al., 2019; Schär et al., 2020), but can also impact the large-scale  
48 circulation (Gao et al. 2023). Ultimately, the replacement of parametrizations by explicitly resolved atmospheric dynamics is  
49 also expected to narrow the still large uncertainty range of cloud-related feedbacks and thus climate sensitivity (Bony et al.  
50 2015; Stevens et al. 2016).

51  
52 Km-scale resolutions are also particularly beneficial for the ocean, where mesoscale ocean eddies (Frenger et al. 2013), leads  
53 opening up in the sea ice cover, and the response of oceanic heat transport to the presence of narrow canyons (Morrison et al.  
54 2020) can be studied directly. The small scales in the ocean, in particular mesoscale ocean eddies, have large-scale impacts on  
55 climate and control the distribution of nutrients, heat uptake, and carbon cycling (Hogg et al., 2015). Eddies also play an  
56 important role in the comprehensive response of the climate system to warming (Hewitt et al. 2022; Rackow et al. 2022,  
57 Griffies et al. 2015). In addition to the influence of mesoscale ocean features on the predictability of European weather  
58 downstream of the Gulf Stream area (Keeley et al., 2012), it has been proposed that higher-resolution simulations can enhance  
59 the representation of local heterogeneities in the sea-ice cover (Hutter et al., 2022). Via their impact on small-scale ocean  
60 features such as eddies, atmospheric storms can impact deep water formation in the Labrador Sea (Gutjahr et al. 2022), an  
61 ocean region of global significance because of its role in the meridional overturning circulation of the ocean. Coupled ocean-  
62 atmosphere variability patterns such as the El Nino-Southern Oscillation (ENSO), the largest signal of interannual variability  
63 on Earth, may also benefit from km-scale resolutions since ENSO-relevant ocean meso-scale features (Wengel et al. 2021) as  
64 well as westerly wind bursts should be better resolved.

65  
66 High-resolution simulations pose significant challenges in terms of numerical methods, data management, storage and analysis  
67 (Schär et al., 2020). To exploit the potential of km-scale modelling, it is essential to develop scalable models that can run  
68 efficiently on large supercomputers and take advantage of the next generation of exascale computing platforms (Bauer et al.,

69 2021, Taylor et al., 2023). Global atmosphere-only climate simulations at km-scale were pioneered by the NICAM group  
70 (Nonhydrostatic ICosahedral Atmospheric Model) almost two decades ago. On sub-seasonal to seasonal time scales, a global  
71 aqua-planet configuration at 3.5km resolution was performed (Tomita et al. 2005), and the MJO was realistically reproduced  
72 at 7km and 3.5km resolutions (Miura et al. 2007). In the last decade, the NICAM group as well as the European Centre for  
73 Medium-Range Weather Forecasts (ECMWF) ran simulations on climate time scales at around 10-15km spatial resolution. In  
74 particular, 14km resolution 30-year AMIP (Kodama et al. 2015) and HighResMIP simulations (Kodama et al. 2021) were  
75 performed with NICAM. During Project Athena, the climate and seasonal predictive skill of ECMWF's Integrated Forecasting  
76 System was analysed at resolutions up to 10km based on many 13 months simulations (totalling several decadal simulations),  
77 complemented with a 48-year AMIP-style simulation plus future time slices at 15km resolution (Jung et al. 2012). Recently,  
78 the NICAM group presented 10-year AMIP simulations at 3.5km using an updated NICAM version (Takasuka et al. 2024).  
79 Other modelling groups around the world have also increased their model resolution towards the km-scale, and many  
80 participated in the recent DYAMOND intercomparison project (DYnamics of the Atmospheric general circulation Modeled  
81 On Non-hydrostatic Domains) with a grid spacing as fine as 2.5km, simulations running over 40 days, and some of them  
82 already coupled to an ocean (Stevens et al., 2019).

83

84 While different modelling groups push global atmosphere-only simulations towards unprecedented resolutions (e.g. 220m  
85 resolution in short simulations with NICAM), another scientific frontier has emerged around running km-scale simulations on  
86 multi-year timescales, coupled to an equally refined ocean model. Indeed, in the last years, several km-scale simulations were  
87 run on up to monthly and seasonal timescales (Stevens et al., 2019, Wedi et al., 2020), but not many beyond these timescales,  
88 and not yet with a km-scale ocean (Miyakawa et al. 2017). This is due to the fact that even the most efficient high-resolution  
89 coupled models that are currently available require substantial computing resources to run, and the comprehensive and diverse  
90 code bases are also challenging to adapt to latest computing technologies. As a result, the number of simulations and  
91 realisations that can be performed is limited, making it difficult to calibrate and optimise the model settings. Coarser resolution  
92 models have been tuned for decades to be relatively reliable on the spatial scales that they can resolve, and to match the  
93 historical period well for which high-quality observations are available. Nevertheless, this is often achieved by compensating  
94 errors, which cannot necessarily be expected to work similarly in a warming climate. These models also have some long-  
95 standing biases that can locally be larger than the interannual variability or the climate change signal (Rackow et al. 2019,  
96 Palmer and Stevens, 2019). The lack of explicitly simulated small-scale features is one likely source for these long-standing  
97 biases in weather and climate models (Schär et al., 2020). Coarser resolution models also struggle with answering some  
98 important climate questions, such as the behaviour of extreme events in a warmer world and the impact of climate changes at  
99 the regional scale.

100

101 The European H2020 Next Generation Earth Modelling Systems (nextGEMS) project aims to build a new generation of eddy-  
102 and storm-resolving global coupled Earth System Models to be used for multi-decadal climate projections at km-scale. By

103 providing globally consistent information at scales where extreme events and the effects of climate change matter and are felt,  
104 global km-scale multi-decadal projections will support the increasing need to provide localised climate information to inform  
105 local adaptation measures. The nextGEMS models build upon models that are also operationally used for numerical weather  
106 prediction (NWP): ICON, which is jointly developed by DWD and MPI-M (Hohenegger et al., 2023), and the Integrated  
107 Forecasting System (IFS) of ECMWF, coupled to the NEMO and FESOM ocean models. NextGEMS revolves around a series  
108 of hackathons, in which the simulations performed with the two models are examined in detail by an international community  
109 of more than 100 participants, followed by new model development iterations or ‘Cycles’. The nextGEMS models have been  
110 (re-)designed for scalability and portability across different architectures (Satoh et al. 2019, Schulthess et al. 2019, Müller et  
111 al. 2019, Bauer et al. 2020, Bauer, Quintino, and Wedi 2022) and lay the foundation for the Climate Change Adaptation Digital  
112 Twin developed in the EU’s Destination Earth initiative (DestinE).

113

114 The operational NWP system at ECMWF uses an average 9km grid-spacing for the atmosphere coupled to an ocean at 0.25°  
115 spatial resolution (NEMO v3.4), which translates to a horizontal grid spacing of about 25km along the equator. While many  
116 coupled effects such as the atmosphere-ocean interactions during tropical cyclone conditions (Mogensen et al. 2017) can be  
117 realistically simulated at this resolution, ocean eddies in the mid latitudes are still only ‘permitted’ due to their decreasing size  
118 with latitude (Hallberg 2013). This setup is far from our goal to explicitly resolve mesoscale ocean eddies all around the globe  
119 (Sein et al., 2017). In this study, we therefore focus mainly on configurations in which km-scale versions of IFS (the main one  
120 at 4.4km grid spacing in the atmosphere and land) are coupled to the FESOM2.5 ocean-sea ice model at about 5km grid  
121 spacing, developed by the Alfred Wegener Institute, Helmholtz Centre for Polar and Marine Research (AWI). These  
122 configurations allow us to resolve many essential climate processes directly, for example mesoscale ocean eddies and sea ice  
123 leads in large parts of the mid- and high-latitude ocean, atmospheric storms, as well as certain small-scale features in the  
124 topography and land surface. We also test new developments of the IFS carried out in the last years at ECMWF to improve  
125 the representation of snow cover, land surface, and cities world-wide.

126

127 This paper documents the coupled km-scale model configurations with the Integrated Forecasting System in Section 2. The  
128 technical and scientific model improvements, carried out along the nextGEMS model development cycles based on feedback  
129 by the nextGEMS community, are presented in Section 3. A first set of emerging advances stemming from the km-scale  
130 character of the simulations is presented in Section 4, and more in-depth process studies will be the focus of dedicated future  
131 work. The paper closes with a summary and discussion of future steps in Section 5.



## 132 **2 Model configurations**

### 133 **2.1 The Integrated Forecasting System and its coupling to NEMO and FESOM**

134 The Integrated Forecasting System (IFS) is a spectral-transform atmospheric model with two-time-level semi-implicit, semi-  
135 Lagrangian time-stepping (Temperton et al., 2001; Hortal, 2002; Diamantakis and Váňa, 2022). It is coupled to other Earth  
136 System components (land, waves, ocean, sea-ice), and it is used in its version Cy48r1  
137 (<https://www.ecmwf.int/en/publications/ifs-documentation>, last access 26 March 2024), which has been used for operational  
138 forecasts at ECMWF since July 2023 (plus modifications that will be detailed in this study). In its operational configuration  
139 (‘oper’), the atmospheric component is coupled to the NEMO v3.4 ocean model. The octahedral reduced Gaussian grid (short  
140 ‘octahedral grid’) with a cubic (spectral) truncation (TCo) is used in the IFS (Malardel et al., 2016). The cubic truncation with  
141 the TCo grid implies higher effective resolution and better efficiency than the former linear truncation. It acts as a numerical  
142 filter without the need for expensive de-aliasing procedures, requires little diffusion, and produces small total mass  
143 conservation errors for medium-range forecasts; see Wedi 2014; Wedi et al. 2015; Malardel et al., 2016 for further discussion.  
144 A hybrid, pressure-based vertical coordinate is used which is a monotonic function of pressure and depends on the surface  
145 pressure (Simmons and Strüfing, 1983). The vertical coordinate follows the terrain at the lowest level and relaxes to a pure  
146 pressure-level vertical coordinate system in the upper part of the atmosphere. The vertical discretization scheme is a finite  
147 element method using cubic B-spline basis functions (Vivoda et al., 2018, Untch and Hortal, 2004).

148  
149 The atmosphere component of the IFS has a full range of parametrizations described in detail in ECMWF (2023a,b). The moist  
150 convection parameterization, originally described in Tiedtke (1989), is based on the mass-flux approach, and represents deep,  
151 shallow and mid-level convection. For deep convection the mass-flux is determined by removing a modified Convective  
152 Available Potential Energy (CAPE) over a given time scale (Bechtold et al., 2008, 2014), taking into account an additional  
153 dependence on total moisture convergence and a grid resolution dependent scaling factor to reduce the cloud base mass flux  
154 further at grid resolutions higher than 9km (Becker et al., 2021). The sub-grid cloud and precipitation microphysics scheme is  
155 based on Tiedtke (1993) and has since been substantially upgraded with separate prognostic variables for cloud water, cloud  
156 ice, rain, snow and cloud fraction, and an improved parametrization of microphysical processes (Forbes et al. 2011; Forbes  
157 and Ahlgrimm, 2014). The parametrization of sub-grid turbulent mixing follows the Eddy-Diffusivity Mass-Flux (EDMF)  
158 framework, with a K-diffusion turbulence closure and a mass-flux component to represent the non-local eddy fluxes in unstable  
159 boundary layers (Siebesma et al., 2007; Kohler et al., 2011). The orographic gravity wave drag is parametrized following Lott  
160 and Miller (1997) and Beljaars et al. (2004) and a non-orographic gravity wave drag parametrization is described in Orr et al.  
161 (2010). The radiation scheme is described in Hogan and Bozzo (2018, ecRad). Full radiation computations are calculated on a  
162 coarser grid every hour with approximate updates for radiation-surface interactions every timestep at the model resolution.

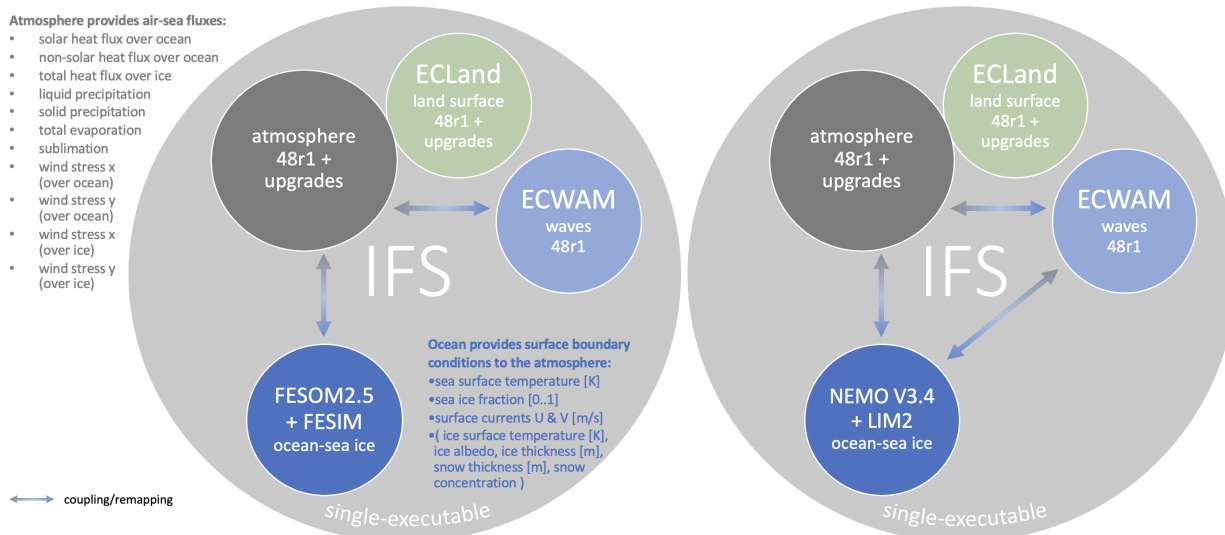
163

164 The IFS land model ECLand (Bousetta et al. 2021) runs on the model grid and is fully coupled to the atmosphere through an  
165 implicit flux solver. ECLand represents the surface processes that interact with the atmosphere in the form of fluxes. The  
166 ECLand version in this work contains among others, a 4-layer soil scheme, a lake model, an urban model, a simple vegetation  
167 model, a multi-layer snow scheme, and a vast range of global maps describing the surface characteristics. A wave model  
168 component is provided by ecWAM to account for sea state dependent processes in the IFS (ECMWF, 2023c). The wave model  
169 runs on a reduced lat-lon  $0.125^\circ$  grid, 36 frequencies, and 36 directions. This means that the distance between latitudes is  
170  $0.125^\circ$ , and the number of points per latitude is reduced polewards in order to keep the actual distance between grid points  
171 roughly equal to the spacing between two consecutive latitudes. The frequency discretisation is such that ocean waves with  
172 periods between 1 and 28 seconds are represented.

173  
174 For the purpose of nextGEMS and other related projects such as the DestinE Climate Change Adaptation Digital Twin, where  
175 also an IFS-NEMO configuration with a  $1/12$  degree ocean (NEMO v4) is applied, the complementary IFS-FESOM model  
176 option was developed. We coupled the Finite Volume Sea ice-Ocean Model FESOM2 (Danilov et al. 2017, Scholz et al. 2019,  
177 Koldunov et al. 2019, Sidorenko et al. 2019) to IFS (see details below). Instead of using a coupler for this task, as for the  
178 OpenIFS-FESOM (Streffing et al. 2022), the alternative adopted here is to follow the strategy for IFS-NEMO coupling, where  
179 the ocean and IFS models are integrated into a single executable and share a common time stepping loop (Mogensen, Keeley,  
180 and Towers, 2012). In this sequential coupling approach (akin to the model physics-dynamics and land-surface coupling that  
181 occurs every model timestep), the atmosphere advances for 1 hour (length of the coupling interval) and fluxes are passed as  
182 upper boundary condition to the ocean, which then in turn advances for 1 hour, up to the same checkpoint. The following  
183 atmospheric step then uses updated surface ocean fields as lower boundary condition for the next coupling interval (Mogensen,  
184 Keeley, and Towers, 2012). Note that there is no need to introduce a lag of one coupling timestep because the ocean and  
185 atmosphere models run sequentially and not overlapping in parallel. A study into the effect of model lag on flux/state  
186 convergence by Marti et al. (2021) found that sequential instead of parallel coupling reduces the error nearly to the fully  
187 converged solution.

188  
189 In the operational IFS, in areas where sea ice is present in the ocean model, currently a sea ice thickness of 1.5m and no snow  
190 cover are assumed for the computation of the conductive heat flux on the atmospheric side. Our initial implementation for the  
191 multi-year simulations carried out in nextGEMS does not divert yet from this assumption of the operational configuration, in  
192 which the atmosphere ‘sees’ only the sea-ice fraction computed by the ocean/sea-ice model. There are more consistent options  
193 available to couple the simulated sea ice albedo, ice surface temperature, ice and snow thickness from the ocean models to the  
194 atmospheric component (Mogensen, Keeley, and Towers, 2012) and those will also be considered in future setups.

195



196

197

**Figure 1: Coupling of the Integrated Forecasting System (IFS) components in (left) IFS-FESOM and (right) IFS-NEMO in nextGEMS configurations.** Coupling between the unstructured FESOM grid and the Gaussian grid of the atmosphere is via pre-prepared remapping weights in SCRIP format (Jones 1999). Direct coupling between the surface wave model (ECWAM) and the ocean is at the moment only implemented in IFS-NEMO; in IFS-FESOM, the ocean and waves interact only indirectly via the atmosphere. ECWAM and the atmosphere have their own set of remapping weights for direct coupling, while ECLand and the atmosphere are more closely coupled to each other.

203

204

205

The oceans provide surface boundary conditions to the atmosphere (sea surface temperature, sea ice concentration, zonal and meridional surface currents) while the atmospheric component provides air-sea fluxes to the ocean models (as listed in Fig. 1). The exchange between the different model grids is implemented as a Gaussian distance-weighted interpolation for both directions. Since the implementation accepts any weight files as long as they are provided in SCRIP format (Jones 1999), future setups will explore other interpolation strategies, such as the use of conservative remapping weights for the air-sea fluxes to ensure better flux conservation. River runoff for the ocean models is taken from climatology; for IFS-FESOM, the runoff from the COREv2 (Large and Yeager 2009) flux dataset is applied based on Dai et al. (2009).

212

In order to couple FESOM with IFS, the existing single-executable coupling interface (i.e. the set of Fortran subroutines) between IFS and NEMO (Mogensen, Keeley, and Towers, 2012) has been extracted and newly implemented directly in the FESOM source code (Rackow et al. 2023c). From the perspective of the atmospheric component, after linking, FESOM and NEMO thus appear to IFS virtually identical in terms of provided fields and functionality in forecast runs with IFS. Clear gaps and differences to the operational configuration with NEMO v3.4 remain in terms of ocean data assimilation capabilities (NEMOVAR), ocean initial condition generation, and missing surface ocean-wave coupling (Fig. 1). However, these

216

217

218 differences do not critically impact the multi-year simulations for nextGEMS described in this study or multi-decadal  
219 simulations planned for nextGEMS and DestinE.

## 220 **2.2 Performed nextGEMS runs and Cycles**

221 The nextGEMS project relies on several model development cycles, in which the high-res models are run and improved based  
222 on community feedback from the analysis of successive runs. In an initial set of km-scale coupled simulations (termed ‘Cycle  
223 1’), the models were integrated for 75 days, starting on 20 January 2020 (Table 1). For Cycle 1, ECMWF’s IFS in Cy47r3  
224 (Cy46r1 for IFS-FESOM) has been run at 9km (TCo1279 in Gaussian octahedral grid notation) and 4.4km (TCo2559) global  
225 spatial resolution. The runs at 9km were performed with the deep convection parametrization, while at 4.4km, the IFS was run  
226 with and without the deep convection parametrization. The underlying ocean models NEMO and FESOM2.1 had been run on  
227 an eddy-permitting  $0.25^\circ$  resolution grid in this initial model cycle (ORCA025 for NEMO and a triangulated version of this  
228 for FESOM, tORCA025). Based on the analysis by project partners during a hackathon organised in Berlin in October 2021,  
229 several key issues were identified both in the runs with IFS, and in those run with ICON (Hohenegger et al. 2023).

230 As will be detailed below, the IFS has been significantly improved for the longer ‘Cycle 2’ simulations based on IFS Cy47r3  
231 (IFS nextGEMS Cycle 2 4.4km 1-year simulation, <https://dx.doi.org/10.21957/1n36-qg55>; Wieners et al., 2023), where a  
232 2.8km simulation (TCo3999) has also been performed. For the purpose of nextGEMS Cycle 2 and 3, an ocean grid with up to  
233 5km resolution (‘NG5’) has been introduced for the FESOM model, which is eddy-resolving in most parts of the global ocean  
234 (see Appendix B). The NG5 ocean has been spun up for a duration of 5 years in stand-alone mode, with ERA5 atmospheric  
235 forcing (Hersbach et al. 2020) until 20 January 2020. In contrast, NEMO performs active data assimilation to estimate ocean  
236 initial conditions for 20 January 2020.

237 Based on feedback from the 2nd hackathon in Vienna in 2022, ‘Cycle 3’ simulations based on IFS Cy48r1 for the 3rd hackathon  
238 in Madrid (June 2023) have been further improved. The ocean has been updated to FESOM2.5 (Rackow et al, 2023c), and run  
239 coupled for up to 5 years (see Fig. 2 for an example wind speed snapshot at 4.4km resolution). In Section 3, we will detail the  
240 series of scientific improvements in the atmosphere, ocean, and land components of IFS-NEMO/FESOM that were performed  
241 to address the identified key issues, and how these successive steps result in a better representation of the coupled physical  
242 system.

243  
244 **Table 1: nextGEMS configurations of the IFS and coupled simulations analysed in this study.** The Gaussian octahedral  
245 grid notations TCo1279, TCo2559, and TCo3999 refer to 9km, 4.4km, and 2.8km global atmospheric spatial resolution,  
246 respectively. The simulations were performed with constant greenhouse gas forcing from the year 2020 ( $\text{CO}_2 = 413.72$  ppmv,  
247  $\text{CH}_4 = 1914.28$  ppbv,  $\text{N}_2\text{O} = 331.80$  ppbv,  $\text{CFC}_{11} = 857.38$  pptv,  $\text{CFC}_{12} = 497.10$  pptv), prognostic ozone, no volcanic  
248 aerosols, and the CAMS aerosol climatology (Bozzo et al. 2020).

<b>Configuration</b>	<b>Atmospheric spatial resolution</b>	<b>Ocean model settings and spatial resolution</b>	<b>Length of simulations</b>
IFS-NEMO, TCo1279 ('oper')  Cycle 3, 2, 1	9km	NEMO V3.4, ORCA025 (0.25° 3-polar grid)	5 years (Cycle 3) 2 years (Cycle 2) 75 days (Cycle 1)
IFS-FESOM, TCo1279-NG5  Cycle 3	9km	FESOM2.5, NG5 grid (3-4km in high-res regions; 13km in tropics)	1 year (Cycle 3)
IFS-FESOM, TCo3999-NG5  Cycle 2	2.8km	FESOM2.1, NG5 grid (3-4km in high-res regions; 13km in tropics)	8 months (Cycle 2)
IFS-FESOM, TCo2559-NG5  Cycle 3 & 2	4.4km	FESOM2.1/2.5, NG5 grid (3-4km in high-res regions; 13km in tropics)	5 years (Cycle 3) 1 year (Cycle 2)

249 **2.3 Technical refactoring for the FESOM2.5 ocean-sea ice model code**

250 Prior to the start of nextGEMS, FESOM had been fully MPI-parallelised only and was shown to scale well on processor counts  
251 beyond 100,000 (Koldunov et al. 2019). In order to fully support hybrid MPI-OpenMP parallelization in the single-executable  
252 framework with IFS, numerous non-iterative loops in the ocean model code were rewritten with release of FESOM version  
253 2.5. The FESOM model has been significantly refactored also in other aspects over the last years to support coupling with IFS.  
254 In the single executable coupled system, the IFS initializes the MPI communicator (Mogensen, Keeley, and Towers, 2012)  
255 and passes it to the ocean model for initialisation of FESOM. In particular, FESOM's main routine has been split into 3 cleanly  
256 defined steps, namely the initialisation, time stepping, and finalisation steps. This was a necessary step for the current single-  
257 executable coupled model strategy at ECMWF, where the ocean is called and controlled from within the atmospheric model.  
258 The single-executable configuration is a necessary condition for coupled data assimilation at ECMWF. The adopted strategy  
259 means that some IFS-NEMO developments can be directly applied also to IFS-FESOM configurations. Similar to what is done

260 for the wave and atmosphere components of the IFS, we implemented a fast “memory dump” restart mechanism for FESOM.  
261 This has the advantage that the whole coupled model can be quickly restarted as long as the parallel distribution (number of  
262 MPI tasks and OpenMP processes) does not change during the simulation.

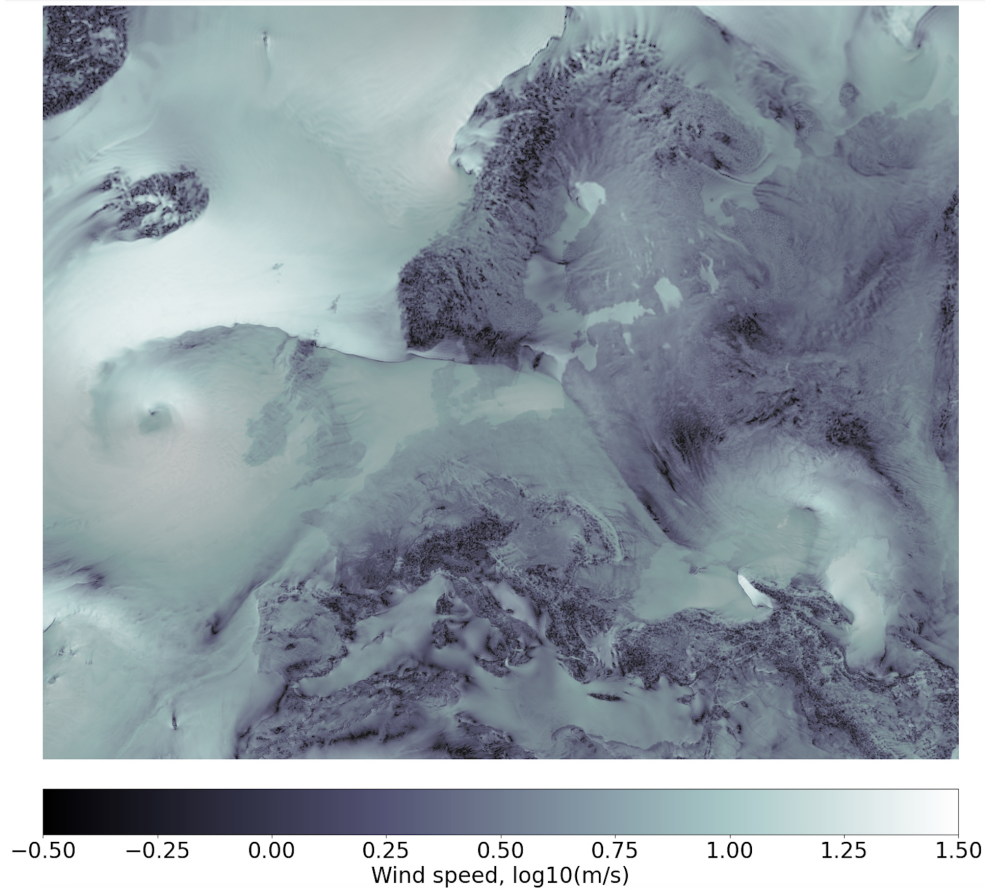
## 263 **2.4 Model output and online diagnostics**

264 One of the concerns for the scientific evaluation of multi-year high-resolution simulations is the need to read large volumes of  
265 output from the global parallel filesystem. This is required for certain processing tasks, such as the computation of monthly  
266 averages in a climate context and regridding to regular meshes, so that the relevant information can be easily analysed and  
267 visualised. One way to mitigate this burden is to move these computations closer to where the data is produced and process  
268 the data in memory. Many of these computations are currently not possible in the IFS code, so starting in Cycle 3 we used  
269 MultIO (Sármány et al., 2023), a set of software libraries that provide, among other functionalities, user-programmable  
270 processing pipelines that operate on model output directly. IFS has its own Fortran-based I/O-server that is responsible for  
271 aggregating geographically distributed three-dimensional information and creating layers of horizontal two-dimensional fields.  
272 It passes these pre-aggregated fields directly to MultIO for the on-the-fly computation of temporal means and data regridding.  
273 One of the key benefits of this approach is that with the in-memory computation of, for example, monthly statistics, the  
274 requirement of storage space may be reduced significantly. Higher-frequency data may only be required for the computation  
275 of these statistics and as such would not need to be written to disk at all. For the nextGEMS runs in this study, however, the  
276 decision was taken to make use of MultIO mostly for user-convenience, i.e. to produce post-processed output in addition to  
277 the native high-frequency output. The computational overhead associated with this (approximately 15% in this case) is more  
278 than offset by the increased productivity gained from much faster and easier evaluation of high-resolution climate output,  
279 particularly in the context of hackathons with a large number of participants. As a result, the MultIO pipelines have been  
280 configured to support the following five groups of output:

- 281
- 282 • Hourly or six-hourly output (depending on variable) on native octahedral grids.
- 283 • Hourly or six-hourly output (depending on variable), interpolated to regular (coarser) meshes for ease of data analysis.  
284 The MultIO configuration uses parts of the functionality of the Meteorological Interpolation and Regridding package  
285 (MIR), ECMWF’s open-source re-gridding software, to be able to execute this in memory.
- 286 • Monthly means for all output variables on native grids.
- 287 • Monthly means for all output variables on regular (coarser) meshes, interpolated by MultIO calling MIR.
- 288 • All fields are encoded or re-encoded in GRIB by MultIO calling ECCODES, an open-source encoding library.
- 289

290 At the end of each pipeline, all data are streamed to disk, more specifically to the Fields DataBase (FDB, Smart et al., 2017),  
291 an indexed domain-specific object store for archival and retrieval – according to a well-defined schema – of meteorological  
292 and climate data. This mirrors the operational setup at ECMWF. For the nextGEMS hackathons, all simulations and their

293 GRIB data in the corresponding FDBs have been made available in Jupyter notebooks (Kluyver et al. 2016) via intake catalogs  
294 (<https://intake.readthedocs.io/en/latest/>, last access 25 March 2024) using gribscan. The gribscan tools scans GRIB files and  
295 creates Zarr-compatible indices (Kölling, Klufft, and Rackow, 2024).  
296



297  
298 **Figure 2: Wind speed snapshot over Europe as simulated by the IFS with a 4.4km spatial resolution in the atmosphere.**  
299 The wind speed map is overlaid with a map of the zonal wind component in a grey-scale colormap for further shading, which  
300 is made partly transparent. The figure does not explicitly plot land. Nevertheless, the high-resolution simulation clearly exposes  
301 the continental land masses and orographic details due to larger surface friction and hence smaller wind speeds (darker areas  
302 depict lower wind speeds). The image is a reproduction with Cycle 3 data of the award winning entry by N. Koldunov for  
303 2022's Helmholtz Scientific Imaging Contest, [https://helmholtz-imaging.de/about\\_us/overview/index\\_eng.html](https://helmholtz-imaging.de/about_us/overview/index_eng.html).

### 304 **3 Model developments for multi-year coupled km-scale IFS simulations**

305 This section details model developments for the atmosphere (3.1), ocean, sea ice, and wave (3.2), and land (3.3) components  
306 of IFS-FESOM/NEMO in the different cycles of nextGEMS. Following a short overview of identified key issues and  
307 developments at the beginning of each section, we present how those successive development steps translate to a better  
308 representation of the coupled physical system.

#### 309 **3.1 Atmosphere**

##### 310 **3.1.1 Key issues and model developments**

###### 311 **Water and energy imbalances**

312 At the first nextGEMS hackathon, large water and energy imbalances were identified as key issues in the Cycle 1 simulations,  
313 which led to large biases in the top-of-atmosphere (TOA) radiation balance. If run for longer than the 75 days of Cycle 1, e.g.  
314 multiple years, this would lead to a strong drift in global mean 2m temperature. Analysis confirmed that most of the energy  
315 imbalance in the IFS was related to water non-conservation, and that this issue gets worse (i) when spatial resolution is  
316 increased, and (ii) when the parametrization of deep convection is switched off (hereafter ‘Deep Off’). This is because the  
317 semi-Lagrangian advection scheme used in the IFS is not conserving the mass of advected tracers, e.g. the water species (see  
318 Appendix A). However, while this issue was acknowledged to be detrimental for the accuracy of climate integrations, so far it  
319 was thought that it was small enough to not significantly affect the quality of numerical weather forecasts, which span  
320 timescales ranging from a few hours to seasons ahead. To address the problem of water non-conservation in the IFS, a tracer  
321 global mass fixer was activated for all prognostic hydrometeors (cloud liquid, ice, rain and snow) in nextGEMS Cycle 2, as  
322 well as water vapour (for more details, see Appendix A describing the mass-fixer approach). The tracer mass fixer ensures  
323 global mass conservation, but it cannot guarantee local mass conservation. However, it estimates where the mass conservation  
324 errors are larger and inserts larger corrections in such regions, which is often beneficial for local mass conservation and  
325 accuracy (see Diamantakis and Agusti-Panareda, 2017). When adding tracer mass fixers to a simulation, the computational  
326 cost increases by a few percentage points (typically less than 5%). Water and energy conservation in Cycle 1 versus Cycle 2  
327 is discussed in Section 3.1.2.

###### 328 **Top-of-atmosphere radiation balance**

329 To reduce drift in global mean surface temperature, it is essential that the global top-of-atmosphere (TOA) radiation imbalance  
330 is small. In the nextGEMS Cycle 2 simulation at 4.4 km resolution coupled to FESOM2.1 (Table 1), the TOA net imbalance,  
331 relative to observed fluxes from the CERES-EBAF product (Loeb et al. 2018), had been about  $+3 \text{ Wm}^{-2}$  (positive values  
332 indicate downward fluxes), resulting from a  $+5 \text{ Wm}^{-2}$  shortwave imbalance that was partly balanced by a  $-2 \text{ Wm}^{-2}$  longwave  
333 imbalance. Because of anthropogenic greenhouse gas emissions, CERES shows a  $+1 \text{ Wm}^{-2}$  imbalance. Due to the larger TOA  
334 imbalance, the nextGEMS Cycle 2 simulations warmed too much, by about 1K over the course of one year (see Section 3.1.3).



335 Thus, addressing the TOA radiation imbalance was a major development focus in preparation for the 5-year integration in  
336 nextGEMS Cycle 3.

337 On top of IFS 48r1, in Cycle 3 we used a combination of model changes targeting a reduced TOA radiation imbalance, mostly  
338 affecting cloud amount. Changes that increased the fraction of low clouds are (i) a change restricting the detrainment of mid-  
339 level convection to the liquid phase, (ii) a reduction of cloud edge erosion following Fielding et al. (2020) and (iii) a reduction  
340 of the cloud inhomogeneity, which increases cloud amount as it reduces the rate of accretion. This change is in line with  
341 nextGEMS's km-scale resolutions as cloud inhomogeneity is expected to be smaller at high resolutions. High clouds were  
342 increased in areas with strong deep convective activity by (iv) decreasing a threshold that limits the minimum size of ice  
343 effective radius, in agreement with observational evidence and (v) changing from cubic to linear interpolation for the departure  
344 point interpolation of the Semi-Lagrangian advection scheme for all moist species except water vapour. The resulting TOA  
345 balance in Cycle 3 is discussed in Section 3.1.3.

### 346 **Representation of intense precipitation and convective cells**

347 Precipitation has many important roles in the climate system. It is not only important for the water cycle over land and ocean,  
348 but also provides a source of energy to the atmosphere, as heat is released when water vapour condensates and rain forms,  
349 which balances radiative cooling. Precipitation is also often associated with meso-scale or large-scale vertical motion and the  
350 corresponding overturning circulation is crucial for the horizontal and vertical redistribution of moisture and energy within the  
351 atmosphere.

352 In km-scale simulations in which the deep convection parametrization is switched off (e.g, Cycle 2 at 4.4 km and 2.8 km  
353 resolution), convective cells tend to be too localised, too intense, and they lack organisation into larger convective systems  
354 (e.g, Crook et al., 2017, Becker et al., 2021). The tropical troposphere also gets too warm and too dry, and these mean biases  
355 as well as biases that concern the characteristics of meso-scale organisation of convection also affect the larger scales, for  
356 instance zonal mean precipitation and the associated large-scale circulation. For example, with deep convection  
357 parametrization off in Cycle 2 (Deep Off), the ITCZ often organises into a continuous and persistent line of deep convection  
358 over the Pacific at 5°N (see Fig. D1 in Appendix D), and the zonal mean precipitation at 5°N is strongly overestimated.

359 To address these issues, instead of switching the deep convection scheme off completely, we have reduced its activity by  
360 reducing the cloud-base mass flux in Cycle 3. The cloud-base mass flux is the key ingredient of the convective closure, and  
361 depends on the convective adjustment time scale  $\tau$ , which assures a transition to resolved convection at high resolution via an  
362 empirical scaling function that depends on the grid spacing (discussed in more detail in Becker et al., 2021). To significantly  
363 reduce the activity of the deep convection scheme in Cycle 3, we use the value of the empirical scaling function that is by  
364 default used at 700m resolution (TCo15999) already at 4.4 km resolution (TCo2559), which corresponds to a reduction of the  
365 empirical value that determines the cloud base mass flux by a factor of 6 compared to its value at 9 km resolution. Precipitation  
366 characteristics in Cycle 3 vs Cycle 2 are discussed in Section 3.1.4.

367

### 368 3.1.2 Improvements of mass and energy conservation in Cycle 2 vs Cycle 1

369 To address the water non-conservation mentioned in Section 3.1.1, tracer mass fixers for all moist species were introduced in  
 370 Cycle 2. Figure 3 shows that the Cycle 1 simulations with the IFS have an artificial source of water in the atmosphere. This  
 371 artificial source is responsible for 4.6% of total precipitation in the 9 km simulation with deep convection parametrization  
 372 switched on (hereafter ‘Deep On’), which is also used for ECMWF’s operational high-resolution ten-day forecasts, and for  
 373 10.7% at 4.4 km with Deep Off. Further analysis after the hackathon by the modelling teams at ECMWF has shown that about  
 374 50% of the artificial atmospheric water source is created as water vapour. The additional water vapour not only affects the  
 375 radiation energy budget of the atmosphere, but it can also cause energy non-conservation when heat is released through  
 376 condensation. The other 50% of water is created as cloud liquid, cloud ice, rain or snow. This is related to the higher-order  
 377 interpolation in the semi-Lagrangian advection scheme introduced for cloud liquid, cloud ice, rain and snow in IFS Cycle 47r3,  
 378 which can result in spurious maxima and minima, including negative values, which are then clipped to remain physical. It  
 379 turns out that the spurious minima are in excess of the spurious maxima and by clipping them, the mass of cloud liquid, cloud  
 380 ice, rain and snow is effectively increased. When activating global tracer mass fixers, global water non-conservation is  
 381 essentially eliminated (about 0.1%) in the Cycle 2 simulations (Figure 3).

382

383 On a global scale, the total energy budget of the atmosphere can be defined as

$$\begin{aligned}
 384 \quad & \frac{c_{pd}}{g} \int_{p_{surf}}^0 \frac{dT}{dt} dp_h + \frac{L_{v0}}{g} \int_{p_{surf}}^0 \frac{dq_v}{dt} dp_h - \frac{L_{s0} - L_{v0}}{g} \int_{p_{surf}}^0 \frac{dq_i + dq_s}{dt} dp_h + \int_{p_{surf}}^0 \frac{dKE}{dt} dp_h \\
 385 \quad & = F_s + F_q - F_{rad}^{top} + F_{rad}^{surf} + (L_{s0} - L_{v0})P_s,
 \end{aligned}$$

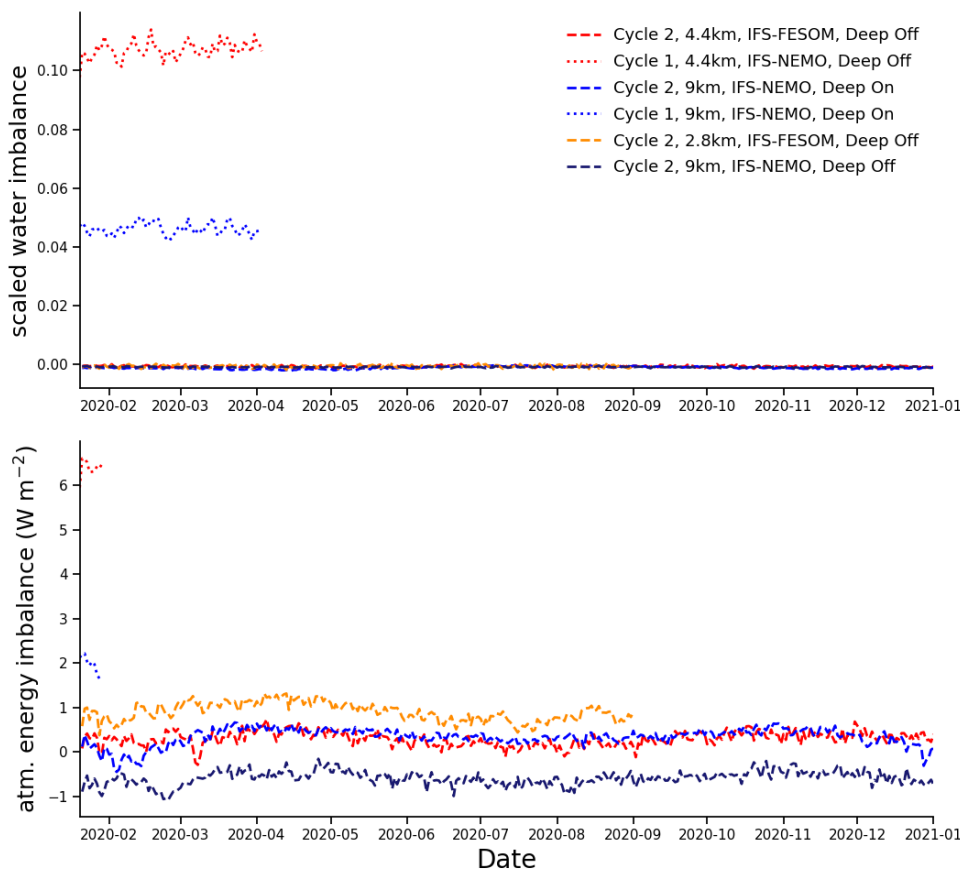
386 (equation 1), where  $T$  is temperature,  $q_v$ ,  $q_i$  and  $q_s$  are water vapour, cloud ice and snow. Together, these terms describe the  
 387 change in vertically-integrated frozen moist static energy over time, while the last term on the left-hand-side of the equation is  
 388 the change in vertically-integrated kinetic energy ( $KE$ ). Sources and sinks of the atmosphere’s total energy are  $F_s$  and  $F_q$ , which  
 389 are the surface turbulent sensible and latent heat fluxes,  $F_{rad}^{top}$  and  $F_{rad}^{surf}$ , which are the TOA and surface net radiative  
 390 shortwave and longwave fluxes, and  $(L_{s0}-L_{v0})P_s$  is the energy required to melt snow at the surface. Note that dissipation is not  
 391 a source or sink of total energy.

392

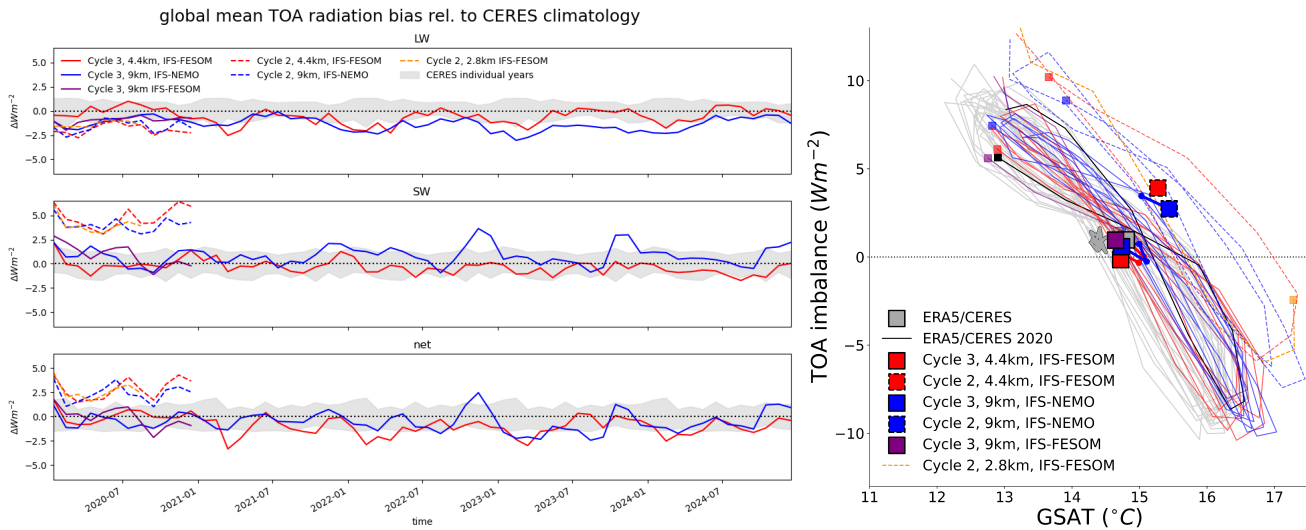
393 Using this equation to calculate the global energy budget imbalance in Figure 3, the Cycle 1 simulation with 9 km resolution  
 394 has an atmospheric energy imbalance of  $2.0 \text{ Wm}^{-2}$ , and this imbalance increased to  $6.4 \text{ Wm}^{-2}$  at 4.4 km resolution with Deep  
 395 Off. In Cycle 2, the energy budget imbalance due to the mass conservation of water species is substantially smaller, having  
 396 reduced to less than  $1 \text{ Wm}^{-2}$ . This remaining imbalance can be related to the explicit and semi-implicit dynamics because they  
 397 are still non-conserving, for example causing an error in surface pressure, as well as the mass fixers. The remaining imbalance  
 398 could be removed by adding a total energy fixer to the model.

399

400 As a result of activating the tracer mass fixers for all moist species, the overestimate of mean precipitation reduces and the  
 401 troposphere gets slightly colder and drier. While these changes are dominated on climate time scales by the effects that energy  
 402 conservation has on global mean temperature, they can have a significant impact on time scales of numerical weather  
 403 prediction. Indeed, the discussed setup with improved water and energy conservation is part of ECMWF’s recent operational  
 404 IFS upgrade in June 2023 (48r1) because it improves the skill scores of the operational weather forecasts (ECMWF Newsletter  
 405 172, 2022).  
 406



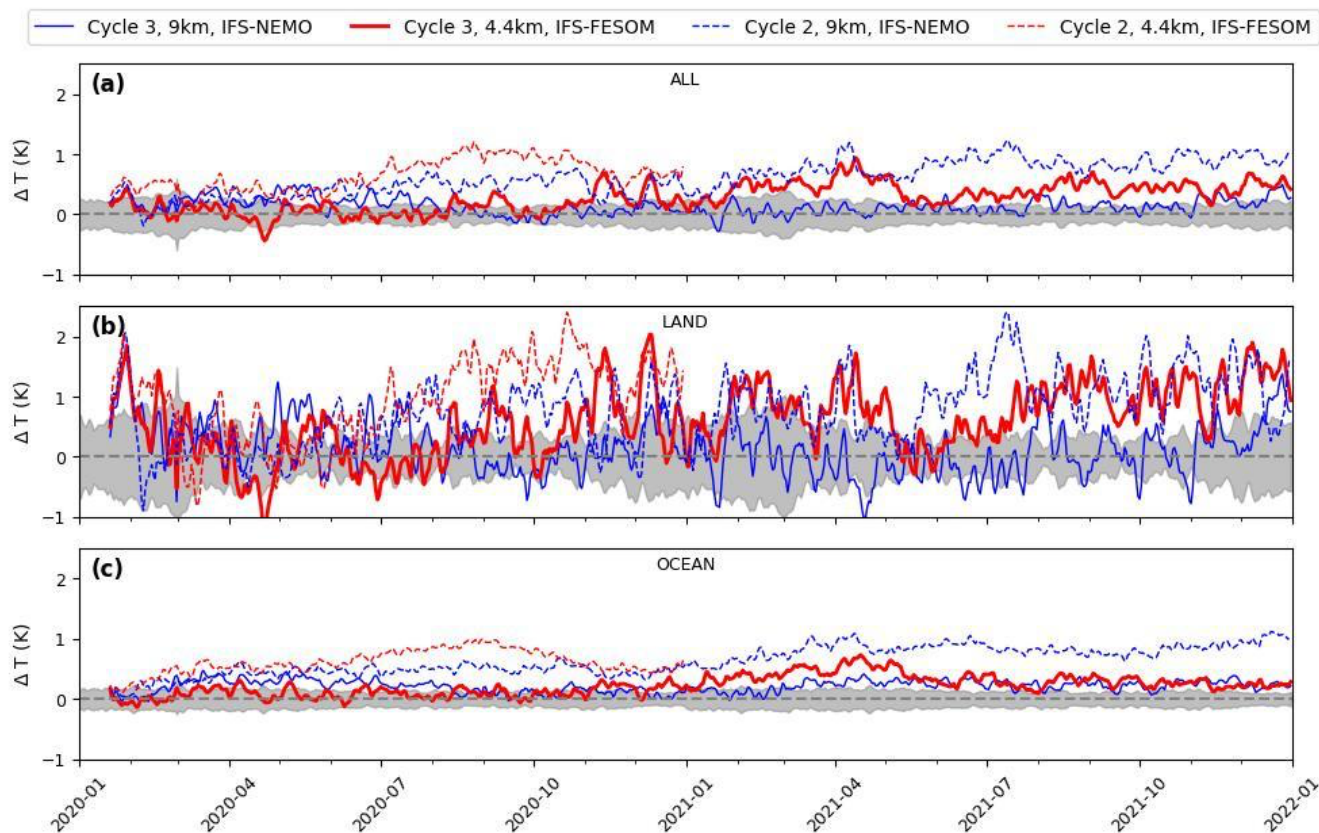
407  
 408 **Figure 3: Daily mean water non-conservation (left) and daily-mean atmospheric energy imbalance (right), as a function**  
 409 **of lead time for Cycle 1 and Cycle 2 simulations.** Water non-conservation is computed as the daily change in globally  
 410 integrated total water, taking account of surface evaporation and precipitation, as a fraction of the daily precipitation. The  
 411 atmospheric energy imbalance is calculated with Equation 1.  
 412



414  
 415 **Figure 4: Global-mean TOA radiation deviation from the CERES climatology in the 5-year-long nextGEMS**  
 416 **simulations and global-mean TOA imbalance as function of global-mean surface air temperature (GSAT).** a) Grey  
 417 shading shows the climatological range of individual CERES years. Due to the free-running nature of the nextGEMS  
 418 simulations, variations within the grey envelope are to be expected even in the absence of any bias. b) Grey lines show the  
 419 climatological range of individual CERES years (2001–2020) over ERA5 GSAT data (Hersbach et al. 2020). Thin lines are  
 420 tracing monthly mean values with a small square marking the final month for each simulation. Big squares depict annual means  
 421 (dashed for Cycle 2, solid for Cycle 3) and for multi-year simulations thick solid lines are tracing annual means for each year  
 422 with the big square marking the last simulated annual mean.

423  
 424 Due to the model changes detailed in Section 3.1.1, the nextGEMS Cycle 3 simulations with the IFS have at all resolutions a  
 425 TOA radiation imbalance that is within observational uncertainty, with respect to the net, shortwave and longwave fluxes  
 426 (Figure 4). This is not only true for the annual mean value, but also for the annual cycle of TOA imbalance (8-shape in Figure  
 427 4). As a result, the global mean surface temperature in the Cycle 3 simulations is in close agreement with the ERA5 reanalysis  
 428 (Hersbach et al. 2020), and stays in close agreement over the 5 years of coupled simulations (Figure 5 and Figure C1 in  
 429 Appendix C). Going from Cycle 2 to Cycle 3, the warming over time is not evident anymore in IFS-FESOM and IFS-NEMO  
 430 (Figure 5). Differences in local warming over the Southern Ocean in the two models are further discussed in section 3.2.2.

431  
 432 Locally, some of the persistent TOA radiation biases in Cycle 2 are also still evident in Cycle 3, for example a positive  
 433 shortwave bias along coastlines in stratocumulus regions, while other biases, for example associated with deep convective  
 434 activity over the Maritime Continent, have significantly reduced (not shown).



436

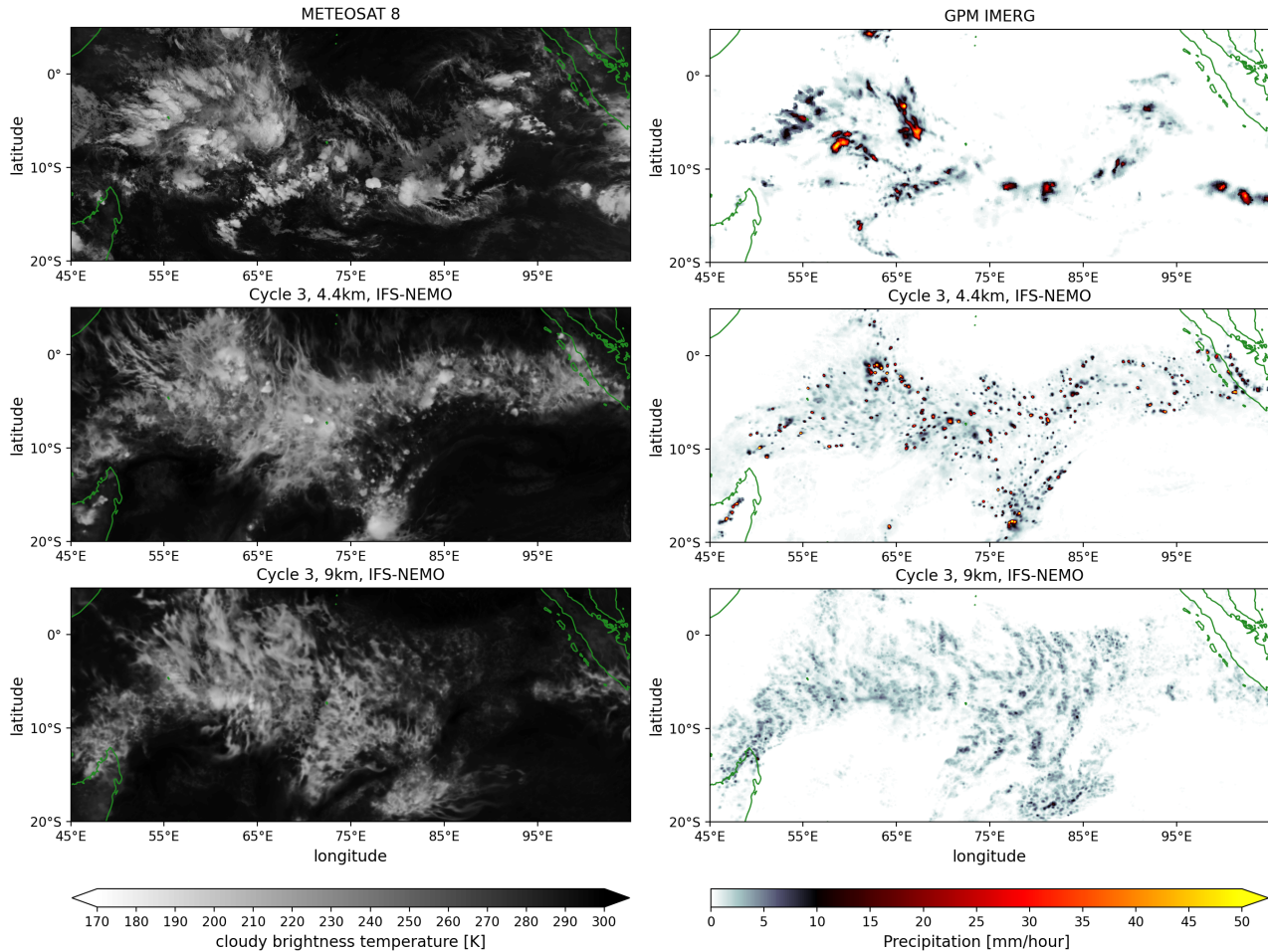
437 **Figure 5: Timeseries of 2-metre temperature global (a), only over land (b) and only over ocean (c) with respect to ERA5,**  
 438 **for the years 2020-2021.** The shaded area shows the ERA5 standard deviation between 2012-2021. The evolution of the 2-  
 439 metre temperature over 5 years is shown in Figure C1 in Appendix C.

440

#### 441 **3.1.4 Improved precipitation characteristics in Cycle 3 vs Cycle 2 and larger-scale impacts**

442 Snapshots of cloudy brightness temperature and precipitation over the Indian Ocean (Fig. 6) illustrate that after 12 days of  
 443 simulation in Cycle 3, there are biases in the characteristics of precipitating deep convection compared to satellite observations,  
 444 even after the developments for Cycle 3 (see Section 3.1.1) were introduced. The observations show multiple mesoscale  
 445 convective systems (MCS), which are associated with strong precipitation intensities and large anvil clouds. Neither the  
 446 baseline 9 km Cycle 3 simulation nor the 4.4 km simulation manage to represent the MCS as observed. At 9 km, the convective  
 447 cells are not well defined with wide-spread areas of weak precipitation. Indeed, precipitation intensity is underestimated in this  
 448 setup, with precipitation intensity rarely exceeding 10 mm/hour (Fig. 7a). Instead of organising into MCS, hints of spurious

449 gravity waves initiated from parametrized convective cells can be seen in the precipitation snapshot, emanating in different  
 450 directions.



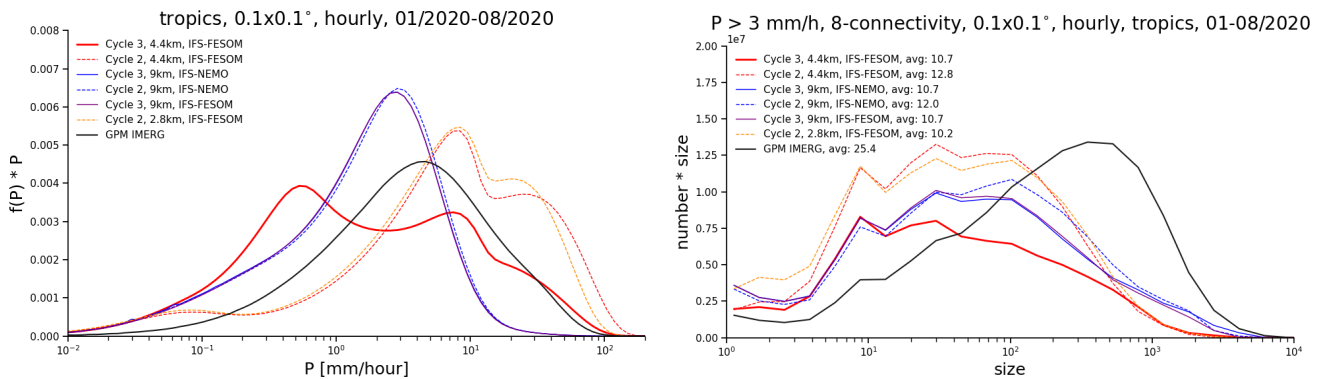
451  
 452 **Figure 6: Snapshot for 31/01/2020 at 21:00 UTC of infra-red brightness temperature (left) and hourly precipitation rate**  
 453 **(right) over the Indian Ocean**, from observations (Meteosat 8 SEVIRI channel 9 and GPM IMERG, 1st row), and at forecast  
 454 day 12 of IFS-NEMO 4.4 km (2nd row) and 9 km (3rd row) simulations. The simulations use the nextGEMS Cycle 3 setup  
 455 except that they are run with a satellite image simulator and, for technical reasons, are coupled to NEMO V3.4 (ORCA025)  
 456 here.

457  
 458 However, at 4.4 km resolution, the deep convection scheme is much less active, as the cloud base mass flux has been reduced  
 459 by a factor of 6 compared to its value at 9 km (see Section 3.1.1). Compared to the Cycle 2 simulations with Deep Off, the  
 460 tropical troposphere is colder and more humid. This setup also features more realistic precipitation intensities, and particularly  
 461 the strong precipitation of more than 10 mm/hour is close to the satellite retrieval GPM IMERG (Figure 7a), while the Cycle  
 462 2 simulations with Deep Off overestimate and with Deep On underestimate intense precipitation. In contrast, weak



463 precipitation of 0.1 to 1 mm/hour is most strongly overestimated at 4.4 km resolution in Cycle 3. This is mostly precipitation  
 464 that stems from the weakly active deep convection scheme. Solutions of how to reduce this drizzle bias are being worked on,  
 465 e.g., through an increase of the rain evaporation rate.

466 A related issue is that the size of convective cells is too small, as illustrated by the size distribution of connected grid cells with  
 467 precipitation exceeding 3 mm/hour (Fig. 7b). The average size of a precipitation cell is rather similar in all simulations, and  
 468 only about half the value as in GPM IMERG. While GPM IMERG has a substantial number of precipitation cells that exceed  
 469 a size of  $10^3$  grid points, which for example would correspond to a precipitation object of  $5^\circ \times 2^\circ$ , this size is almost never  
 470 reached in the IFS simulations. The baseline simulations reach this size more often than the higher-resolution simulations, but  
 471 mainly in association with the spurious gravity waves, not because an MCS would be correctly represented. In summary, the  
 472 representation of intense precipitation has been improved from Cycle 2 to Cycle 3, but that has not led to more realistic  
 473 precipitation cell sizes. Even though it is possible that GPM IMERG overestimates precipitation cell size, cloudy brightness  
 474 temperature shows the same issue (Fig. 6). Work with other models (e.g., ICON, NICAM, SCREAM) has also shown that an  
 475 underestimation of precipitation cell size is a common issue in global km-scale resolution simulations, in some models even  
 476 leading to “popcorn” convection, and will require more attention in the future.  
 477

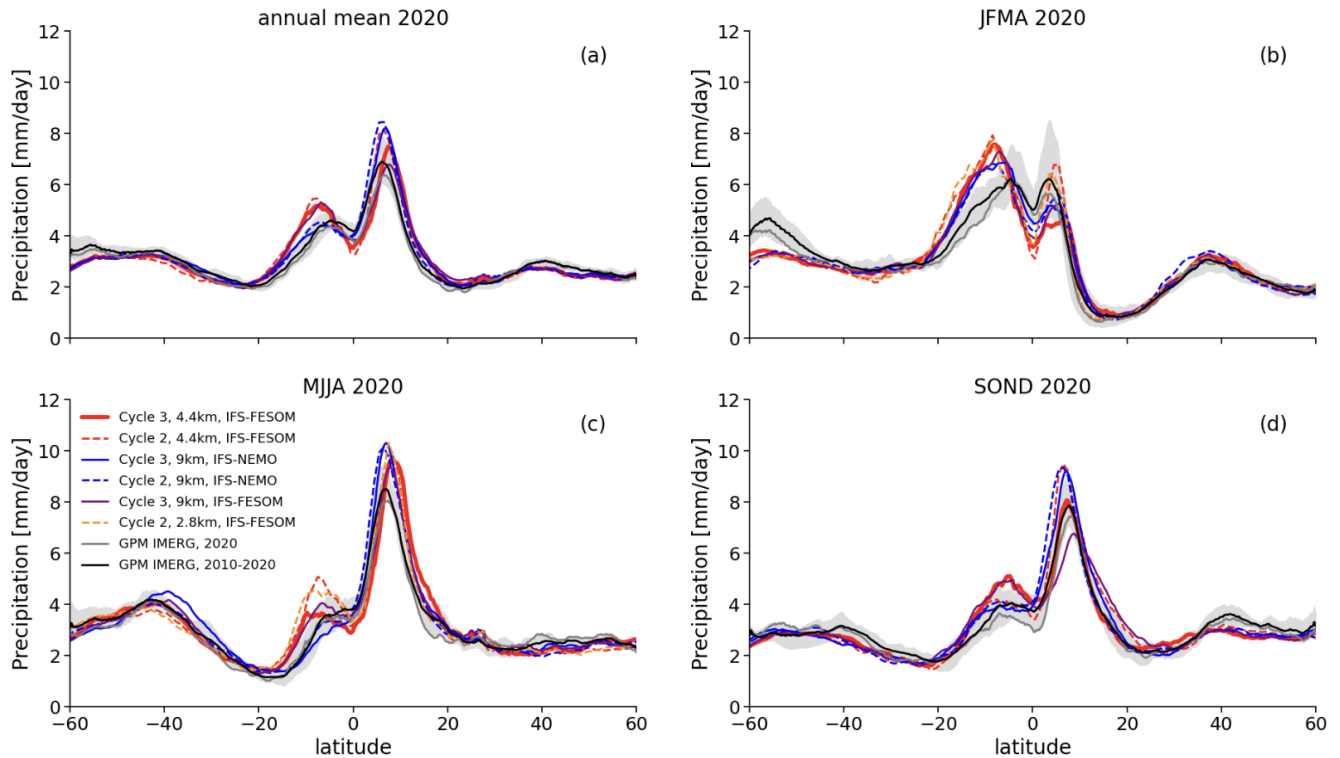


478  
 479 **Figure 7: (a) Frequency times bin intensity of hourly precipitation intensity in the tropics (30S-30N), conservatively**  
 480 **interpolated to a 0.1° grid from January to August 2020.** Following Berthou et al. (2019), the bins are exponential, meaning  
 481 that the area under the curve represents the contribution of that intensity range to the mean. (b) Histogram of precipitation cell  
 482 size times bin size, using a similar approach as in (a). The precipitation cell size is defined as the number of connected grid  
 483 cells on a 0.1° grid (also considering diagonal neighbours) where precipitation exceeds 3 mm/hour, counting cells in the whole  
 484 tropics (30°S-30°N), again from January to August 2020. The average precipitation cell size is given in the legend. The  
 485 observational estimate is from GPM IMERG.

486  
 487 As already mentioned in Section 3.1.1, the characteristics of meso-scale organisation of convection also affect the larger scales.  
 488 For example, in Cycle 2 simulations with Deep Off, the ITCZ often organises into a continuous and persistent line of deep

489 convection over the Pacific at 5°N (see Figure D1 in Appendix D) and as a consequence, the zonal mean precipitation is  
 490 strongly overestimated. This bias improved significantly from Cycle 2 to Cycle 3, when switching from a setup with no deep  
 491 convection scheme in Cycle 2 (at 2.8 and 4.4km resolution) to a setup with reduced cloud base mass flux in Cycle 3 (at 4.4km).  
 492 While the peak of precipitation around 5°N was overestimated by a factor of 2 during individual winter months in the 2.8 and  
 493 4.4km Cycle 2 run (see Figure D2 in Appendix D), the 4.4km Cycle 3 run shows a much reduced bias, and the peak at 5°N is  
 494 thus perfectly aligned with the GPM IMERG observations during September-December (Figure 8d). The 9 km baseline run  
 495 did not change significantly from Cycle 2 to Cycle 3 but it also shows some small improvements with regards to the  
 496 overestimation of the precipitation peak at 5°N.

497 Comparing the FESOM and NEMO runs, it is striking that all FESOM runs overestimate precipitation in the Southern  
 498 Hemisphere tropics around 10°S, hinting at a biased large-scale circulation, while NEMO runs show some good agreement  
 499 with observations. The different seasons (Figure 8b-d) show an overestimation of precipitation at 10°S only during January-  
 500 April in the NEMO runs, while FESOM runs overestimate precipitation at 10°S during most of the year. Additionally, the  
 501 FESOM runs also slightly underestimate precipitation at the equator (particularly during January-April), hinting at a double  
 502 ITCZ bias, which is a common issue in coupled simulations at km-scale resolutions during boreal winter, e.g. in ICON  
 503 (Hohenegger et al., 2023). Compared to ICON and other global coupled km-scale models that contributed to the DYAMOND  
 504 model intercomparison project (Stevens et al., 2019), the zonal mean precipitation biases in IFS nextGEMS Cycle 3 are of  
 505 similar nature and in part smaller than in the other models.



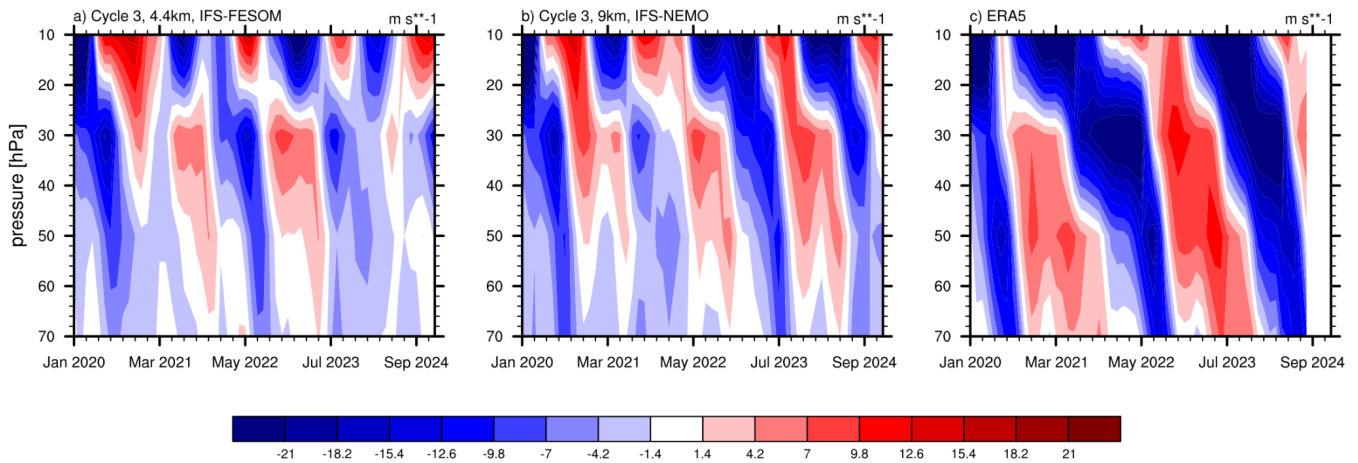
506



507 **Figure 8: Zonal-mean precipitation in nextGEMS Cycle 2 and 3, averaged over the year 2020 (a) and for different 4-**  
 508 **months periods in 2020, January-April (b), May-August (c) and September-December (d).** Observations are from GPM  
 509 IMERG for the year 2020 and for the 2010-2020 climatological period, indicating the climatological range of individual years  
 510 via the grey shading.

511

### 512 3.1.5 Stratospheric Quasi-Biennial Oscillation



513

514 **Figure 9: Time evolution of monthly-mean zonal winds, averaged over the equatorial band 10S-10N, for a) the 9 km**  
 515 **Cycle 3 simulation with IFS-NEMO, b) the 4.4 km Cycle 3 simulation with IFS-FESOM, and c) the ERA5 reanalysis for**  
 516 **reference.**

517 The Quasi-Biennial Oscillation (QBO) in the equatorial stratospheric winds is driven by momentum deposited by breaking  
 518 small-scale convectively generated gravity waves (GWs) and large-scale Kelvin and Rossby-gravity waves (e.g., Baldwin et  
 519 al., 2001). The QBO can have a downward influence on the troposphere (e.g., Scaife et al., 2022) and it is thus important to  
 520 simulate it well in seasonal and decadal prediction models. As km-scale models explicitly resolve GWs to a large extent, they  
 521 have a potential to better simulate the QBO than lower resolution models (e.g., CMIP), which fully rely on GW  
 522 parametrizations. However, GW parametrizations are often tuned to get a good QBO in lower resolution models (Garfinkel et  
 523 al., 2022; Stockdale et al., 2022) and at higher resolution the resolved GW forcing can be overestimated with less freedom for  
 524 tuning. For example, whether parametrized deep convection is switched on or off has a large impact on resolved GWs, with  
 525 fully resolved convection generating more than two times stronger GW forcing (Stephan et al., 2019; Polichtchouk et al., 2021)  
 526 and a QBO period that is – as a result – too fast.

527 We find that the QBO is reasonably well simulated in the nextGEMS Cycle 3 simulations at 9 km and even at km-scale (4.4  
 528 km) resolution (Fig. 9). The periodicity is reasonable, peaking at around 20 months at 30hPa for both simulations (calculated

529 by performing FFT on the monthly timeseries). This can be probably further improved by tuning the strength of parametrized  
530 non-orographic GW drag, which is still on with reduced magnitude in both 9km and 4.4km simulations, reduced to 70% and  
531 35%, respectively, compared to that at 28 km resolution.

532 In the lower stratosphere below 40hPa, the amplitude of the QBO, however, is underestimated (compare panels a-b) to panel  
533 c) in Fig. 9), especially for the eastward phase. This deficiency is also observed in many lower-resolution models (Bushell et  
534 al., 2022). We hypothesise that the overall reasonable QBO simulation at km-scale resolution might partly be due to the  
535 parametrization for deep convection being still “slightly on” in the Cycle 3 simulations with IFS, as detailed in the previous  
536 section.

## 537 **3.2 Ocean, Sea ice, and Waves**

### 538 **3.2.1 Key issues and model developments**

539 From a model development point of view, one of the main purposes of the nextGEMS Cycle 3 simulations was to set up and  
540 test a fully-coupled global model that runs over multiple years and still does not show drift in global mean surface temperature  
541 and other main climate characteristics, prior to performing the final multi-decadal integrations foreseen in nextGEMS. To  
542 improve the general ocean state, an eddy-resolving ocean grid had been introduced already from Cycle 2 onwards. To reduce  
543 the drift further (Figure 5), in particular over the Southern Ocean where the model in Cycle 2 had still shown a strong warming  
544 over the ocean with time compared to the ERA5 range for 2020-2021, the FESOM ocean component has been updated to the  
545 latest release version 2.5 and coupling between the ocean and atmosphere has been improved.

#### 546 **Warm biases over the ocean**

547 The warming ocean in Cycle 2 leads to an overall warming of the atmosphere as well. The 4.4km IFS-FESOM simulations in  
548 Cycle 2 with 5km resolution in the ocean had shown a warming over the Southern Ocean in winter and year-round in the  
549 tropics. For Cycle 3, the latter has been significantly improved by tuning the TOA balance and by using partially active  
550 parametrized convection, while the former has been solved by a combination of different factors, namely (i) improvements in  
551 the consistency of the heat flux treatment between the atmosphere and ocean/sea ice component, (ii) heat is taken from the  
552 ocean in order to melt snow falling into the ocean, which had been overlooked before, (iii) the activation of a climatological  
553 runoff/meltwater flux around Antarctica (COREv2, Large and Yeager 2009), and (iv) a general update from FESOM2.1 to  
554 FESOM2.5 (Rackow et al. 2023c, <https://github.com/FESOM/fesom2/releases/tag/2.5/>). The resulting more realistic  
555 temperature evolution in Cycle 3 is discussed in Section 3.2.2.

#### 556 **Ocean currents, eddy variability, and mixed-layer**

557 The eddy-permitting ocean grid in Cycle 1 simulations with IFS-FESOM can impact not just the temperature evolution but  
558 also the simulated eddy variability, mean currents, and details of the simulated mixed layer, which all evolve on sub-5-year

559 timescales and are thus relevant to the longer-term performance of a coupled model. An analysis of the resulting simulated  
560 ocean state, including mesoscale eddy statistics and mixed layer, with the final ocean eddy-resolving IFS-FESOM simulations  
561 in Cycle 3 is presented in Section 3.2.3.

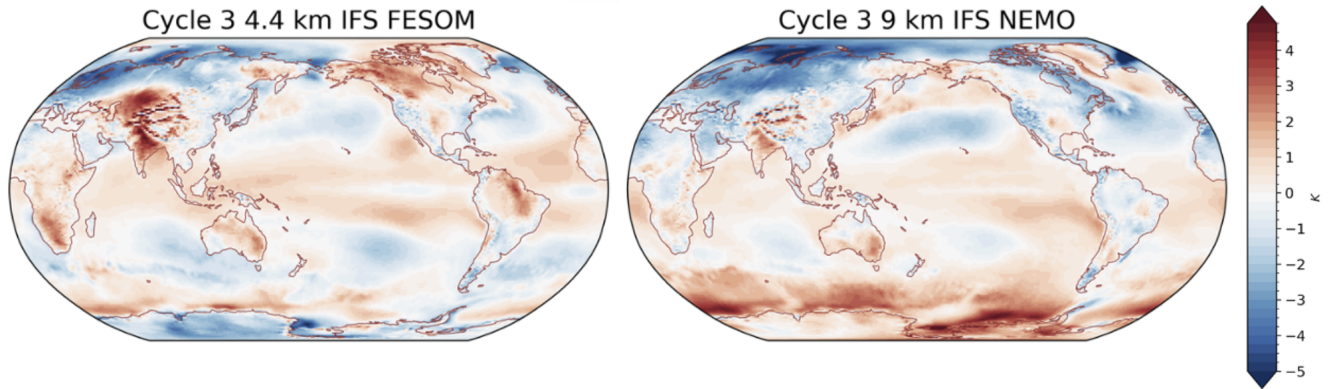
## 562 **Sea ice performance**

563 In Cycle 1 and 2, the sea ice representation in IFS-FESOM showed prominent deviations from the observed seasonal cycle in  
564 the Ocean and Sea Ice Satellite Application Facility (OSI-SAF) dataset. This could be addressed mainly by correcting the  
565 shortwave flux over ice with the release of FESOM version 2.5. The resulting sea ice performance in Cycle 3 is discussed in  
566 Section 3.2.4.

## 567 **3.2.2 Improved Southern Ocean temperature evolution**

568 As already mentioned in section 3.1.3, IFS-FESOM simulations in Cycle 2 (TCo2559 and NG5 grid in the ocean) had shown  
569 a warming over the Southern Ocean in winter and year-round in the tropics. For Cycle 3, the improvement in IFS-FESOM  
570 4.4km is particularly evident when comparing to the operational 9km IFS setup with NEMO V3.4. While the Southern Ocean  
571 shows a similar magnitude of anomalies in IFS-FESOM TCo2559-NG5 in year 5 compared to the first year, there appears to  
572 be an increase of anomalies over time in IFS-NEMO (Figure 10). This has been confirmed in a second set of IFS-FESOM  
573 simulations at TCo399 resolution (28km), and on the tORCA025 ocean grid (not shown).

574

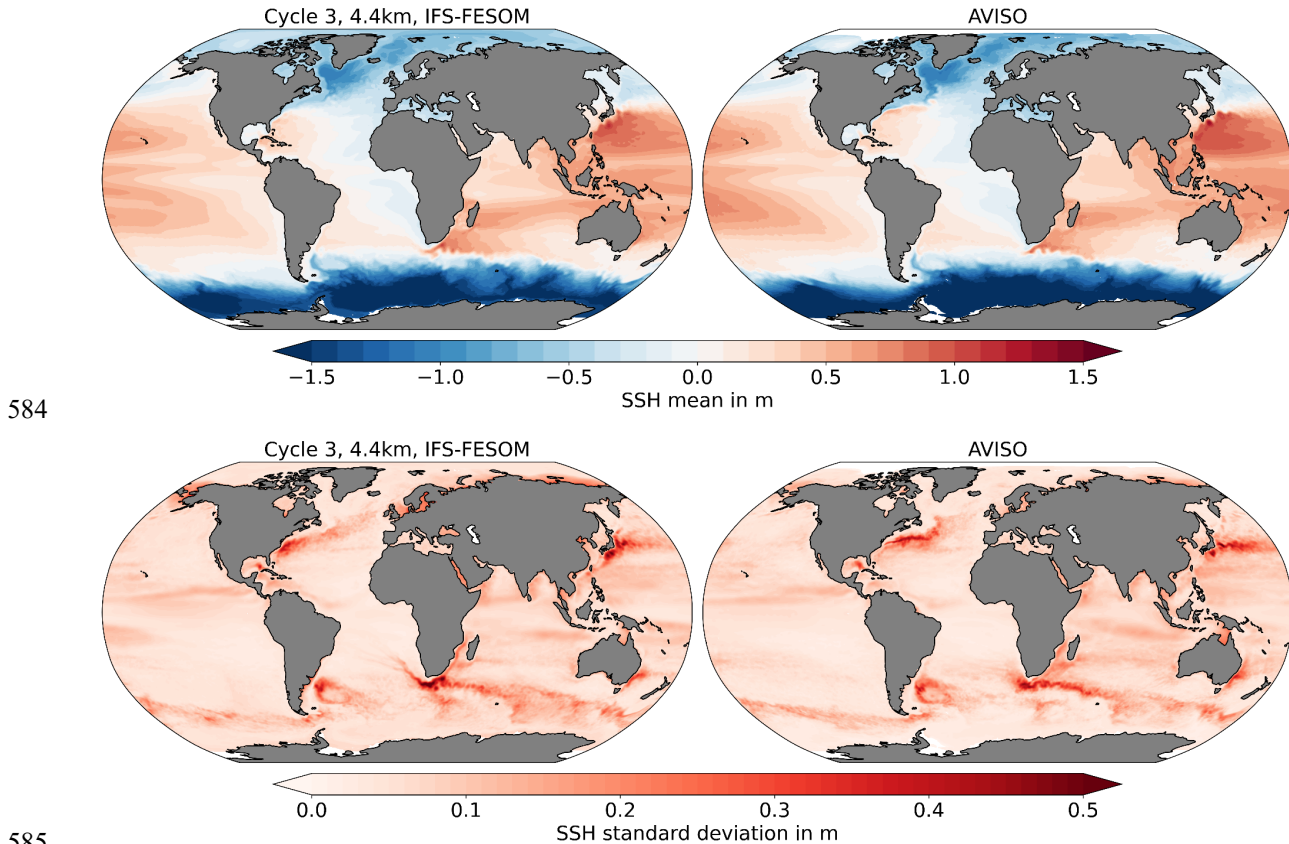


575

576 **Figure 10: Anomaly of annual-mean 2m temperature in year 5 of the nextGEMS Cycle 3 simulations, initialised on 20**  
577 **January 2020, compared to the mean of ERA5 over 2020-2021. (left) IFS-FESOM 4.4km/NG5, and (right) IFS-NEMO**  
578 **9km/ORCA025.**

579 **3.2.3 Simulated ocean state in terms of currents, eddy variability, and mixed layer**

580 Daily sea surface height (SSH) data is taken from the IFS-FESOM outputs and compared with the AVISO multi satellite  
581 altimeter data of daily gridded absolute dynamic topography, representing the observed SSH (Pujol et al. 2016). While ocean  
582 eddy variability in the 4.4km IFS-FESOM Cycle 3 simulation and AVISO can be diagnosed from standard deviation of sea  
583 surface height, the structure of (geostrophic) mean currents is diagnosed here from the time-mean SSH.



586 **Figure 11: Mean Ocean currents and eddy variability expressed as the time-mean of the daily sea surface height (SSH)**  
587 **and as the standard deviation of daily SSH data.** (left column) Data from the Cycle 3 simulation of IFS-FESOM model and  
588 from (right column) AVISO multi-satellite altimeter data. In AVISO, the global mean SSH is removed from each grid-point.  
589 AVISO data consists of the time period 2017-2021 while 2020-2024 is used for IFS-FESOM.

590

591 Both the time-mean and variability of SSH show an excellent agreement between the simulation and observations from AVISO  
592 (Fig. 11). The position of the main gyres and the gradient of SSH is well-reproduced, indicating a good performance in terms  
593 of position and strength of the main ocean currents. Ocean eddy variability is very similar as well with the eddy-resolving NG5  
594 grid that has been introduced for IFS nextGEMS simulations (see Fig. B1 in Appendix B). However, while there are positive  
595 indications, the North Atlantic Current as northward extension of the Gulf Stream still underestimates SSH variability over the

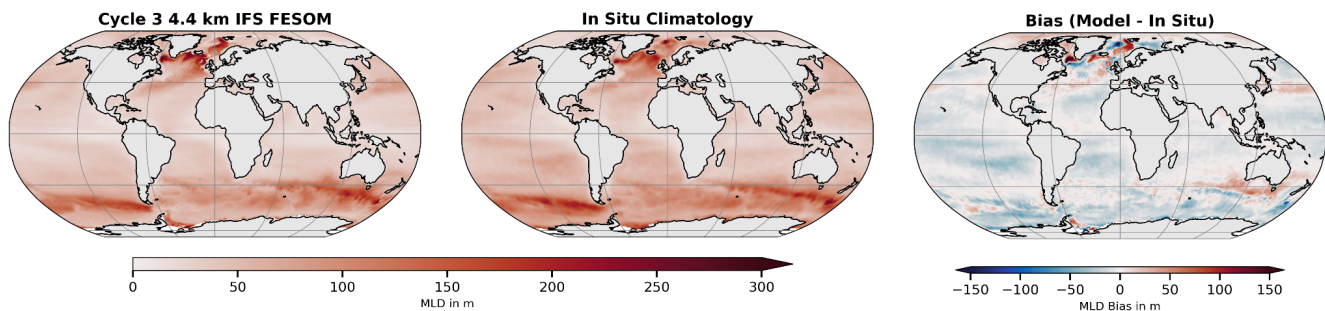
596 North-West corner. Moreover, Agulhas rings forming at the tip of South Africa seem to follow a too narrow, static path  
597 compared to observations.

598

599 Mixed-layer depth (MLD) is calculated using a density threshold criterion of  $0.03 \text{ kg/m}^3$  from the 10 m depth value. The in-  
600 situ MLD climatology dataset produced by de Boyer Montégut (2023) is based on about 7.3 million casts/profiles of  
601 temperature and salinity measurements made at sea between January 1970 and December 2021. While the qualitative  
602 agreement between the 4.4km IFS-FESOM Cycle 3 simulation and observations is excellent (Fig. 12), IFS-FESOM  
603 underestimates MLD across most of the ocean areas, with values not exceeding 0-50 meters. Largest biases are in the North  
604 Atlantic sector, which aligns with MLD bias results from stand-alone FESOM simulations (Treguier et al. 2023) for a 10-50  
605 km ocean grid. Specifically, FESOM overestimates (deepens) MLD in the Labrador Sea, over the Reykjanes Ridge, and in the  
606 Norwegian Sea, while underestimating MLD in the Irminger Sea and the Greenland Sea.

607 Overall, the distribution of MLD in IFS-FESOM is comparable to the stand-alone lower-resolution FESOM ocean simulations.  
608 In coupled models, we could typically expect larger biases than presented here, although the relatively short 5-year period of  
609 the Cycle 3 simulation may not be sufficient to fully develop the MLD biases. In particular, IFS-FESOM does not show open-  
610 ocean convection in the Southern Ocean's Weddell Sea, which is a common bias in CMIP models.

611



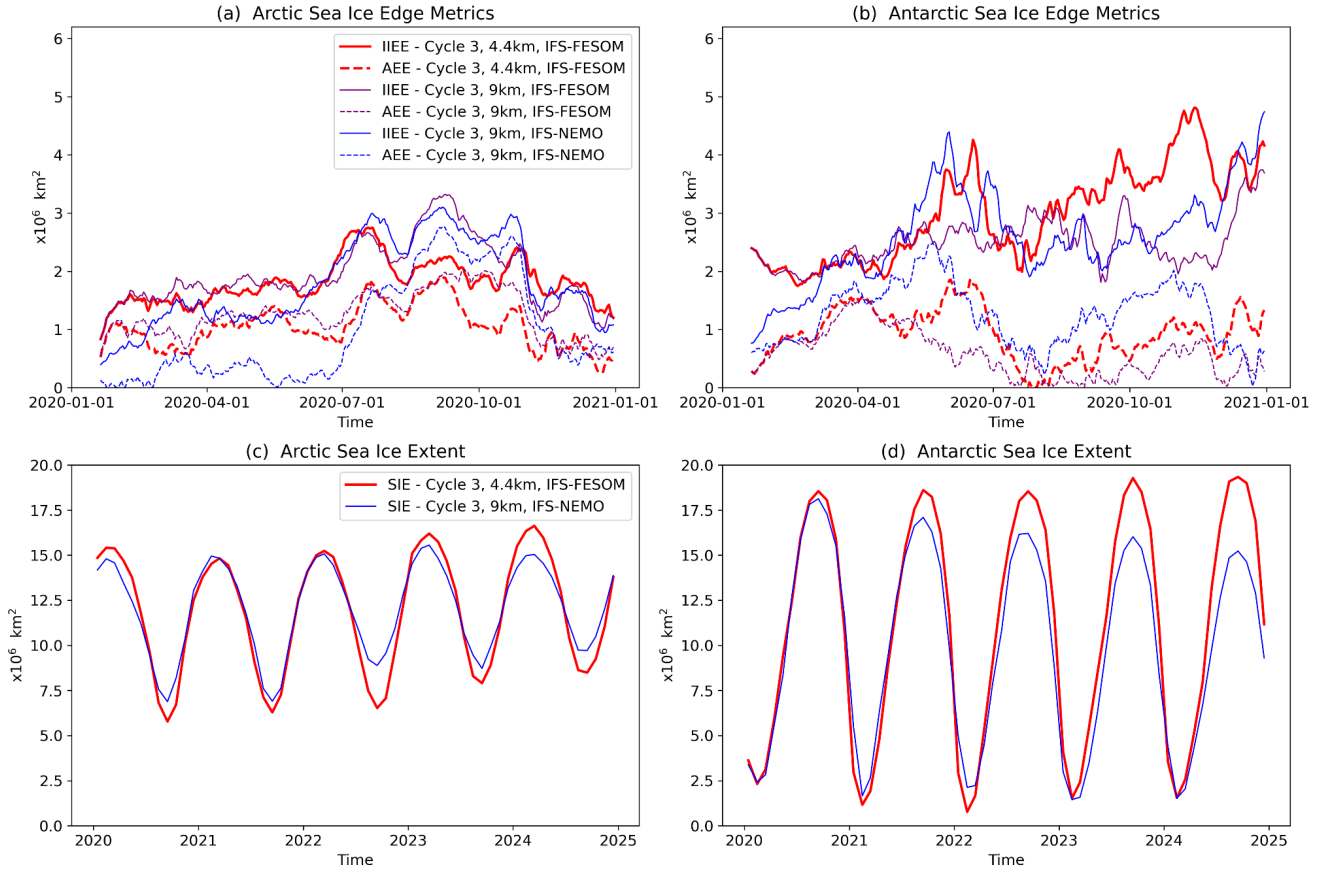
612

613 **Figure 12: Mixed-layer depth (MLD) in simulations and observations.** MLD was averaged over the entire time period in  
614 (left) the 4.4km IFS-FESOM Cycle 3 simulation. (centre) MLD in-situ climatology from de Boyer Montégut (2023), and  
615 (right) difference plot (model - climatology).

### 616 3.2.4 Integrated sea ice performance metrics

617 The performance of the nextGEMS Cycle 3 simulations is analysed in terms of the sea ice extent and sea ice edge position  
618 (Fig. 13). The Integrated Ice Edge Error (IIEE), the Absolute Extent Error (AEE), and the Sea Ice Extent (SIE) metrics are  
619 used for comparing the model simulations and daily 2020 remote-sensing sea ice concentration observations from the Ocean  
620 and Sea Ice Satellite Application Facility (OSI SAF). Specifically, the recently released Global Sea Ice Concentration climate  
621 data record (SMMR/SSMI/SSMIS), release 3 (OSI-450-a; OSI SAF 2022) is considered in our analysis. The IIEE is a  
622 positively defined metric introduced by Goessling et al. (2016), and it is commonly used for evaluating the correctness of the

623 sea ice edge position in Arctic and Antarctic sea ice predictions (Zampieri et al. 2018, Zampieri et al. 2019). We compute the  
 624 IIEE by summing the areas where the model overestimates and underestimates the observed sea ice edge, here defined by the  
 625 15% sea ice concentration contour. The SIE is the hemispherically integrated area where the sea ice concentration is larger  
 626 than 15%. Finally, the AEE represents the absolute difference in the hemispheric SIE of models and observations, therefore  
 627 not accounting for errors arising from a different distribution of the ice edge in the two sets.  
 628



629  
 630 **Figure 13: (a) Arctic daily Integrated Ice Edge Error (IIEE; solid lines) and Absolute Extent Error (AEE; dashed lines)**  
 631 **for three different Cycle 3 simulations. (b) is the same as (a), but for Antarctic sea ice.** The IIEE and AEE metrics are  
 632 computed by comparing the three model runs against remote-sensing sea ice concentration observations from OSI-SAF. (c)  
 633 and (d) show the Arctic and Antarctic sea ice extent for two different Cycle 3 simulations from 2020 until the end of 2024.  
 634

635 All model configurations show substantial errors in representing the initial state. In the Arctic, the error grows in the first  
 636 simulation days in response to the active coupling between the sea ice components and the IFS atmospheric model (Fig. 13a).  
 637 In the Antarctic, an initial error growth takes place for the IFS-NEMO model configuration, while modest error mitigation is



638 seen for the two IFS-FESOM configurations (Fig. 13b). The latter feature suggests that a coupled setup could be better suited  
639 to represent the Antarctic sea ice processes in the FESOM models, at least for this specific instance. Both in the Arctic and  
640 Antarctic, the initial error of the IFS-NEMO configuration is substantially lower than that of the IFS-FESOM configurations.  
641 This behaviour is expected since NEMO performs active data assimilation, while the sea ice in FESOM is only constrained by  
642 the ERA5 atmospheric forcing (Hersbach et al. 2020) imposed during the ocean-sea ice model spinup. In the Antarctic, the  
643 initial error differences diminish quickly and, after a couple of months, the errors of IFS-NEMO and IFS-FESOM are similar.  
644 In the Arctic, IFS-NEMO exhibits residual prediction skill over IFS-FESOM in late spring, four to six months after the  
645 initialization, possibly due to a more accurate description of the Arctic Ocean heat content influenced by the use of proper  
646 ocean data assimilation techniques. After the initialization, the pan-hemispheric sea ice model performance is similar for the  
647 three configurations, and attributing the error differences to the use of different model resolution or complexity is not obvious,  
648 confirming previous findings (e.g., Streffing et al. 2022; Selivanova et al., 2023). Overall, the model errors for the first year of  
649 simulations are in line with state-of-the-art seasonal prediction systems (Johnson et al. 2019; Mu et al. 2020; Mu et al. 2022),  
650 showing similar features in terms of seasonal error growth.

651  
652 When considering longer timescales (5-year simulations), model drifts are visible for the IFS-NEMO configuration and, to a  
653 lesser extent, for the IFS-FESOM setup. In particular, the NEMO setup appears to progressively lose the winter sea ice cover  
654 in the Southern Ocean (Fig. 13d). This behaviour is not compatible with the observed interannual variability of the Antarctic  
655 sea ice and it is likely due to the near-surface temperature warming, which is not affecting the IFS-FESOM setup. Our  
656 hypothesis is that the initialisation strategy for FESOM and NEMO accounts for part of the discrepancies in the multi-year  
657 drift between IFS-NEMO and IFS-FESOM. We found that active data assimilation improved the model performance for the  
658 initial months, while an uncoupled ocean spinup might be preferable for minimizing the drift towards the ocean model's  
659 equilibrium state during the 5-year coupled simulation. In the Arctic, the sea ice extent tends to increase progressively in both  
660 the FESOM and NEMO setups, with an additional dampening of the seasonal cycle observed for NEMO (Fig. 13c). Different  
661 multi-year drift regimes between NEMO and FESOM could be also attributed to diverse complexity of the underlying sea ice  
662 models. The more sophisticated physical parametrizations of the NEMO V3.4 configuration could respond more to the active  
663 coupling with IFS compared to the FESOM setups.

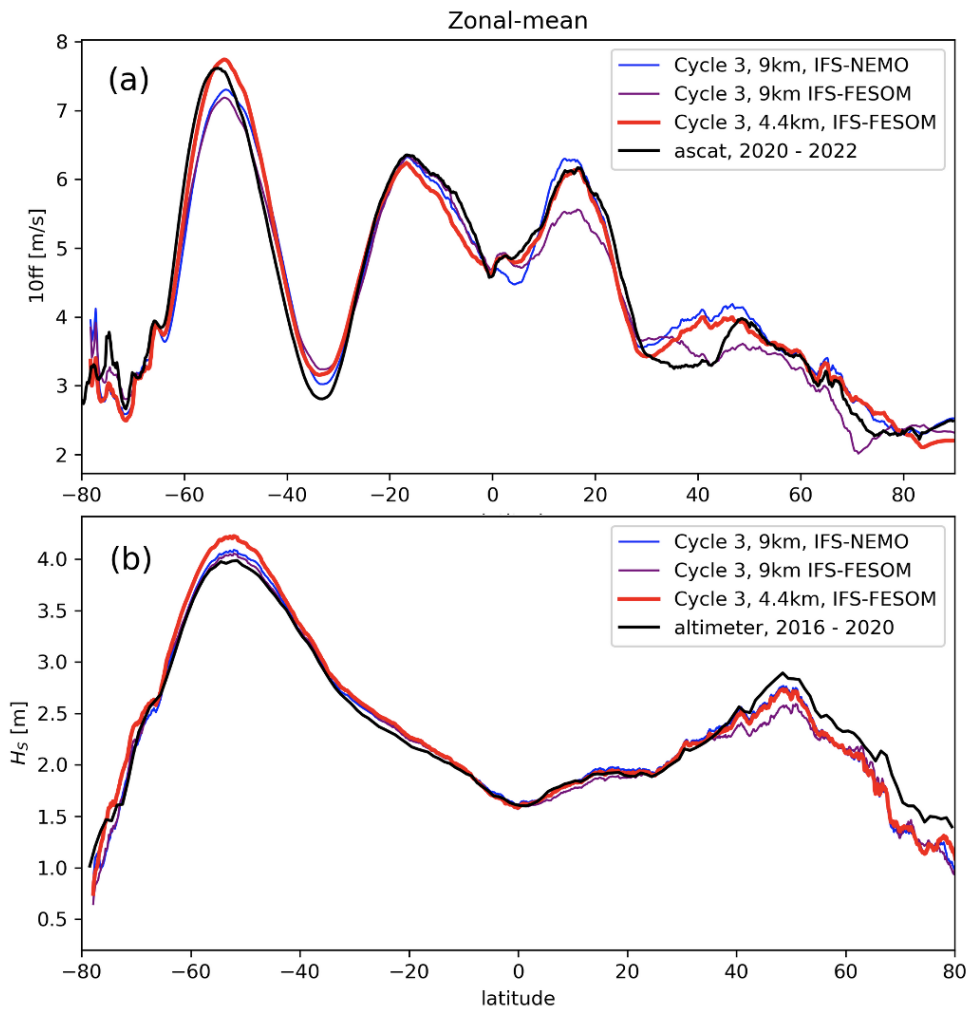
664

### 665 **3.2.5 Wind and waves**

666 As written above in Section 2, in the IFS there is an active two-way coupling between the atmosphere and ocean waves. Surface  
667 wind stress generates ocean surface waves and in turn those waves modulate the wind stress. The increase in resolution from  
668 4.4km relative to the 9km for the IFS-FESOM simulations results in significant increases in wind speed in the storm tracks  
669 (~50S and ~45N; Fig. 14a), most likely due to the increased ability to resolve the intense winds in the extratropical cyclones.  
670 This increased resolution looks to be particularly important for the Southern Ocean, as the 4.4km simulation is the only one of

671 the three simulations that can achieve winds of realistic intensity in this area. We also note a significant improvement in the  
672 trade winds ( $\sim 15^{\circ}\text{N}$ ) for the 4.4km IFS-FESOM simulation.

673



674

675 **Figure 14: Zonal-means of 10-metre wind speed ‘10ff’ over ocean (a) and significant wave height (b) in nextGEMS**  
676 **Cycle 3.** Observations in black are from Copernicus Marine Service for wind speed (‘ascat’; scatterometer combined with  
677 ERA5), and the ESA-CCI (v3) cross-calibrated altimeter record for wave height (‘altimeter’).

678

679 The waves in the storm tracks are also significantly larger (Fig. 14b). The increased wind is likely partly responsible for this  
680 increase. The second factor likely playing a role here is the change in fetch, i.e. the area of ocean over which the wind is  
681 contributing to wave growth. A notable decrease in mean sea ice concentration (more than ten percent) takes place in the 4.4km  
682 simulation (Fig. E1a), thereby freeing up the ocean surface here for wave growth. These changes can be directly seen in the



683 wave field in the according areas (Fig. E1b). These waves then continue to grow with the wind as they propagate into the  
684 Southern Ocean, thereby contributing to the larger waves seen in this region. For the NH storm track, this points to an  
685 improvement with respect to altimeter observations, but for the Southern Ocean the 4.4km simulation is now somewhat  
686 overestimating the waves.

### 687 **3.3 Land**

688 Performing simulations at the km-scale inherently brings a richer picture in the atmosphere and ocean in terms of small-scale  
689 features, as more scales become explicitly resolved. To gain the full benefit of the resolution over land, it is important that the  
690 surface information is also at an equivalent or finer resolution. Therefore, work at ECMWF in recent years has been directed  
691 to provide the IFS surface model ECLand (Bousetta et al., 2021) with surface global ancillary information of a resolution down  
692 to 1 km or finer, and to include additional processes that become relevant at those scales. These developments had always the  
693 improvement of the operational IFS as a goal and focused, therefore, on timescales from days to a few months. nextGEMS  
694 simulations present a timely opportunity to test these changes in parallel before they become operational, and to assess their  
695 impact when fully coupled on multi-annual timescales. Most of the developments in this section are described in more detail  
696 by Bousetta et al. (2021). Here in this section, nextGEMS Cycle 2 and Cycle 3 will refer to IFS CY48r1 (ECMWF, 2023b)  
697 and CY49r1 (scheduled for 2024), respectively.

#### 698 **3.3.1 Km-scale surface information**

699 An improved land-water mask was included for nextGEMS Cycle 2. The original source belonging to the Joint Research  
700 Centre (JRC) had a nominal resolution of 30m. The mask was further improved by including glacier data and new land-water  
701 and lake fraction masks. In parallel, lake depth data was improved (Bousetta et al., 2021).  
702 Further changes to the land-water mask were tested in nextGEMS Cycle 3. The Land Use/Land Cover maps (LU/LC) used  
703 before nextGEMS Cycle 3 were based on those from GLCCv1.2 data (Loveland et al., 2000), which is based on observations  
704 from the Advanced Very High Resolution Radiometer (AVHRR) covering the period 1992–1993. They had a nominal  
705 resolution of about 1km. In nextGEMS Cycle 3, we used new maps, based on ESA-CCI, which exploit the high resolution of  
706 recent remote sensing products down to 300m and will pave the way to enable observation-based time-varying LU/LC maps  
707 in the future. These maps lead to a more realistic overall increase of low vegetation cover compared to the GLCCv1.2-based  
708 maps, at the expense of the high vegetation cover. The new conversion from ESA-CCI to the Biosphere-Atmosphere Transfer  
709 Scheme (BATS) vegetation types used by ECLand also reduces the presence of ambiguous vegetation types like ‘interrupted  
710 forest’ or ‘mixed forest’. In addition, work has been done on upgrading the Leaf Area Index (LAI) seasonality and its  
711 disaggregation into low and high-vegetation LAI. This improves, among others, the previously found overestimation of total  
712 LAI during March-April-May (MAM) and September-October-November (SON). This revised description of the vegetation

713 will also be used in the next operational IFS cycle (49R1), and an initial implementation and evaluation is presented in Nogueira  
714 et al (2021).

715 The thermodynamic effects of urban environments emerge at the surface as models refine resolution down to the km-scale and  
716 the rural-urban contrast sharpens. To determine where to activate the urban processes at the surface, a global map of urban  
717 land cover is used in our nextGEMS Cycle 3 simulations. This map, based on information provided by ECOCLIMAP-SG at  
718 an initial 300m horizontal resolution (McNorton et al., 2023; Faroux et al., 2013), will also be used in the next operational IFS  
719 cycle 49R1.

### 720 **3.3.2 Km-scale surface processes**

721 The presence of the fine spatial information described above opens the path to simulate relevant km-scale processes and  
722 interactions. In particular, the representation of snow, 2-metre temperature, and urban areas was improved as explained in the  
723 following.

724 A newly developed multi-layer snow scheme was implemented in IFS CY48r1 and was already used in the nextGEMS Cycle  
725 2 (Arduini et al. 2019), substituting the existing snow bulk-layer scheme. The new scheme dynamically varies the number of  
726 snow model layers depending on the snow depth and provides snow temperature, density, liquid water content and albedo as  
727 prognostic variables. In addition, snow and frozen soil parameters were modified for improved river discharge (Zsoter et al.,  
728 2022) and permafrost extent (Cao et al. 2022). An additional upgrade in nextGEMS Cycle 3 was a package of changes to  
729 ECLand which will be included in the next operational IFS cycle (49R1). This contains an improved postprocessing of 2-metre  
730 temperature reducing the warm bias present occasionally under very stable conditions. It also contains a significant upgrade  
731 to the representation of the near-surface impact of urban areas. For this purpose, the urban scheme developed in ECLand was  
732 activated. This scheme considers the urban environment as an interface connecting the sub-surface soil and the atmosphere  
733 above (McNorton 2021, McNorton 2023). The urban tile comprises both a canyon and roof fraction. In terms of energy and  
734 moisture storage, the uppermost soil layer is not specific to the tile but represents a grid-cell average. This results in a weighted  
735 average that accounts for both urban and non-urban environments. The albedo and emissivity values used in radiation exchange  
736 computations (McNorton 2021, McNorton 2023) are determined based on an assumption of an "infinite canyon," taking into  
737 account "shadowing." The roughness length for momentum and heat follows the model proposed by Macdonald et al. (1998)  
738 and varies according to urban morphology. Simplified assumptions regarding snow clearing and run-off are incorporated based  
739 on literature estimates (e.g., Paul & Meyer, 2001). Illustrative examples of urban cover characteristics and the impact of  
740 accounting for urbanised areas in Cycle 3 vs Cycle 2 simulations are highlighted in Section 4.3.

## 741 **4 Selected examples of significant advances in km-scale nextGEMS simulations**

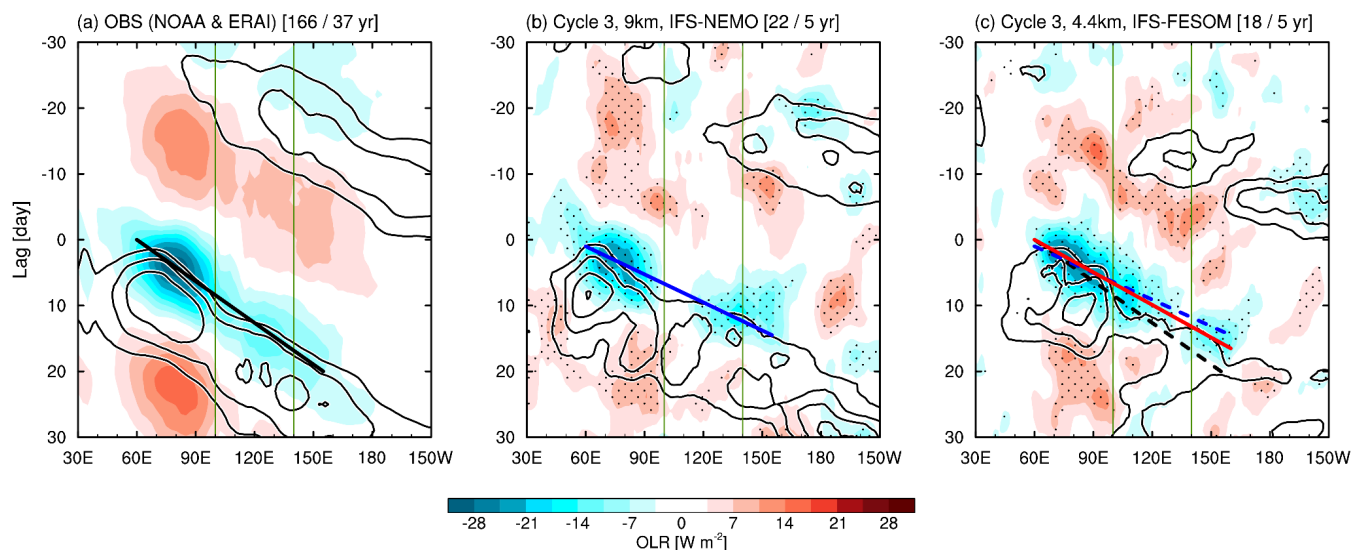
742 In this section, we will highlight three examples of notable advances in the Cycle 3 4.4km nextGEMS simulations that emerge  
743 due to the km-scale character of our simulations. Besides successes in the representation of the Madden-Julian Oscillation

744 (MJO), an important variability pattern that is linked to the monsoons, we also provide examples of small-scale air-sea ice  
745 interactions in the Arctic, and touch on atmospheric impacts due to the new addition of km-scale cities in the IFS. We expect  
746 more in-depth process studies as part of ongoing analyses within the nextGEMS community and as part of dedicated future  
747 work.

#### 748 **4.1 MJO propagation and spectral characteristics of tropical convection**

749 The MJO is a dominant intraseasonal variability mode in the tropics, characterised by slow eastward propagation of large-  
750 scale convective envelopes over the Indo–Pacific warm pool (Madden and Julian, 1972). The MJO convection and circulations  
751 have profound impacts on weather and climate variability globally (Zhang, 2013), so that it is important to reproduce the MJO  
752 in global circulation models (GCMs) targeting seasonal-to-decadal simulations. Having the MJO well represented in models  
753 is indicative of a better tropical or global circulation. Because the reproducibility of the MJO is highly sensitive to the treatment  
754 of cumulus convection (e.g., Hannah and Maloney, 2011), many conventional GCMs that adopt cumulus parametrizations,  
755 which have uncertainties in the estimation of cumulus mass fluxes and moistening and heating rates, still struggle with  
756 simulating important MJO characteristics such as amplitudes, propagation speeds, and occurrence frequencies appropriately  
757 (e.g., Ling et al., 2019; Ahn et al., 2020; Chen et al., 2021). This issue might be improved by km-scale simulations as a result  
758 of more accurate representation of moist processes, as represented by the first success of an MJO hindcast simulation with  
759 NICAM (Miura et al. 2007), but also other physical processes (besides convection) play a role for skilful MJO simulations  
760 (Yano and Wedi, 2021).

761  
762 Figure 15 illustrates the MJO propagation characteristics in the Cycle 3 4.4km IFS-FESOM simulation in comparison with the  
763 observations and the 9km IFS-NEMO simulation, using the MJO event-based detection method (Suematsu and Miura, 2018;  
764 Takasuka and Satoh, 2020). Note that the observational reference is made by the interpolated daily OLR from the NOAA  
765 polar-orbiting satellite (Liebmann and Smith, 1996) and ERA-Interim reanalysis (Dee et al. 2011) during the period of 1982–  
766 2018. While the 9km simulation already does a very good job and both the 9km and 4.4km simulations can reproduce the  
767 overall eastward propagation of MJO convection coupled with zonal winds (Figures 15b and 15c), the 4.4km simulation allows  
768 to improve even further in terms of amplitudes and propagation speeds. Specifically, MJO convective envelopes in the 4.4km  
769 simulation are continuously organised when they propagate into the Maritime Continent (see OLR anomalies in 100°–120°E),  
770 and their propagation speeds become slower than in the 9km simulation and thus closer to those in the observation. We  
771 hypothesize that km-scale resolutions and partially resolved convection can better represent convective systems around  
772 complex land-sea distributions and topography. Nevertheless, the 4.4km simulation still retains several biases compared to the  
773 observed MJOs such as much faster propagation and weaker convection amplitudes to the east of 120°E (i.e., the eastern part  
774 of the Maritime Continent).



775

776

777

778

779

780

781

782

783

784

785

786

787

788

789

790

791

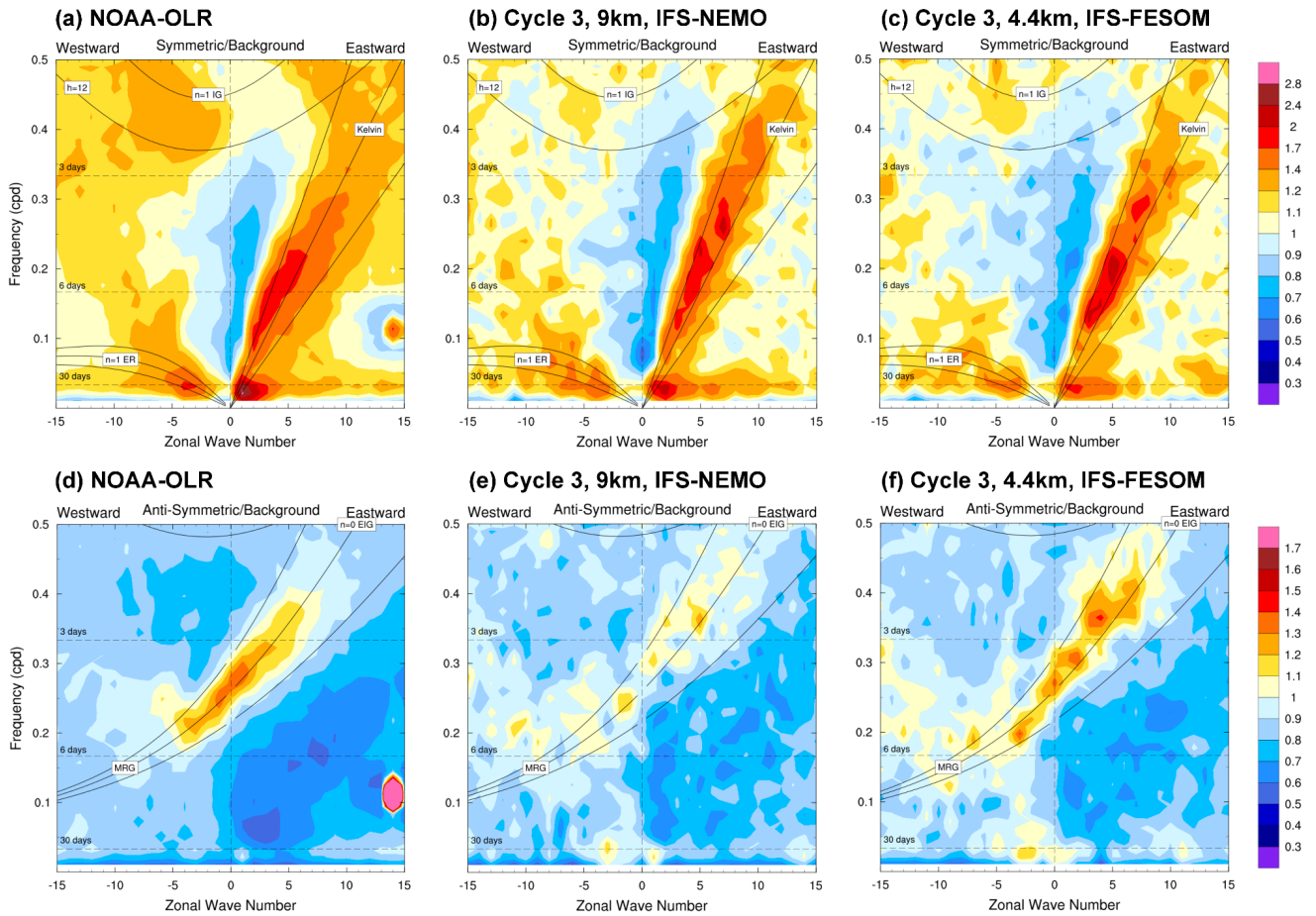
792

793

794

**Figure 15: Propagation characteristics of MJO convection and circulations composited from (a) observations and (b) IFS 9km simulation with NEMO and (c) IFS 4.4km simulation with FESOM.** Time–longitude diagrams of lagged-composite intraseasonal OLR (shading) and 850-hPa westerly wind anomalies (contours) averaged over 10°N–10°S. Contour interval is 0.5 m/s, with zero contours omitted. Stippling in (b) and (c) denotes statistical significance of OLR anomalies at the 90% level (All shading in (a) satisfies this significance). The number of detected MJO cases is denoted at the top of the figures together with analysis periods. Green lines indicate the longitudinal range over the Maritime Continent, and black, blue, and red lines indicate the centre of MJO convective envelopes for the observations, the 9 km simulation, and for the 4.4 km simulation, respectively.

Notwithstanding the intricacies of tropical mesoscale circulations (Stephan et al, 2021), we further compare with linear Fourier analysis the appearance of convectively coupled equatorial wave activities between the observation and 9km and 4.4km simulations (Figure 16), following the methodology of Takayabu (1994) and Wheeler and Kiladis (1999). Several previous studies also evaluated the representation of equatorial waves in IFS simulations (Dias et al., 2018; Bengtsson et al., 2019). For the equatorially symmetric components of tropical convection (Figures 16a–c), the IFS simulations at both resolutions can simulate Kelvin waves separated from the MJO, whereas the amplitudes of equatorial Rossby waves and tropical depression-type disturbances (i.e., westward-propagating systems in several-day periods) are somewhat underestimated especially in the 4.4km simulation. Meanwhile, the representation of the equatorially antisymmetric wave modes are significantly improved in the 4.4km simulation; both  $n = 0$  eastward inertia-gravity waves and mixed Rossby-gravity waves can be reproduced with amplitudes as large as in the observation.



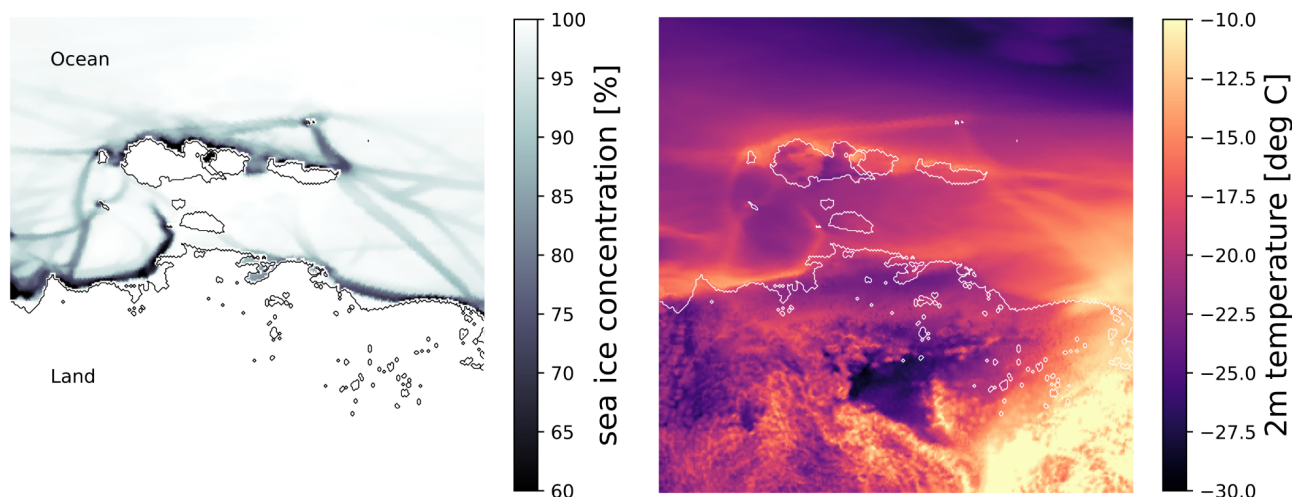
795

796 **Figure 16: Wavenumber-frequency power spectra of equatorially (a-c) symmetric and (d-f) antisymmetric components**  
 797 **of tropical convection measured by OLR anomalies in (a, d) observations, (b, e) IFS 9km simulation with NEMO, and**  
 798 **(c, f) IFS 4.4km simulation with FESOM.** Power spectra are summed from 15°S to 15°N, and plotted as the ratio of raw to  
 799 background power. Abbreviations of WIG, TD, ER, MRG, and EIG indicate westward inertia-gravity waves, tropical  
 800 depressions, equatorial Rossby waves, mixed Rossby-gravity waves, and eastward inertia-gravity waves, respectively.  
 801 Dispersion curves for corresponding equatorial waves are plotted for equivalent depths  $h = 12, 25,$  and  $50$  m.  $n$  denotes the  
 802 number of meridional modes.

## 803 4.2 Sea ice imprint on the atmosphere

804 Leads are narrow open areas in the sea ice cover that typically form after deformation events, such as caused by a persisting  
 805 Arctic storm over the ice cover. Individual leads can form typical ‘linear’ channels of several kilometres length, while the  
 806 larger connected lead systems can extend up to hundreds of kilometres (Overland et al. 1995) or even cross the entire Arctic.  
 807 They are detectable in satellite synthetic-aperture radar images (von Albedyll et al. 2023). Especially in winter, open leads can

808 significantly impact the stability of the atmospheric column and other atmospheric parameters above them. A change in sea  
809 ice cover of 1% can cause near-surface temperature responses around 3.5 K (Lüpkes et al., 2008).



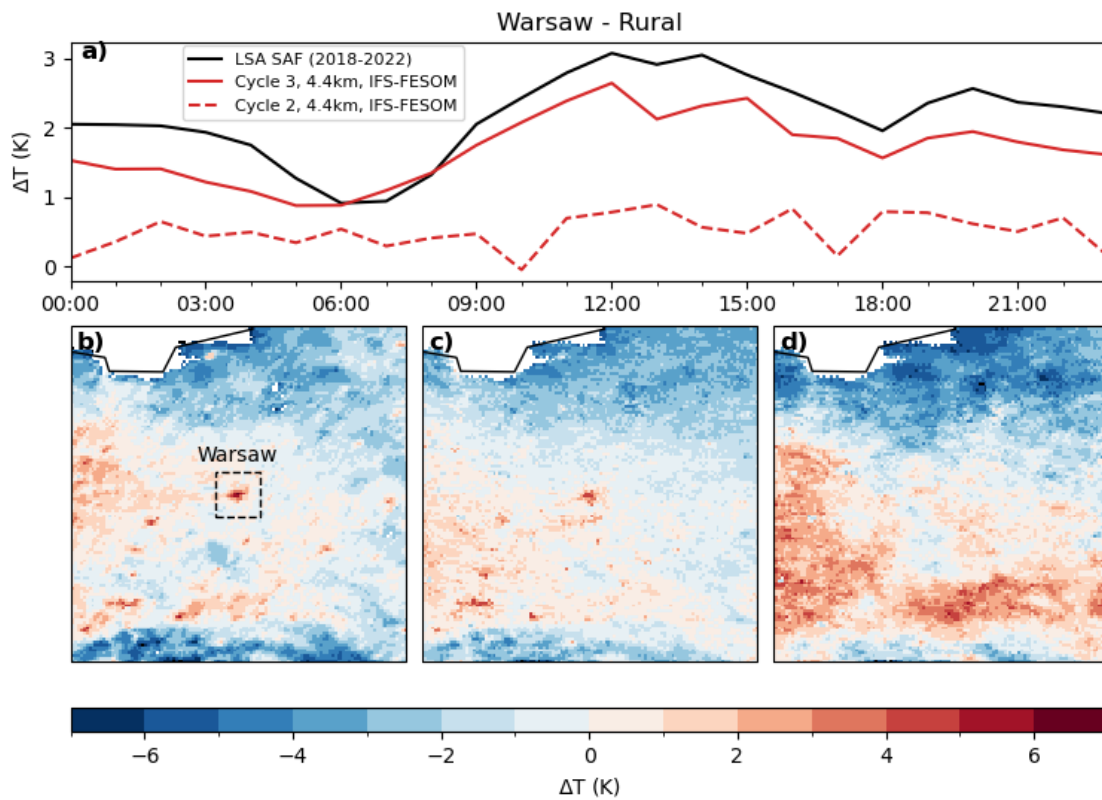
810

811 **Figure 17: Imprint of simulated Arctic sea ice leads on 2m-temperature in the Laptev Sea and East Siberian Sea.** (left)  
812 Sea ice concentration field, (right) 2m-temperature field. The panels depict 13 February 2020, 08:00, in the IFS-FESOM Cycle  
813 3 simulation with TCo2559 (4.4 km), coupled to the NG5 ocean (~4-5 km resolution in this area). The black and white contour  
814 lines represent the border between land and ocean areas.

815 At the km-scale resolution employed here, there is first evidence of resolved linear kinematic features in the sea ice cover at a  
816 grid-spacing of ~4-5km in our coupled simulations (ECMWF News Item, 2022). With resolutions of 4.4km and 2.8km, the  
817 atmosphere can thus ‘see’ these narrow features in the sea ice cover and simulate a response explicitly. Similar to the effect  
818 that meso-scale ocean eddies can have on the atmosphere above them (Frenger et al. 2013), we find that the leads in sea ice  
819 can strongly modulate the atmospheric state above them in our simulations. To give an example from the Arctic winter, north  
820 of Siberia in the Laptev and East Siberian Sea, due to the relatively warm ocean compared to the atmosphere, 2m-temperature  
821 anomalies over sea ice leads can often reach 10–20K against the surrounding closed sea ice cover background (Fig. 17). While  
822 the realism with respect to the size, number, spatial distribution, and orientation of the simulated leads still needs to be  
823 quantified (Hutter et al. 2022), the direct simulation of sea ice lead effects within a coupled km-scale climate model is entirely  
824 novel and opens up new areas of research. Potential climate impacts of this air-ice-ocean interaction on the atmospheric  
825 column, such as Arctic clouds (Saavedra Garfias et al., 2023), will be one focus of our future work.

826 **4.3 Cities and urban heat island effects**

827 Between Cycles 2 and 3, significant improvements have been achieved in representing urban heat island effects around the  
828 globe at the km-scale (Fig. 18). To give an example, the difference in land surface temperature (LST) between the city of  
829 Warsaw and its more rural surroundings during the 5-year clear-sky hours (in the JJA season) depicts a clear urban heat island  
830 effect (Fig. 18, a), with temperature anomalies compared to the rural areas in exceedance of typically 1K over any given day,  
831 and exceeding 2K around noon. When comparing with observations from the Satellite Application Facility on Land Surface  
832 Analysis (LSA SAF) LST product (Trigo et al. 2008), the results in Cycle 3 show a closer fit to the satellite product than was  
833 possible in Cycle 2; both the average temperature difference over the day, as well as its temporal variability, is better captured  
834 (Fig. 18, a).



835  
836 **Figure 18: Diurnal cycle of land surface temperature (LST) difference between the city of Warsaw and its rural**  
837 **surroundings**, for a) the summer months (JJA) during clear-sky conditions (5-year mean). The IFS 4.4km simulations are  
838 given with red lines (Cycle 2 dashed, Cycle 3 solid), observations from LSA SAF are given in black. The bottom panels show  
839 JJA-mean clear-sky LST anomaly maps at 13:00 local time, with respect to the surrounding rural LST average, for b)

840 observations from LSA SAF, for c) IFS 4.4km Cycle 3 with urban scheme, and for d) IFS 4.4km in Cycle 2 without urban  
841 scheme and using older land use/land cover maps.

842

843 Although the sub-diurnal variability is qualitatively well represented, the Cycle 3 modelled urban-rural contrast is  
844 systematically around 0.5 K smaller than in observations. We hypothesise that missing anthropogenic heating as well as an  
845 underestimation of the urban heat storage due to too low urban cover or building height may explain some of the discrepancies.  
846 In terms of spatial variability of LST JJA-mean clear-sky anomalies, our Cycle 3 4.4km IFS simulation (year 2020) matches  
847 km-scale details of the LSA SAF dataset (2018-2022) well (compare Fig. 18, b & c), while Cycle 2 4.4km IFS cannot provide  
848 this local detail in the absence of updated land use/land cover maps plus urban scheme (Fig. 18, d). Note also that the changes  
849 in high and low vegetation cover and vegetation types in Cycle 3 impact positively on the areas found to be too warm in Cycle  
850 2 in the South and East of Warsaw. These results illustrate clearly that high-resolution surface information as well as an urban  
851 scheme will be necessary in the context of the increasing need for local climate information on a city scale, and for local  
852 projections of direct socio-economic relevance.

## 853 **5 Summary and Conclusions**

854 In this paper, storm- and eddy-resolving simulations performed with the nextGEMS configurations of the ECMWF Integrated  
855 Forecasting System have been described and analysed. While we have also presented eddy-permitting simulations with IFS-  
856 NEMO as the ECMWF operational baseline configuration, we have focused mostly on IFS-FESOM runs that feature not only  
857 the highest atmospheric resolution (4.4km and also 2.8km) but also an eddy-resolving ocean at 5km. The large-scale  
858 performance in terms of the mean state has been presented, such as top-of-the atmosphere radiation balance and surface  
859 temperature biases, but also important variability patterns (e.g. MJO and QBO) that can be analysed in 5-year long simulations.  
860 The illustrated set of emerging advances in the km-scale nextGEMS simulations are first indications of the added value of km-  
861 scale modelling and explicit simulation of smaller scales. We expect to be able to show more of these examples once longer  
862 simulations will be available from the multi-decadal production simulations planned in nextGEMS for 2024/2025. In this study  
863 it is the first time that the model configuration and quality of the simulations with IFS-FESOM have been described; and it  
864 thus represents a significant milestone both in terms of documenting this novel model capability and the scientific readiness  
865 of the coupled modelling system.

866

867 A number of model advances delivered in the nextGEMS development cycles improved the realism of the km-scale  
868 simulations. For example, activating mass fixers for water vapour, cloud liquid, ice, rain, and snow made global water non-  
869 conservation negligible and reduced energy non-conservation to an amount that is acceptable for long climate simulations.  
870 Importantly, global water conservation turns out to be beneficial not only for long climate integrations, but also for the quality  
871 of ECMWF's medium-range weather forecasts. Work for ECMWF's recent operational IFS upgrade in June 2023 (48r1)



872 showed that the model changes performed to fix the water and energy imbalances reduce the overestimation of mean  
873 precipitation at different timescales and improve the skill scores for the recent operational resolution upgrade for medium-  
874 range ensemble weather forecasts (ECMWF Newsletter 172, 2022). For example, in 9km forecasts where we ensured global  
875 water conservation the mean absolute error of precipitation against rain gauge measurements is about 2–3% smaller. This is a  
876 great example of a model development from the nextGEMS multi-year simulations feeding into the improvement of the  
877 operational NWP system at ECMWF.

878

879 Variability patterns that could be studied with the 5-year nextGEMS simulations so far are the Madden-Julian Oscillation  
880 (MJO) and the Quasi-Biennial Oscillation (QBO) in the equatorial stratospheric winds. The QBO is simulated with reasonable  
881 periodicity, which is typically challenging for km-scale models without any active parametrization for deep convection. The  
882 remaining deficiencies we explained are likely due to the overly active vertical diffusion parametrization in stable conditions,  
883 which will be addressed in an upcoming version of the IFS. The MJO is similarly well represented in both the 9km and 4.4km  
884 simulations. However, the MJO convective envelopes are continuously organised in the 4.4km simulation when they propagate  
885 over the Maritime Continent, which is in better agreement with observations. We think that this is not just an effect of sampling  
886 different numbers of MJO events in our simulations and in the observations (simulated 5-year periods at 9km and 4.4km  
887 resolution versus long-term observational period) since the observed MJO for shorter periods of time (e.g., 2011-2015) shows  
888 a similar result to the full observational record. The realistic representation of tropical variability and wave activity in the IFS  
889 at 9km and 4.4km is the result of 15 years of sustained efforts in model developments, notably convection, cloud-radiation  
890 interaction, and air-sea coupling (Bechtold et al. 2008, Dias et al 2018). The documented additional improvements in the 4.4km  
891 simulation compared to 9km may result from reduced cloud base mass fluxes (i.e., more weight on explicit convection), but  
892 further detailed study of this subject is part of our future work.

893

894 With our km-scale simulations that resolve mesoscale ocean eddies over large parts of the globe, we can also investigate  
895 coupled effects between sea ice leads, open narrow channels in the sea ice cover, and the atmosphere above them for the first  
896 time. Leads form during deformation events and can span over distances from several to hundreds of kilometres. From limited  
897 observations and field campaigns it is known that sea ice leads can significantly impact the stability and temperature of the  
898 atmospheric column, especially in winter. We find that our model can resolve the linear features of the leads and represent  
899 explicitly the resulting heating of the atmosphere. This is a novel and promising approach that reveals new aspects of the air-  
900 ice-ocean interaction.

901

902 The nextGEMS model configurations are also starting points for the Climate Adaptation Digital Twin in DestinE, which aims  
903 to provide local climate information, for instance at the scale of cities, globally. The urban heat island effect, which is the  
904 phenomenon of higher temperatures in urban areas compared to rural areas, is an aspect of socio-economic importance that  
905 will need to be accurately represented by km-scale models in the future. In this study, we have shown that the implementation

906 of an urban scheme in the IFS for nextGEMS Cycle 3 can significantly improve the simulation of land surface temperature  
907 (LST) over urban areas around the world, compared to previous model cycles that were missing specific urban tiles. The  
908 example of Warsaw illustrates the improvement in both temporal and spatial variability of land surface temperatures when  
909 compared to observations. We have also identified some limitations, such as nocturnal LST differences, which may be related  
910 to the lack of some anthropogenic heating in the model. Our first results here demonstrate the necessity and benefit of using  
911 an urban scheme in km-scale models for future efforts to provide reliable local climate information at the city scale.

912

913 While kilometre-scale model resolution is of benefit for the representation of the atmosphere, ocean, sea ice and land, it is also  
914 of importance for our understanding of other components of the climate system that have not been covered in this study yet,  
915 such as deep ocean circulation and ice sheet behaviour. For example, ocean heat transport at depth towards the Antarctic ice  
916 sheet and ice-shelf cavities is localised in narrow canyons (Morrison et al. 2020). To resolve bathymetric features like this and  
917 their potentially far-reaching impacts could be a strength of high-resolution models. Another example is the equilibration of  
918 the Antarctic Circumpolar Current, which is a balance of the wind-driven circulation and the opposing eddy-induced  
919 circulation cells. While transient ocean eddies can be parametrized to some degree, the effect of standing eddies (or meanders  
920 of this current) are beyond what parametrizations can achieve (Bryan et al., 2014). First studies indicate that explicit simulation  
921 of these effects with km-scale ocean models might be warranted to achieve higher confidence in projections of the Southern  
922 Ocean and global sea level rise (van Westen and Dijkstra, 2021; Rackow et al. 2022).

923

924 We have demonstrated that kilometre-scale modelling, which will soon enable multi-decadal simulations, has become feasible  
925 and offers advantages over lower-resolution models. At the scales used in this study, some modified subgrid parameterizations  
926 (e.g. deep convection with reduced cloud base mass flux) are still active for best performance, even though the influence of  
927 resolved-scale horizontal and vertical motions increases. The results presented here prove that our seamless model  
928 development approach, where numerical weather prediction models are extended for km-scale multi-decadal climate  
929 applications, is useful (Randall and Emanuel, 2024) and can benefit the original NWP application as well. As we have shown  
930 by running those models for 5 years, the km-scale simulations improve the representation of atmospheric circulation and  
931 extreme precipitation, but also enhance the coupling between the atmosphere, land, urban areas, ocean, and sea ice. We have  
932 revealed novel interactions among these components for the first time that will be further explored in ongoing work. With  
933 upcoming multi-decadal simulations from the nextGEMS and DestinE projects we will be able to generate even more statistics  
934 on km-scale modelling soon, with an extended set of simulations from several models. These projects aim to provide accurate  
935 and globally consistent information on local climate change - at the scales that matter for individual cities or local impact  
936 modelling.

937

938

939

940 **Appendix A - Conservation properties of the IFS advection scheme and mass fixer approach**

941 The IFS uses a semi-Lagrangian (SL) advection scheme which is stable for long timesteps and essential for the efficiency of  
942 the overall model. It is also multi-tracer efficient as many fields can be transported with a relatively small overhead: to advect  
943 a field (e.g. temperature, wind components, tracers), the upstream departure locations of the model grid-points are computed  
944 but these are the same for all fields. The only remaining task is then to find the value of each field by interpolation to the  
945 departure location (for details, see Diamantakis and Váňa 2021). However, despite being accurate and efficient, the transport  
946 scheme lacks local and global conservation. In the absence of sources/sinks, the global mass of a tracer should remain constant,  
947 however, SL advection changes slightly its global mass. This change depends strongly on the spatial characteristics of the  
948 tracer such as smoothness of the field and its geographic location, with larger conservation errors for tracers that have sharp  
949 gradients and interact with the orography.

950

951 Conservation properties are important for water and energy budgets, especially for high resolutions. A practical solution that  
952 restores the global mass conservation of water tracers without altering the efficient and accurate numerical formulation of the  
953 IFS, is the mass fixer approach. However, simple mass fixers which change each tracer gridpoint value by the same proportion  
954 may result in unwanted biases in some regions. Hence, a more “local” approach is applied in the IFS advection scheme, which  
955 was originally developed and tested for atmospheric composition tracers yielding accurate results when compared against  
956 observations (Diamantakis and Fleming 2014, Diamantakis and Agusti-Panareda 2017). This is a “weighted” approach as the  
957 correction of the tracer field at each grid point depends on a weight factor which is proportional to a local error measure. The  
958 correction restores global conservation, using local criteria and it also preserves positive definiteness and monotonicity of the  
959 field.

960

961

962

963

964

965

966

967

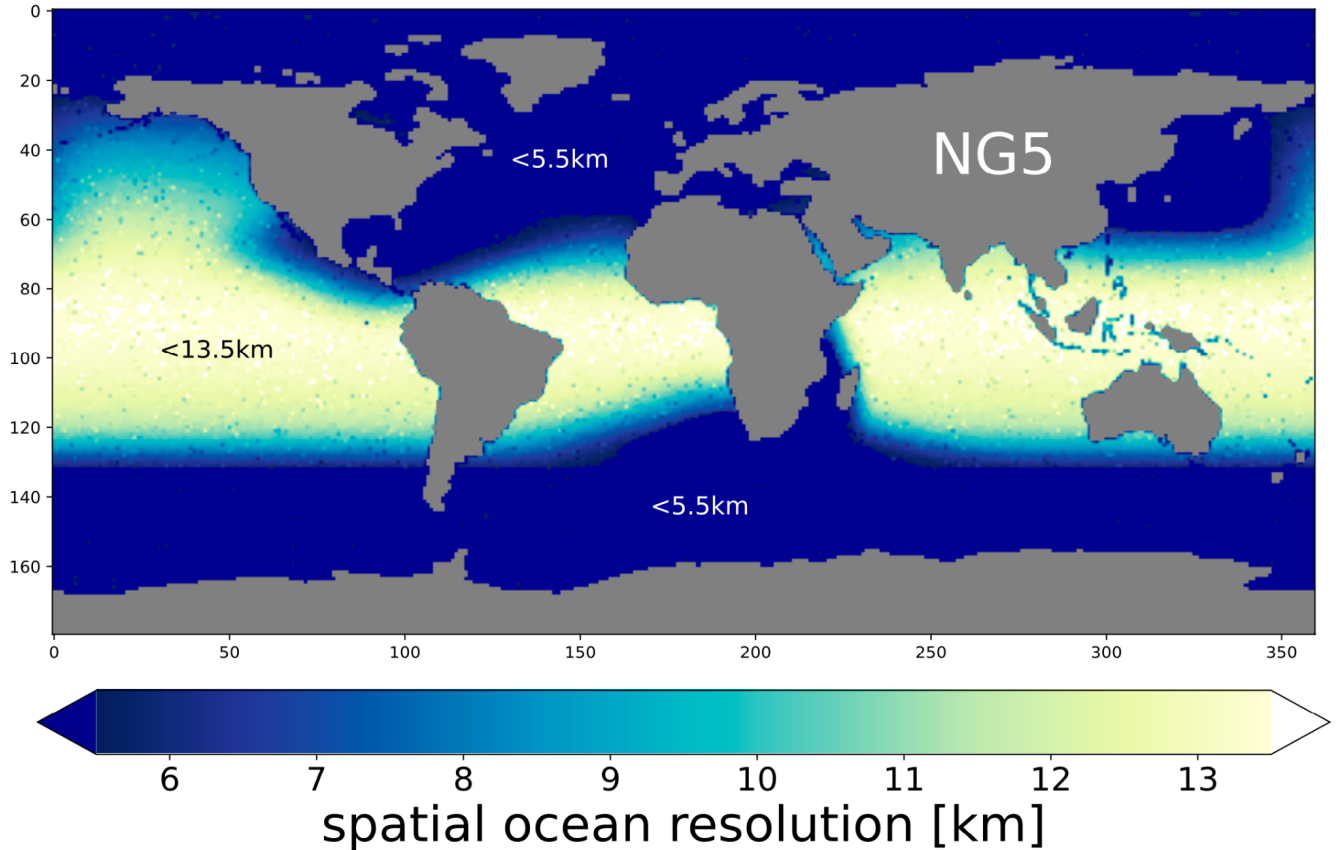
968

969

970 **Appendix B**

971 The 5km nextGEMS ocean grid in this study (termed 'NG5') makes use of the multi-resolution mesh capabilities provided by  
972 the FESOM ocean-sea ice model (Figure B1). From nextGEMS Cycle 2 and following cycles, FESOM was run with this new  
973 eddy-resolving ocean grid with spacing of less than ~5km (at the poles) and around 13km in the tropics. This grid, specifically  
974 designed by the Alfred Wegener Institute (AWI) to better match the high atmospheric resolution of 4.4km in the IFS, allows  
975 to better resolve areas of particular interest at higher resolution, such as the Western boundary currents or the Southern Ocean.  
976 The mesh was created with the JIGSAW-GEO package (Engwirda, 2017).

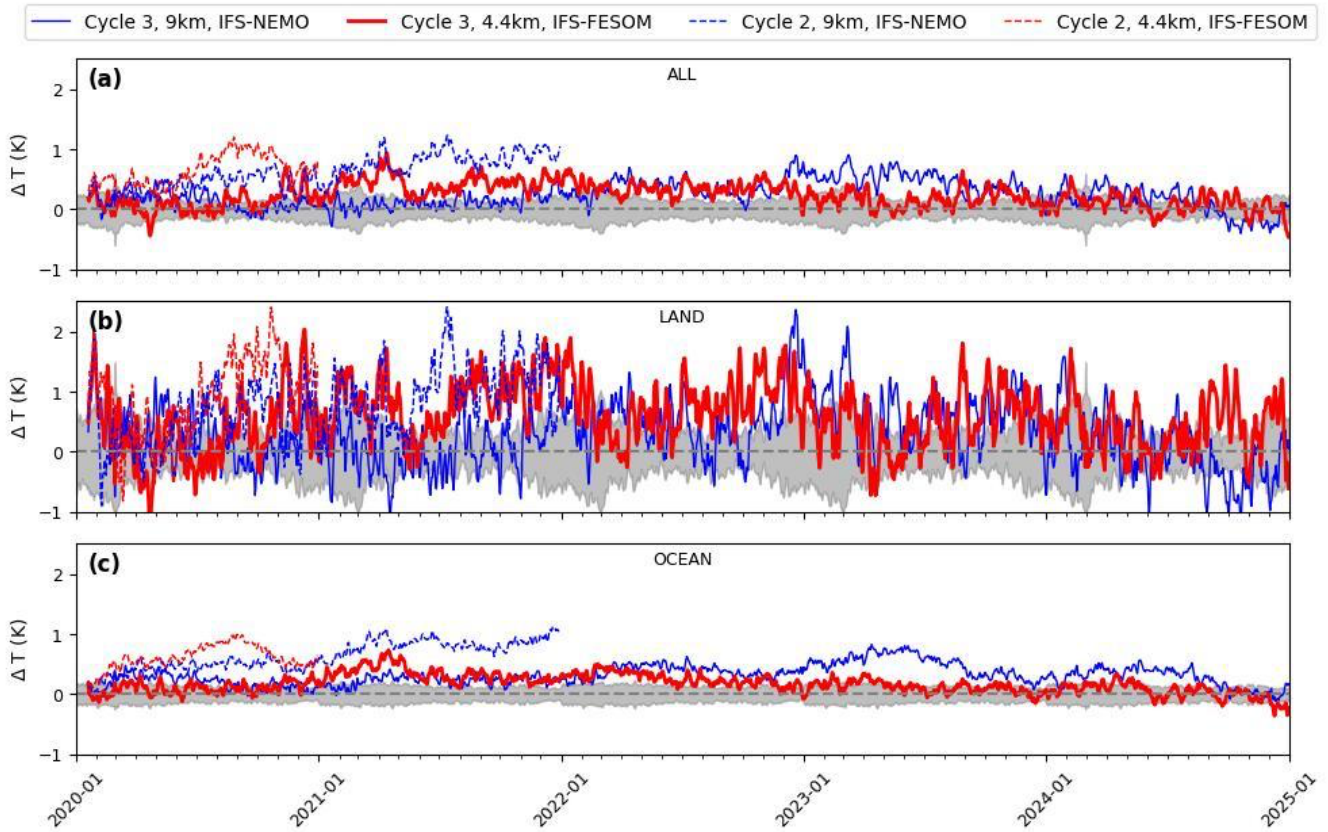
977



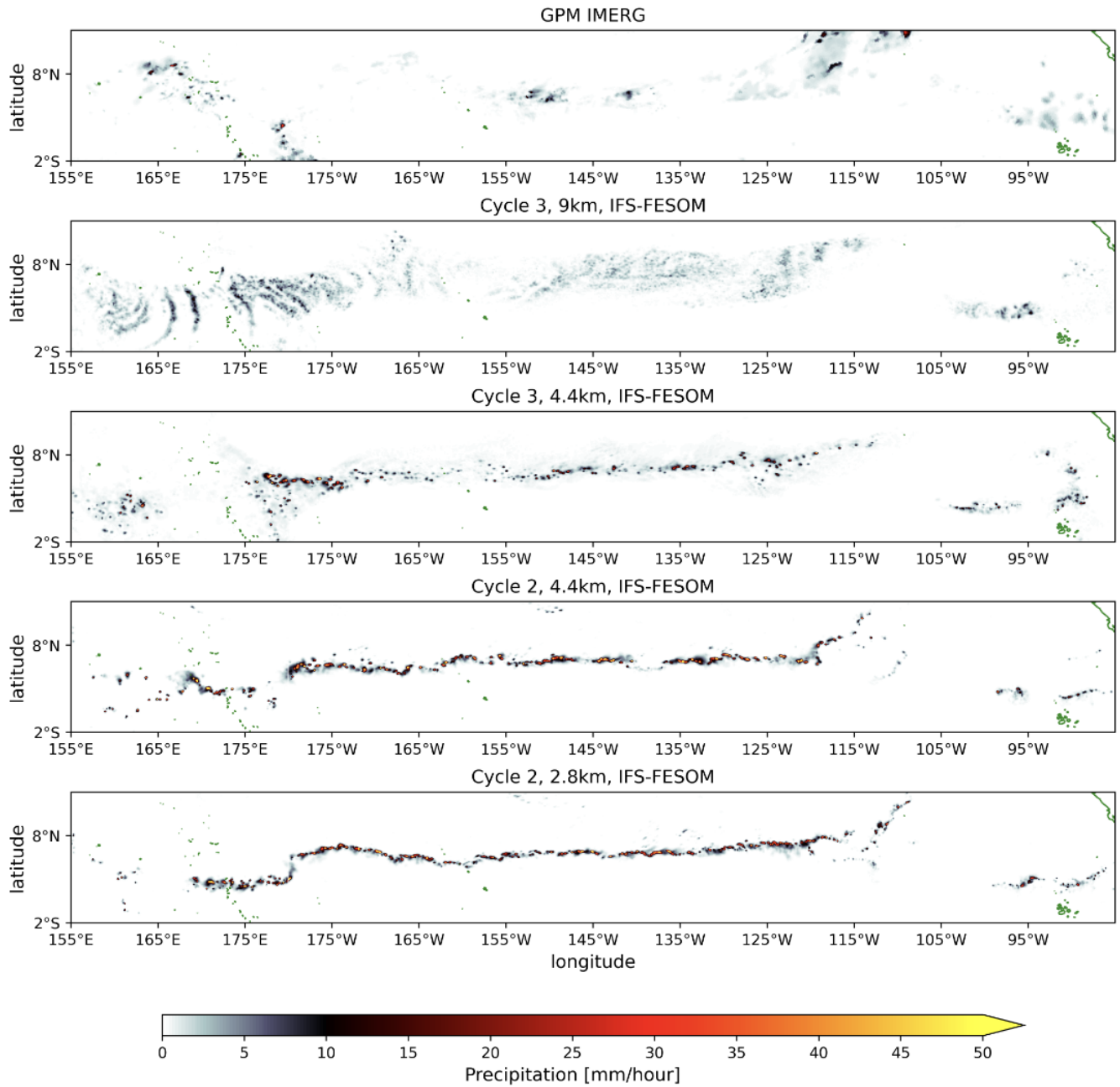
978

979

**Figure B1: Spatial ocean resolution in the nextGEMS 5km grid, NG5 [km].**



981 **Figure C1: Timeseries of mean 2-metre temperature in nextGEMS simulations for (a) global, (b) only over land, and**  
 982 **(c) only over ocean with respect to ERA5, for the years 2020-2024. The shaded area shows the ERA5 standard deviation**  
 983 **between 2012-2021.**



985

986

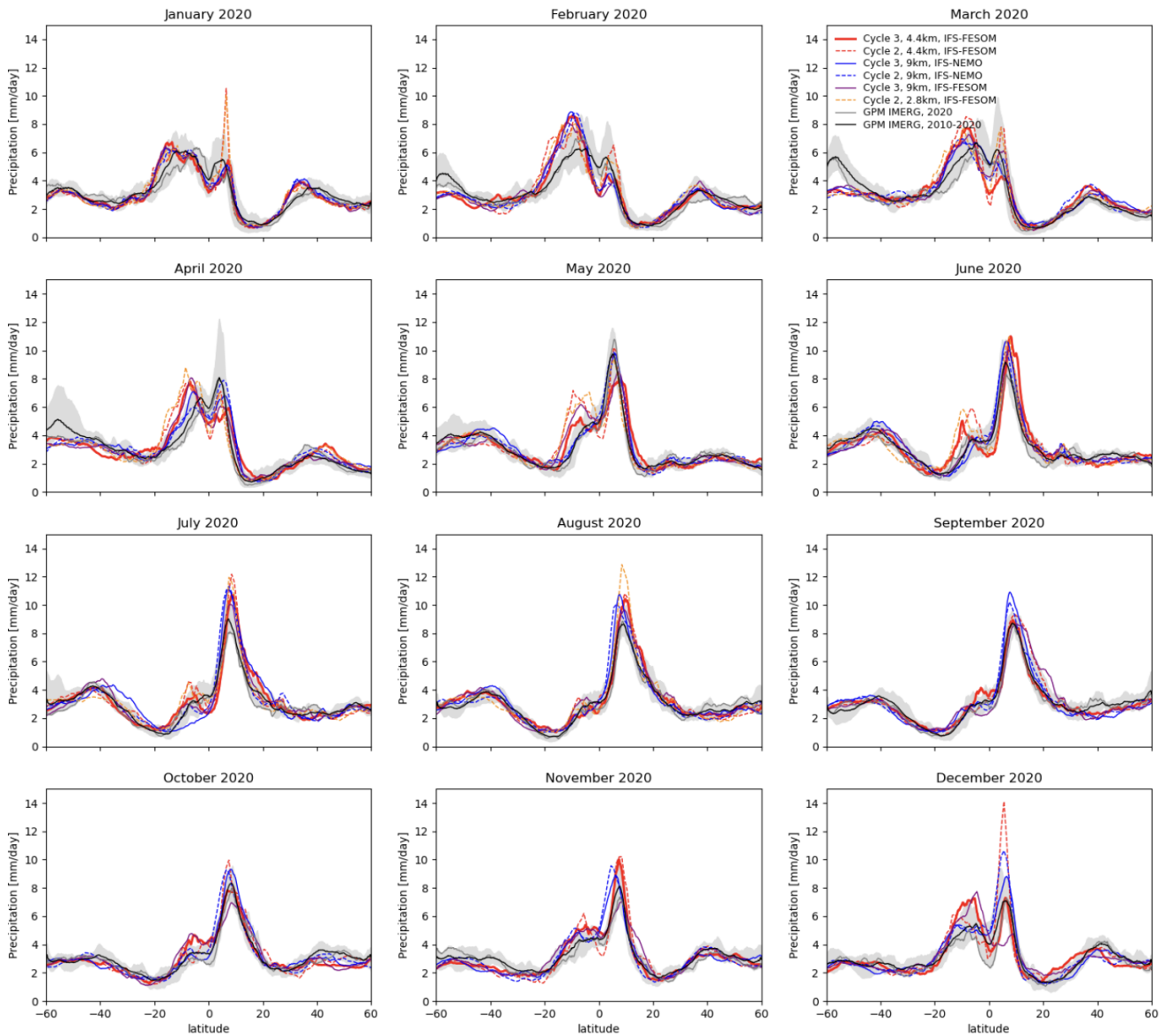
987

988

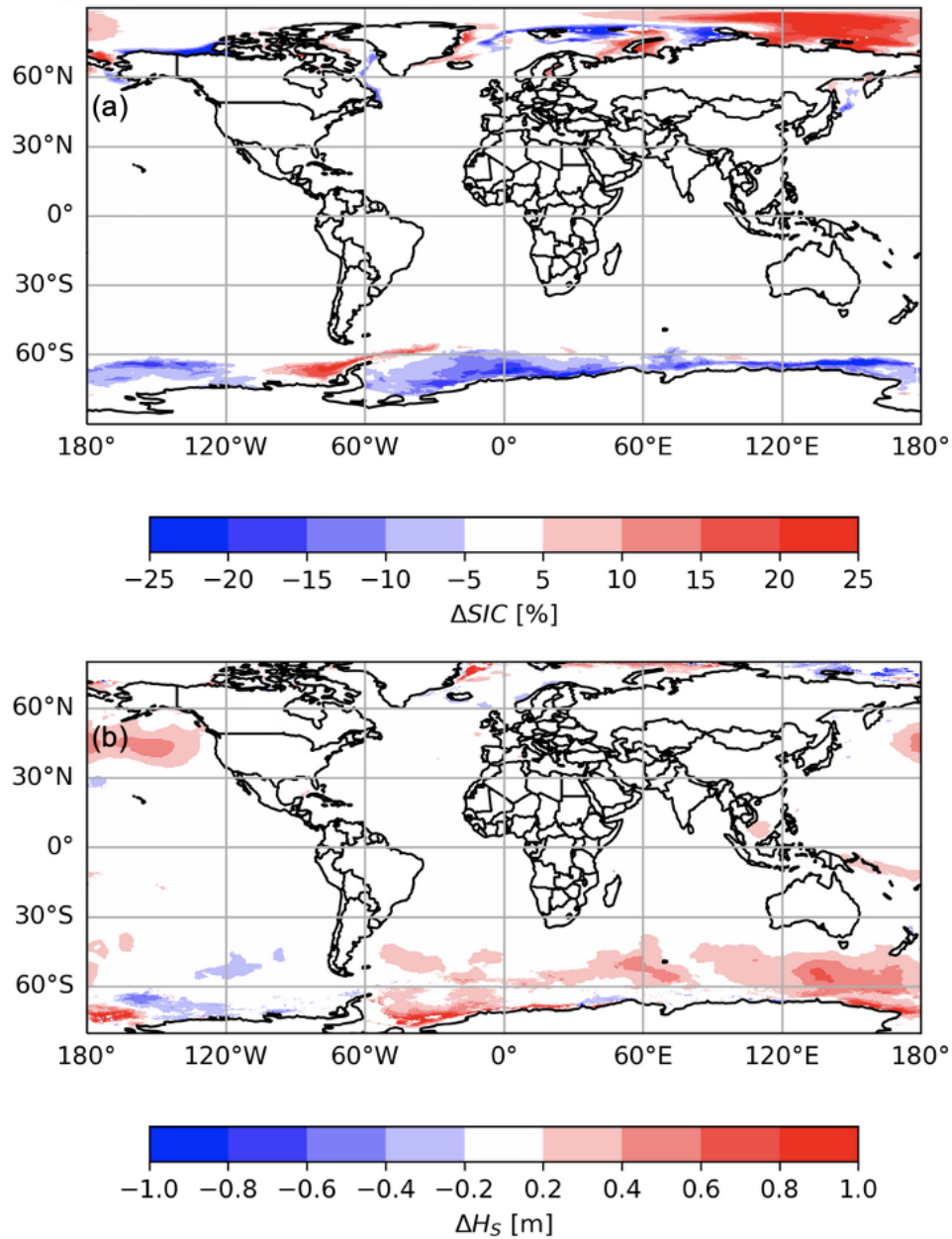
**Figure D1: Snapshots of precipitation in nextGEMS Cycle 2 and 3 simulations in the tropical Pacific at 5°N, compared to observations from GPM IMERG.** The ITCZ often organises into a continuous and persistent line of deep convection over the Pacific at 5°N in Cycle 2 at 4.4km and 2.8km resolution (lower two panels), with strongly overestimated zonal mean

989 precipitation along this latitude. In Cycle 3 this has been addressed via a reduced cloud-base mass flux with 4.4km resolution.  
 990 The 9km Cycle 3 simulation uses active deep convection parametrization (Deep On).

991  
 992



993  
 994 **Figure D2: Zonal-mean precipitation for the individual months in the first year of Cycle 2 (dashed) and Cycle 3 (solid)**  
 995 **simulations.** IFS-NEMO 9km simulations are in blue, while IFS-FESOM simulations are given in red (4.4km), orange  
 996 (2.8km), and purple (9km).



998

999 **Figure E1: Mean changes in (a) sea ice concentration and (b) significant wave height between the 4.4km and 9km IFS-**  
 1000 **FESOM simulations in nextGEMS Cycle 3 (4.4km minus 9km). Red (blue) indicates an increase (decrease) for the 4.4km**  
 1001 **simulation.**



## 1002 **Code Availability**

1003 The FESOM2.5 model is a free software and available from Github (<https://github.com/FESOM/fesom2>). The latest version 2.5 including  
1004 all developments used in nextGEMS Cycle 3 is archived in a Zenodo repository, <https://doi.org/10.5281/zenodo.10225420> (Rackow et al.  
1005 2023c). The ocean coupling interface to the Integrated Forecasting System (IFS) has been extracted for IFS-FESOM and is publicly available  
1006 as part of the FESOM2.5 code above as well (folder `ifs_interface`). MultiIO, MIR, ECCODES and FDB are all free software and available at  
1007 the ECMWF Github space, <https://github.com/ecmwf>. The IFS source code is available subject to a licence agreement with ECMWF.  
1008 ECMWF member-state weather services and approved partners will be granted access. The IFS code without modules for data assimilation  
1009 is also available for educational and academic purposes via an OpenIFS licence (see <http://www.ecmwf.int/en/research/projects/openifs>).  
1010 For easier public access and review, the IFS code modifications from this study and developments detailed in section 3.1.1 for nextGEMS  
1011 have also been separately archived in a Zenodo repository, <https://doi.org/doi/10.5281/zenodo.10223576> (Rackow et al. 2023b). Scripts and  
1012 data to reproduce the figures and analysis of this paper can be found at <https://github.com/trackow/nextGEMS-paper/>. Grib data in FDB  
1013 were made available to hackathon participants using gribscan (Kölling, Klufft, and Rackow, 2024).

## 1014 **Data Availability**

1015 Data for our simulations are openly accessible and can be obtained either from the web (see DOIs below), from ECMWF's MARS archive,  
1016 or directly from DKRZ's supercomputer Levante after registration (<https://luv.dkrz.de/register/>). The Cycle 2 data for 20 January 2020 to 31  
1017 December 2020 of TCo2559-NG5 with deep convection parametrization disabled can be found at <https://dx.doi.org/10.21957/1n36-qg55>.  
1018 The Cycle 2 data for TCo1279-ORCA025 (20 Jan 2020 to 31 December 2021) with deep convection parametrization active can be found at  
1019 <https://dx.doi.org/10.21957/x4vb-3b40>. More Cycle 2 output, also for the nextGEMS sister model ICON, can be found at the World Data  
1020 Center for Climate (WDCC), [https://dx.doi.org/10.26050/WDCC/nextGEMS\\_cyc2](https://dx.doi.org/10.26050/WDCC/nextGEMS_cyc2). Cycle 3 data for ICON and IFS can be found WDCC  
1021 under [https://doi.org/10.26050/WDCC/nextGEMS\\_cyc3](https://doi.org/10.26050/WDCC/nextGEMS_cyc3) (Koldunov et al. 2023). Namelist files to reproduce the settings of the ocean,  
1022 atmosphere, land, and wave model in the Cycle 3 simulations are archived in a Zenodo repository (Rackow et al. 2023a),  
1023 <https://doi.org/10.5281/zenodo.10221652>. LSA SAF LST data are available from the LSA SAF data service under the link  
1024 <https://datalsasaf.lsasvcs.ipma.pt/PRODUCTS/MSG/MLST/>. Observed SSH AVISO data are taken from  
1025 <http://marine.copernicus.eu/services-portfolio/access-to-products/> (last access 7 September 2024). The ocean mixed-layer climatology is  
1026 from de Boyer Montégut Clément (2023), accessed from the SEANOE repository (<https://doi.org/10.17882/91774>).

## 1027 **Author contributions**

1028 TR led the writing of the paper and prepared the initial manuscript with TB and XPB. TR, TB, XPB, and IH performed the simulations. TB,  
1029 XPB, RF, MD and TR developed the model code changes. The refactoring of the FESOM model has been led by DSi, NK, JS, PS, and JH.  
1030 Initial implementation of the IFS-FESOM single-executable coupling is joint work of KM and TR with support from CK. NK created the  
1031 5km nextGEMS FESOM grid NG5 in discussions with TR. IP performed the QBO analysis. TB has analysed the precipitation characteristics  
1032 and performed the TOA tuning. XPB contributed the 5-year temperature timeseries. SM performed TOA budget analyses. DT performed  
1033 the MJO analyses. JB and JK contributed the wave model analyses. The city and urban heat island analyses are by XPB and ED. RG  
1034 performed the SSH analyses. AK performed the mixed-layer analysis. Sea ice performance indices are the work of LZ. TR performed the

1035 sea ice lead analysis. HFG provided ocean grid descriptions for coupling weight computations. In the paper, MD and CK discussed the mass  
1036 fixer approach and RF discussed the physics parametrizations. DSá added the multiIO section to the paper. TK, LK, and FZ helped with  
1037 faster data access. PM developed necessary software tools, in particular MIR. All co-authors discussed and contributed to the final document.

## 1038 **Competing Interests**

1039 The authors declare that they have no conflict of interest.

## 1040 **Acknowledgements**

1041 This work used supercomputing resources of the German Climate Computing Centre (Deutsches Klimarechenzentrum, DKRZ) granted by  
1042 its Scientific Steering Committee (WLA) under project ID 1235. We want to thank DKRZ staff for their continued support in terms of data  
1043 handling, data hosting, and running of the presented Cycle 3 simulations, in particular Jan Frederik Engels, Hendryk Bockelmann, Fabian  
1044 Wachsmann, Irina Fast, and Carsten Beyer. We want to thank colleagues at AWI for active discussions and their support towards the  
1045 upcoming multi-decadal simulations, in particular Suvarchal Kumar Cheedela, Bimochan Niraula, and Sergey Danilov.. We also would like  
1046 to thank all colleagues at ECMWF who are not co-authors but also had a substantial impact on km-scale model development and modelling  
1047 on climate timescales, e.g. Gabriele Arduini, Gianpaolo Balsamo, Magdalena Alonso Balmaseda, Margarita Choulga, Jasper Denissen, Joe  
1048 McNorton, Simon Smart, James Hawkes, Philipp Geier, Charles Pelletier, Andreas Mueller, Michael Lange, Olivier Marsden, Sam Hatfield,  
1049 Matthew Griffith, Shannon Mason, and Mark Fielding. We thank Philippe Lopez for providing the Meteosat 8 observations in Figure 6. We  
1050 also want to thank the international nextGEMS hackathon community, including many Early Career Researchers, who analysed our  
1051 simulations in detail and helped guide some of the model development efforts. This research has been supported by the European  
1052 Commission Horizon 2020 Framework Programme nextGEMS (grant no. 101003470). This work was also supported by the European  
1053 Union's Destination Earth Initiative and relates to tasks entrusted by the European Union to the European Centre for Medium-Range Weather  
1054 Forecasts implementing part of this Initiative with funding by the European Union.

## 1055 **References**

1056 Ahn, M. S., Kim, D., Kang, D., Lee, J., Sperber, K. R., Gleckler, P. J., ... & Kim, H. (2020). MJO propagation across the  
1057 Maritime Continent: Are CMIP6 models better than CMIP5 models?. *Geophysical Research Letters*, 47(11), e2020GL087250.  
1058  
1059 Arduini, G., Balsamo, G., Dutra, E., Day, J. J., Sandu, I., Boussetta, S., & Haiden, T. (2019). Impact of a multi-layer snow  
1060 scheme on near-surface weather forecasts. *Journal of Advances in Modeling Earth Systems*, 11, 4687–4710.  
1061 <https://doi.org/10.1029/2019MS001725>  
1062  
1063 Baldwin, M. P., et al. (2001), The quasi-biennial oscillation, *Rev. Geophys.*, 39(2), 179–229, doi:10.1029/1999RG000073.  
1064

1065 Bauer, P., Quintino, T., Wedi, N., Bonanni, A., Chrust, M., Deconinck, W., ... & Zanna, C. (2020). The ECMWF scalability  
1066 programme: Progress and plans. European Centre for Medium Range Weather Forecasts. <https://doi.org/10.21957/gdit22ulm>  
1067

1068 Bauer, P., Dueben, P.D., Hoefler, T., Quintino, T., Schulthess, T., Wedi, N.P. The digital revolution of Earth-system science.  
1069 *Nat Comput Sci* 1, 104–113 (2021). <https://doi.org/10.1038/s43588-021-00023-0>  
1070

1071 Bauer, P., Quintino, T., and Wedi, N.P. (2022) From the Scalability Programme to Destination Earth, ECMWF Newsletter,  
1072 issue 171, pp. 15-22. DOI: 10.21957/pb2vnp59ks  
1073

1074 Bechtold, P., M. Köhler, T. Jung, M. Leutbecher, M. Rodwell, F. Vitart and G. Balsamo (2008). Advances in predicting  
1075 atmospheric variability with the ECMWF model: From synoptic to decadal time-scales. *Quart. J. Roy. Meteor. Soc.* 134,  
1076 1337-1351  
1077

1078 Bechtold, P., N. Semane, P. Lopez, J.-P. Chaboureau, A. Beljaars, and N. Bormann (2014). Representing equilibrium and  
1079 non-equilibrium convection in large-scale models. *J. Atmos. Sci.*, 134, 1337-1351, <https://doi.org/10.1175/JAS-D-13-0163.1>.  
1080

1081 Becker, T., Bechtold, P. and Sandu, I., 2021: Characteristics of convective precipitation over tropical Africa in storm-  
1082 resolving global simulations. *Quarterly Journal of the Royal Meteorological Society*, 147(741), pp.4388-4407.  
1083 <https://doi.org/10.1002/qj.4185>  
1084

1085 ECMWF Newsletter 172: [https://www.ecmwf.int/en/newsletter/172/news/fixing-water-and-energy-budget-imbalance-](https://www.ecmwf.int/en/newsletter/172/news/fixing-water-and-energy-budget-imbalance-integrated-forecasting-system/)  
1086 [integrated-forecasting-system/](https://www.ecmwf.int/en/newsletter/172/news/fixing-water-and-energy-budget-imbalance-integrated-forecasting-system/), last access: 4 January 2024, Summer 2022.

1087 Beljaars, A. C. M., Brown, A. R. and Wood, N. (2004). A new parametrization of turbulent orographic form drag. *Q. J. R.*  
1088 *Meteorol. Soc.*, 130, 1327-1347, <https://doi.org/10.1256/qj.03.73>.

1089 Bengtsson, L, J. Dias, M. Gehne, P. Bechtold, J. Whitaker, J.-W. Bao, L. Magnusson, S. Michelson, P. Pegion, S. Tulich and  
1090 G. Kiladis, 2019 : Convectively coupled equatorial wave simulations using the ECMWF IFS and the NOAA GFS cumulus  
1091 convection schemes in the NOAA GFS model. *Mon. Wea. Rev*, 147, 4005-4025 <https://doi.org/10.1175/MWR-D-19-0195.1>  
1092

1093 Bony, S., Stevens, B., Frierson, D. et al. Clouds, circulation and climate sensitivity. *Nature Geosci* 8, 261–268 (2015).  
1094 <https://doi.org/10.1038/ngeo2398>  
1095

1096 Boussetta, S.; Balsamo, G.; Arduini, G.; Dutra, E.; McNorton, J.; Choulga, M.; Agustí-Panareda, A.; Beljaars, A.; Wedi, N.;  
1097 Munõz-Sabater, J.; et al. ECLand: The ECMWF Land Surface Modelling System. *Atmosphere* 2021, 12, 723.  
1098 <https://doi.org/10.3390/atmos12060723>.  
1099  
1100 Bozzo, A., Benedetti, A., Flemming, J., Kipling, Z., and Rémy, S.: An aerosol climatology for global models based on the  
1101 tropospheric aerosol scheme in the Integrated Forecasting System of ECMWF, *Geosci. Model Dev.*, 13, 1007–1034,  
1102 <https://doi.org/10.5194/gmd-13-1007-2020>, 2020.  
1103  
1104 Bryan, F. O., Gent, P. R., & Tomas, R.: Can Southern Ocean Eddy Effects Be Parameterized in Climate Models?,  
1105 *Journal of Climate*, 27(1), 411-425. Retrieved Dec 20, 2022, from [https://journals.ametsoc.org/view/journals/clim/27/1/jcli-  
1107 d-12-00759.1.xml](https://journals.ametsoc.org/view/journals/clim/27/1/jcli-<br/>1106 d-12-00759.1.xml), 2014.  
1108 Bushell, A.C., Anstey, J.A., Butchart, N., Kawatani, Y., Osprey, S.M., Richter, J.H., Serva, F., Braesicke, P., Cagnazzo, C.,  
1109 Chen, C.-C., Chun, H.-Y., Garcia, R.R., Gray, L.J., Hamilton, K., Kerzenmacher, T., Kim, Y.-H., Lott, F., McLandress,  
1110 C., Naoe, H., Scinocca, J., Smith, A.K., Stockdale, T.N., Versick, S., Watanabe, S., Yoshida, K. and Yukimoto, S. (2022),  
1111 Evaluation of the Quasi-Biennial Oscillation in global climate models for the SPARC QBO-initiative. *QJR Meteorol Soc*,  
1112 148: 1459-1489. <https://doi.org/10.1002/qj.3765>  
1113  
1114 Cao, B., Arduini, G., and Zsoter, E.: Brief communication: Improving ERA5-Land soil temperature in permafrost regions  
1115 using an optimized multi-layer snow scheme, *The Cryosphere*, 16, 2701–2708, <https://doi.org/10.5194/tc-16-2701-2022>,  
1116 2022.  
1117 Chen, G., Ling, J., Zhang, R., Xiao, Z., & Li, C. (2022). The MJO from CMIP5 to CMIP6: Perspectives from tracking MJO  
1118 precipitation. *Geophysical Research Letters*, 49(1), e2021GL095241.  
1119 Crook, J., Klein, C., Folwell, S., Taylor, C.M., Parker, D.J., Stratton, R. and Stein, T. (2019) Assessment of the representation  
1120 of West African storm lifecycles in convection-permitting simulations. *Earth and Space Science*, 6(5), 818–835.  
1121 <https://doi.org/10.1029/2018EA000491>.  
1122 Dai, A., T. Qian, K. E. Trenberth, and J. D. Milliman, 2009: Changes in Continental Freshwater Discharge from 1948 to  
1123 2004. *J. Climate*, 22, 2773–2792, <https://doi.org/10.1175/2008JCLI2592.1>.  
1124 Danilov, S., Sidorenko, D., Wang, Q., and Jung, T.: The Finite-volume Sea ice–Ocean Model (FESOM2), *Geosci. Model*  
1125 *Dev.*, 10, 765–789, <https://doi.org/10.5194/gmd-10-765-2017>, 2017.

1126 de Boyer Montegut Clement, Madec Gurvan, Fischer Albert S., Lazar Alban, Iudicone Daniele (2004). Mixed layer depth  
1127 over the global ocean: An examination of profile data and a profile-based climatology. *Journal Of Geophysical Research-*  
1128 *oceans*. 109 (C12/C12003). 1-20. <https://doi.org/10.1029/2004JC002378>

1129 de Boyer Montégut Clément (2023). Mixed layer depth climatology computed with a density threshold criterion of  
1130 0.03kg/m<sup>3</sup> from 10 m depth value. *SEANOE*. <https://doi.org/10.17882/91774>

1131 Dee, D. P., Uppala, S. M., Simmons, A. J., Berrisford, P., Poli, P., Kobayashi, S., ... & Vitart, F. (2011). The ERA-Interim  
1132 reanalysis: Configuration and performance of the data assimilation system. *Quarterly Journal of the royal meteorological*  
1133 *society*, 137(656), 553-597.

1134 Diamantakis, M. and Váňa, F (2022). A fast converging and concise algorithm for computing the departure points in semi-  
1135 Lagrangian weather and climate models. *Q J R Meteorol Soc*, 148(743), 670–684, <https://doi.org/10.1002/qj.4224>  
1136

1137 Diamantakis, M. and Agusti-Panareda, A. (2017): A positive definite tracer mass fixer for high resolution weather and  
1138 atmospheric composition forecasts. [https://www.ecmwf.int/sites/default/files/elibrary/2017/17914-positive-definite-tracer-](https://www.ecmwf.int/sites/default/files/elibrary/2017/17914-positive-definite-tracer-mass-fixer-high-resolution-weather-and-atmospheric-composition.pdf)  
1139 [mass-fixer-high-resolution-weather-and-atmospheric-composition.pdf](https://www.ecmwf.int/sites/default/files/elibrary/2017/17914-positive-definite-tracer-mass-fixer-high-resolution-weather-and-atmospheric-composition.pdf).

1140

1141 Diamantakis, M. and Flemming, J. (2014): Global mass fixer algorithms for conservative tracer transport in the ECMWF  
1142 model, *Geosci. Model Dev.*, 7, 965–979, <https://doi.org/10.5194/gmd-7-965-2014>.  
1143

1144 Dias, J., M. Gehne, G. N. Kiladis, N. Sakaeda, P. Bechtold and T. Haiden, 2018: Equatorial waves and the skill of NCEP and  
1145 ECMWF forecast systems. *Mon. Wea. Rev.* 146, 1763-1784. <https://doi.org/10.1175/MWR-D-17-0362.1>  
1146

1147 ECMWF (2023a): ECMWF IFS Documentation CY48R1 – Part III: Dynamics and Numerical Procedures. Reading, UK:  
1148 ECMWF, <https://doi.org/10.21957/26f0ad3473>, 2023.  
1149

1150 ECMWF (2023b): ECMWF IFS documentation CY48R1 – Part IV Physical processes. Reading, UK: ECMWF,  
1151 <https://doi.org/10.21957/02054f0fbf>, 2023.  
1152

1153 ECMWF (2023c): ECMWF IFS Documentation CY48R1 – Part VII: ECMWF Wave Model. Reading, UK: ECMWF,  
1154 <https://doi.org/10.21957/cd1936d846>, 2023.  
1155

1156 ECMWF News Item: [https://www.ecmwf.int/en/about/media-centre/news/2022/nextgems-probes-km-scale-resolutions-](https://www.ecmwf.int/en/about/media-centre/news/2022/nextgems-probes-km-scale-resolutions-integrated-forecasting-system/)  
1157 [integrated-forecasting-system/](https://www.ecmwf.int/en/about/media-centre/news/2022/nextgems-probes-km-scale-resolutions-integrated-forecasting-system/), last access: 4 January 2024, October 2022.

1158  
1159 Engwirda, D.: JIGSAW-GEO (1.0): locally orthogonal staggered unstructured grid generation for general circulation  
1160 modelling on the sphere, *Geosci. Model Dev.*, 10, 2117–2140, <https://doi.org/10.5194/gmd-10-2117-2017>, 2017.  
1161  
1162 Fielding, M. D., S. A. K. Schäfer, R. J. Hogan, and R. M. Forbes (2020). “Parametrizing cloud geometry and its application  
1163 in a subgrid cloud-edge erosion scheme”. In: *Quarterly Journal of the Royal Meteorological Society* 146.729, pp. 1651–  
1164 1667. <https://doi.org/10.1002/qj.3758>.

1165 Forbes, R. M. and Tompkins, A. M. (2011). An improved representation of cloud and precipitation. *ECMWF Newsletter No.*  
1166 129, pp. 13-18.

1167 Forbes, R. M., Tompkins, A. M. and Untch, A. (2011). A new prognostic bulk microphysics scheme for the IFS. *ECMWF*  
1168 *Tech. Memo. No.* 649.

1169 Frenger, I., Gruber, N., Knutti, R. et al. Imprint of Southern Ocean eddies on winds, clouds and rainfall. *Nature Geosci* 6,  
1170 608–612 (2013). <https://doi.org/10.1038/ngeo1863>  
1171

1172 Gao, K., Harris, L., Bender, M., Chen, J.-H., Zhou, L., & Knutson, T. (2023). Regulating fine-scale resolved convection  
1173 in high-resolution models for better hurricane track prediction. *Geophysical Research Letters*, 50, e2023GL103329.  
1174 <https://doi.org/10.1029/2023GL103329>  
1175

1176 Garfinkel, C. I., Gerber, E. P., Shamir, O., Rao, J., Jucker, M., White, I., & Paldor, N. (2022). A QBO cookbook:  
1177 Sensitivity of the quasi-biennial oscillation to resolution, resolved waves, and parameterized gravity waves. *Journal of*  
1178 *Advances in Modeling Earth Systems*, 14, e2021MS002568. <https://doi.org/10.1029/2021MS002568>  
1179

1180 Goessling, H. F., S. Tietsche, J. J. Day, E. Hawkins, and T. Jung (2016), Predictability of the Arctic sea ice edge,  
1181 *Geophys. Res. Lett.*, 43, 1642–1650, DOI:10.1002/2015GL067232.  
1182

1183 Griffies, S. M., and Coauthors, 2015: Impacts on Ocean Heat from Transient Mesoscale Eddies in a Hierarchy of Climate  
1184 Models. *J. Climate*, 28, 952–977, <https://doi.org/10.1175/JCLI-D-14-00353.1>.  
1185

1186 Gutjahr, O., Jungclaus, J. H., Brüggemann, N., Haak, H., and Marotzke, J.: Air-sea interactions and water mass  
1187 transformation during a katabatic storm in the Irminger Sea. *Journal of Geophysical Research: Oceans*, 127,  
1188 e2021JC018075. <https://doi.org/10.1029/2021JC018075>, 2022.

1189  
1190 Hersbach H, Bell B, Berrisford P, et al. (2020). The ERA5 global reanalysis. *Q J R Meteorol Soc.* 146: 1999–2049.  
1191 <https://doi.org/10.1002/qj.3803>  
1192  
1193 Hewitt, H., Fox-Kemper, B., Pearson, B. et al. The small scales of the ocean may hold the key to surprises. *Nat. Clim.*  
1194 *Chang.* 12, 496–499 (2022). <https://doi.org/10.1038/s41558-022-01386-6>.  
1195  
1196 Hogan, R. J., and A. Bozzo, 2018: A flexible and efficient radiation scheme for the ECMWF model. *J. Adv. Modeling Earth*  
1197 *Sys.*, 10, 1990–2008, <https://doi.org/10.1029/2018MS001364>  
1198  
1199 Hohenegger, C., Korn, P., Linardakis, L., Redler, R., Schnur, R., Adamidis, P., Bao, J., Bastin, S., Behraves, M., Bergemann,  
1200 M., Biercamp, J., Bockelmann, H., Brokopf, R., Brüggemann, N., Casaroli, L., Chegini, F., Datsaris, G., Esch, M., George,  
1201 G., Giorgetta, M., Gutjahr, O., Haak, H., Hanke, M., Ilyina, T., Jahns, T., Jungclaus, J., Kern, M., Klocke, D., Kluff, L., Kölling,  
1202 T., Kornbluh, L., Kosukhin, S., Kroll, C., Lee, J., Mauritsen, T., Mehlmann, C., Mieslinger, T., Naumann, A. K., Paccini, L.,  
1203 Peinado, A., Praturi, D. S., Putrasahan, D., Rast, S., Riddick, T., Roeber, N., Schmidt, H., Schulzweida, U., Schütte, F., Segura,  
1204 H., Shevchenko, R., Singh, V., Specht, M., Stephan, C. C., von Storch, J.-S., Vogel, R., Wengel, C., Winkler, M., Ziemann, F.,  
1205 ICON-Sapphire: simulating the components of the Earth System and their interactions at kilometer and subkilometer scales,  
1206 *Geosci. Model Dev.*, <https://doi.org/10.5194/gmd-16-779-2023>, 2023.  
1207  
1208 Hutter, N., Bouchat, A., Dupont, F., Dukhovskoy, D., Koldunov, N., Lee, Y. J., et al. (2022). Sea Ice Rheology Experiment  
1209 (SIREx): 2. Evaluating linear kinematic features in high-resolution sea ice simulations. *Journal of Geophysical Research:*  
1210 *Oceans*, 127, e2021JC017666. <https://doi.org/10.1029/2021JC017666>  
1211  
1212 Hallberg, R.: Using a resolution function to regulate parameterizations of oceanic mesoscale eddy effects, *Ocean Modelling*,  
1213 *Volume 72*, 2013, Pages 92–103, ISSN 1463-5003, <https://doi.org/10.1016/j.ocemod.2013.08.007>.  
1214  
1215 Hannah, W. M., & Maloney, E. D. (2011). The role of moisture–convection feedbacks in simulating the Madden–Julian  
1216 oscillation. *Journal of Climate*, 24(11), 2754–2770.  
1217  
1218 Hogg, A. McC., Meredith, M. P., Chambers, D. P., Abrahamsen, E. P., Hughes, C. W., and Morrison, A. K.(2015), Recent  
1219 trends in the Southern Ocean eddy field, *J. Geophys. Res. Oceans*, 120, 257–267, doi:10.1002/2014JC010470.  
1220  
1221 Hortal, M. (2002) The development and testing of a new two-time-level semi-Lagrangian scheme (SETTLS) in the ECMWF  
1222 forecast model. *Quarterly Journal of the Royal Meteorological Society*, 128, 1671– 1687.

1223 IFS nextGEMS cycle 2 4km 1-year simulation. <https://dx.doi.org/10.21957/1n36-qg55>, 2022.

1224 Johnson, S. J., Stockdale, T. N., Ferranti, L., Balmaseda, M. A., Molteni, F., Magnusson, L., Tietsche, S., Decremer, D.,  
1225 Weisheimer, A., Balsamo, G., Keeley, S. P. E., Mogensen, K., Zuo, H., and Monge-Sanz, B. M.: SEAS5: the new ECMWF  
1226 seasonal forecast system, *Geosci. Model Dev.*, 12, 1087–1117, <https://doi.org/10.5194/gmd-12-1087-2019>, 2019.

1227 Jones PW. 1999. First- and second-order conservative remapping schemes for grids in spherical coordi- nates. *Mon. Wea. Rev.*  
1228 127: 2204–2210.

1229 Judt, F., Klocke, D., Rios-Berrios, R. et. al. 2021: Tropical Cyclones in Global Storm-Resolving Models, *JMSJ*, II, 2021-029.  
1230 <https://doi.org/10.2151/jmsj.2021-029>  
1231

1232 Judt, F., and R. Rios-Berrios, 2021: Resolved convection improves the representation of equatorial waves and tropical rainfall  
1233 variability in a global nonhydrostatic model. *Geophys. Res. Lett.*, 48, e2021GL093265,  
1234 <https://doi.org/10.1029/2021GL093265>.  
1235

1236 Jung, T., and Coauthors, 2012: High-Resolution Global Climate Simulations with the ECMWF Model in Project Athena:  
1237 Experimental Design, Model Climate, and Seasonal Forecast Skill. *J. Climate*, 25, 3155–3172, [https://doi.org/10.1175/JCLI-  
1238 D-11-00265.1](https://doi.org/10.1175/JCLI-<br/>1238 D-11-00265.1).

1239

1240 Kluyver, T. et al. 2016: Jupyter notebooks – a publishing format for reproducible computational workflows. In *Positioning  
1241 and Power in Academic Publishing: Players, Agents and Agendas*, (eds Loizides, F. & Schmidt, B.) 87–90 (IOS Press, 2016).  
1242

1243 Keeley, S.P.E., Sutton, R.T. and Shaffrey, L.C. (2012), The impact of North Atlantic sea surface temperature errors on the  
1244 simulation of North Atlantic European region climate. *Q.J.R. Meteorol. Soc.*, 138: 1774-1783. <https://doi.org/10.1002/qj.1912>.  
1245

1246 Kodama, C., Ohno, T., Seiki, T., Yashiro, H., Noda, A. T., Nakano, M., et al. (2021). The nonhydrostatic icosahedral  
1247 atmospheric model for CMIP6 HighResMIP simulations (NICAM16-s): Experimental design, model description, and impacts  
1248 of model updates. *Geoscientific Model Development*, 14(2), 795–820. <https://doi.org/10.5194/gmd-14-795-2021>.  
1249

1250 Kodama, C., Yamada, Y., Noda, A. T., Kikuchi, K., Kajikawa, Y., Nasuno, T., et al. (2015). A 20-year climatology of a  
1251 NICAM AMIP-type simulation. *Journal of the Meteorological Society of Japan. Ser. II*, 93(4), 393–424.  
1252 <https://doi.org/10.2151/jmsj.2015-024>.  
1253



1254 Koehler, M., Ahlgrimm, M. and Beljaars, A. (2011). Unified treatment of dry convective and stratocumulus-topped boundary  
1255 layers in the ECMWF model. *Q. J. R. Meteorol. Soc.*, 137, 43-57, <https://doi.org/10.1002/qj.713>  
1256

1257 Koldunov, N. V., Aizinger, V., Rakowsky, N., Scholz, P., Sidorenko, D., Danilov, S., and Jung, T.: Scalability and some  
1258 optimization of the Finite-volume Sea ice–Ocean Model, Version 2.0 (FESOM2), *Geosci. Model Dev.*, 12, 3991–4012,  
1259 <https://doi.org/10.5194/gmd-12-3991-2019>, 2019.  
1260

1261 Koldunov, Nikolay; Kölling, Tobias; Pedruzo-Bagazgoitia, Xabier; Rackow, Thomas; Redler, René; Sidorenko, Dmitry;  
1262 Wieners, Karl-Hermann; Ziemer, Florian Andreas (2023). nextGEMS: output of the model development cycle 3 simulations  
1263 for ICON and IFS. World Data Center for Climate (WDCC) at DKRZ. [https://doi.org/10.26050/WDCC/nextGEMS\\_cyc3](https://doi.org/10.26050/WDCC/nextGEMS_cyc3)  
1264

1265 Kölling, T., Kluft, L., & Rackow, T. (2024). gribscan (v0.0.10). Zenodo. <https://doi.org/10.5281/zenodo.10625189>  
1266

1267 Large, W.G., Yeager, S.G. The global climatology of an interannually varying air–sea flux data set. *Clim Dyn* 33, 341–364  
1268 (2009). <https://doi.org/10.1007/s00382-008-0441-3>  
1269

1270 Liebmann, B., & Smith, C. A. (1996). Description of a complete (interpolated) outgoing longwave radiation dataset. *Bulletin*  
1271 *of the American Meteorological Society*, 77(6), 1275-1277.  
1272

1273 Ling, J., Zhao, Y., & Chen, G. (2019). Barrier effect on MJO propagation by the Maritime Continent in the MJO Task  
1274 Force/GEWEX atmospheric system study models. *Journal of Climate*, 32(17), 5529-5547.  
1275

1276 Loeb, N. G., and Coauthors, 2018: Clouds and the Earth’s Radiant Energy System (CERES) Energy Balanced and Filled  
1277 (EBAF) Top-of-Atmosphere (TOA) Edition-4.0 Data Product. *J. Climate*, 31, 895–918, <https://doi.org/10.1175/JCLI-D-17-0208.1>.  
1278

1279

1280 Loveland, T.R.; Reed, B.C.; Brown, J.F.; Ohlen, D.O.; Zhu, Z.; Young, L.; Merchant, J.W. Development of a global land  
1281 cover characteristics database and IGB6 DISCover from the 1 km AVHRR data. *Int. J. Remote Sens.* 2000, 21, 1303–1330.  
1282

1283 Lott, F. and Miller, M. J. (1997). A new subgrid-scale orographic drag parametrization: Its formulation and testing. *Q. J. R.*  
1284 *Meteorol. Soc.*, 123, 101-127, <https://doi.org/10.1002/qj.49712353704>.  
1285

1286 Lüpkes, C., T. Vihma, G. Birnbaum, and U. Wacker (2008), Influence of leads in sea ice on the temperature of the  
1287 atmospheric boundary layer during polar night, *Geophys. Res. Lett.*, 35, L03805, doi:10.1029/2007GL032461.

1288

- 1289 Macdonald, R. W., Griffiths, R. F., & Hall, D. J. (1998). An improved method for the estimation of surface roughness of  
1290 obstacle arrays. *Atmospheric Environment*, 32(11), 1857–1864. [https://doi.org/10.1016/s1352-2310\(97\)00403-2](https://doi.org/10.1016/s1352-2310(97)00403-2)
- 1291 Madden, R. A., & Julian, P. R. (1972). Description of global-scale circulation cells in the tropics with a 40–50 day period.  
1292 *Journal of Atmospheric Sciences*, 29(6), 1109-1123.
- 1293
- 1294 Malardel, S., Wedi N., Deconinck W., Diamantakis M., Kuehnlein C., Mozdzyński G., Hamrud M., Smolarkiewicz P.: A  
1295 new grid for the IFS. *ECMWF Newsletter* 146:23–28. <https://doi.org/doi:10.21957/zwdu9u5i.>, 2016
- 1296
- 1297 Marti, O., Nguyen, S., Braconnot, P., Valcke, S., Lemarié, F., & Blayo, E. (2021). A Schwarz iterative method to evaluate  
1298 ocean–atmosphere coupling schemes: implementation and diagnostics in IPSL-CM6-SW-VLR. *Geoscientific Model*  
1299 *Development*, 14(5), 2959-2975.
- 1300
- 1301 McNorton, J. R., Arduini, G., Bousserez, N., Agustí-Panareda, A., Balsamo, G., Boussetta, S., et al. (2021). An urban  
1302 scheme for the ECMWF integrated forecasting system: Single-column and global offline application. *Journal of Advances in*  
1303 *Modeling Earth Systems*, 13, e2020MS002375. <https://doi.org/10.1029/2020MS002375>
- 1304
- 1305 McNorton, J., Agustí-Panareda, A., Arduini, G., Balsamo, G., Bousserez, N., Boussetta, S., et al. (2023). An urban scheme  
1306 for the ECMWF Integrated forecasting system: Global forecasts and residential CO2 emissions. *Journal of Advances in*  
1307 *Modeling Earth Systems*, 15, e2022MS003286. <https://doi.org/10.1029/2022MS003286>
- 1308
- 1309 Miyakawa, T., H. Yashiro, T. Suzuki, H. Tatebe, and M. Satoh (2017), A Madden-Julian Oscillation event remotely  
1310 accelerates ocean upwelling to abruptly terminate the 1997/1998 super El Niño, *Geophys. Res. Lett.*, 44, 9489–9495,  
1311 doi:10.1002/2017GL074683.
- 1312
- 1313 Miura, H., Satoh, M., Nasuno, T., Noda, A. T., & Oouchi, K. (2007). A Madden-Julian oscillation event realistically  
1314 simulated by a global cloud-resolving model. *Science*, 318(5857), 1763-1765.
- 1315
- 1316 Mogensen, K. S., Magnusson, L., and Bidlot, J.-R.: Tropical cyclone sensitivity to ocean coupling in the ECMWF coupled  
1317 model, *J. Geophys. Res. Oceans*, 122, 4392–4412, doi:10.1002/2017JC012753., 2017.
- 1318
- 1319 Mogensen, K. S., Keeley, S., and Towers, P. (2012): Coupling of the NEMO and IFS models in a single executable,  
1320 *ECMWF Technical Memorandum*, 673, <https://doi.org/10.21957/rfplwzuol>
- 1321

1322 Morrison, A. K., Hogg, A. McC., England, M. H., Spence, P.: Warm Circumpolar Deep Water transport toward Antarctica  
1323 driven by local dense water export in canyons, *Science Advances*, eaav2516, V6, N18 doi:10.1126/sciadv.aav2516, 2020.  
1324

1325 Mu, L., Nerger, L., Tang, Q., Loza, S. N., Sidorenko, D., Wang, Q., Semmler, T., Zampieri, L., Losch, M., & Goessling H.  
1326 F. (2020). Toward a data assimilation system for seamless sea ice prediction based on the AWI Climate Model. *Journal of*  
1327 *Advances in Modeling Earth Systems*, 12, e2019MS001937. DOI:10.1029/2019MS001937  
1328

1329 Mu, L., Nerger, L., Streffing, J., Tang, Q., Niraula, B., Zampieri, L., Loza, S. L., Goessling, H. F. (2022) Sea-ice forecasts  
1330 with an upgraded AWI Coupled Prediction System. *Journal of Advances in Modeling Earth Systems*, e2022MS003176.  
1331 DOI:10.1029/2022MS003176  
1332

1333 Müller, A., W. Deconinck, C. Kühnlein, G. Mengaldo, M. Lange, N. Wedi, P. Bauer et al., 2019: The ESCAPE project:  
1334 Energy-efficient Scalable Algorithms for Weather Prediction at Exascale. *Geosci. Model Dev.*, 12, 4425–4441,  
1335 <https://doi.org/10.5194/gmd-12-4425-2019>.  
1336

1337 Nogueira, M., Boussetta, S., Balsamo, G., Albergel, C., Trigo, I. F., Johannsen, F., et al. (2021). Upgrading land-cover and  
1338 vegetation seasonality in the ECMWF coupled system: Verification with FLUXNET sites, METEOSAT satellite land  
1339 surface temperatures, and ERA5 atmospheric reanalysis. *Journal of Geophysical Research: Atmospheres*, 126,  
1340 e2020JD034163. <https://doi.org/10.1029/2020JD034163>.  
1341

1342 Orr, A., Bechtold, P., Scinocca, J. F., Ern, M. and Janiskova, M. (2010). Improved middle atmosphere climate and forecasts  
1343 in the ECMWF model through a non-orographic gravity wave drag parametrization. *J. Climate*, 23, 5905-5926.,  
1344 <https://doi.org/10.1175/2010JCLI3490.1>.  
1345

1346 OSI SAF Global sea ice concentration climate data record 1978-2020 (v3.0, 2022), OSI-450-a,  
1347 doi:10.15770/EUM\_SAF\_OSI\_0013. EUMETSAT Ocean and Sea Ice Satellite Application Facility. Data extracted from  
1348 OSI SAF FTP server: year 2020, Arctic and Antarctic data, accessed 03.01.2024  
1349

1350 Overland, J. E., T. B. Curtin, and W. O. Smith Jr. (1995), Preface [to special section on Leads and Polynyas], *J. Geophys.*  
1351 *Res.*, 100(C3), 4267–4268, doi:10.1029/95JC00336.  
1352

1353 Palmer, T. Climate forecasting: Build high-resolution global climate models. *Nature* 515, 338–339 (2014).  
1354 <https://doi.org/10.1038/515338a>

1355 Palmer, T., and Stevens, B. (2019): The scientific challenge of understanding and estimating climate change, PNAS 116  
1356 (49), 24390-24395, <https://doi.org/10.1073/pnas.1906691116>  
1357

1358 Paul, M. J., & Meyer, J. L. (2001). Streams in the urban landscape. *Annual Review of Ecology and Systematics*, 32(1), 333–  
1359 365. <https://doi.org/10.1146/annurev.ecolsys.32.081501.114040>  
1360

1361 Polichtchouk, I., Wedi, N. & Kim, Y.-H.(2021) Resolved gravity waves in the tropical stratosphere: Impact of horizontal  
1362 resolution and deep convection parametrization. *Q J R Meteorol Soc*, 148(742), 233–251. Available from:  
1363 <https://doi.org/10.1002/qj.4202>  
1364

1365 Prein, A. F., Langhans, W., Fossier, G., Ferrone, A., Ban, N., Goergen, K., Keller, M., Tölle, M., Gutjahr, O., Feser, F.,  
1366 Brisson, E., Kollet, S., Schmidli, J., van Lipzig, N. P. M., and Leung, R.: A review on regional convection-permitting  
1367 climate modeling: Demonstrations, prospects, and challenges, *Rev. Geophys.*, 53, 323–361, 2015.  
1368

1369 Pujol, M.-I., Y. Faugère, G. Taburet, S. Dupuy, C. Pelloquin, M. Ablain, and N. Picot, (2016): DUACS DT2014: The new  
1370 multi-mission altimeter data set reprocessed over 20 years. *Ocean Sci.*, 12, 1067–1090, [https://doi.org/10.5194/os-12-1067-](https://doi.org/10.5194/os-12-1067-2016)  
1371 2016

1372 Randall, D. A., and K. Emanuel, 2024: The Weather–Climate Schism. *Bull. Amer. Meteor. Soc.*, 105, E300–E305,  
1373 <https://doi.org/10.1175/BAMS-D-23-0124.1>.

1374 Rackow, T., Sein, D. V., Semmler, T., Danilov, S., Koldunov, N. V., Sidorenko, D., Wang, Q., and Jung, T.: Sensitivity of  
1375 deep ocean biases to horizontal resolution in prototype CMIP6 simulations with AWI-CM1.0, *Geosci. Model Dev.*, 12,  
1376 2635–2656, <https://doi.org/10.5194/gmd-12-2635-2019>, 2019.  
1377

1378 Rackow, T., Danilov, S., Goessling, H.F. et al.: Delayed Antarctic sea-ice decline in high-resolution climate change  
1379 simulations. *Nat Commun* 13, 637, <https://doi.org/10.1038/s41467-022-28259-y>, 2022.  
1380

1381 Rackow, T., Pedruzo-Bagazgoitia, X., & Becker, T. (2023a). Namelist files and settings for multi-year km-scale nextGEMS  
1382 Cycle 3 simulations with IFS-FESOM/NEMO. Zenodo. <https://doi.org/10.5281/zenodo.10221652>  
1383

1384 Rackow, T., Becker, T., Forbes, R., & Fielding, M. (2023b). Source code changes to the Integrated Forecasting System (IFS)  
1385 for nextGEMS simulations. Zenodo. <https://doi.org/10.5281/zenodo.10223577>  
1386

1387 Rackow, T., Hegewald, J., Koldunov, N. V., Mogensen, K., Scholz, P., Sidorenko, D., & Streffing, J. (2023c). FESOM2.5  
1388 source code used in nextGEMS Cycle 3 simulations with IFS-FESOM. Zenodo. <https://doi.org/10.5281/zenodo.10225420>  
1389

1390 Saavedra Garfias, P., Kalesse-Los, H., von Albedyll, L., Griesche, H., and Spreen, G.: Asymmetries in cloud microphysical  
1391 properties ascribed to sea ice leads via water vapour transport in the central Arctic, *Atmos. Chem. Phys.*, 23, 14521–14546,  
1392 <https://doi.org/10.5194/acp-23-14521-2023>, 2023.  
1393

1394 Sámány, D., Valentini, M., Smart, S., Razvan, A., Geier, P., Hawkes, J., Quintino, T.: MultiIO: A framework for message-  
1395 driven data routing for weather and climate simulations. Submitted to Proceedings of the Platform for Advanced Scientific  
1396 Computing Conference, 2024.  
1397

1398 Satoh, M., Stevens, B., Judt, F. et al. Global Cloud-Resolving Models. *Curr Clim Change Rep*5, 172–184 (2019).  
1399 <https://doi.org/10.1007/s40641-019-00131-0>  
1400

1401 Scaife, A. A., Baldwin, M. P., Butler, A. H., Charlton-Perez, A. J., Domeisen, D. I. V., Garfinkel, C. I., Hardiman, S. C.,  
1402 Haynes, P., Karpechko, A. Y., Lim, E.-P., Noguchi, S., Perlwitz, J., Polvani, L., Richter, J. H., Scinocca, J., Sigmond, M.,  
1403 Shepherd, T. G., Son, S.-W., and Thompson, D. W. J.: Long-range prediction and the stratosphere, *Atmos. Chem. Phys.*, 22,  
1404 2601–2623, <https://doi.org/10.5194/acp-22-2601-2022>, 2022.  
1405

1406 Schär, C., and Coauthors, 2020: Kilometer-Scale Climate Models: Prospects and Challenges. *Bull. Amer. Meteor. Soc.*, 101,  
1407 E567–E587, <https://doi.org/10.1175/BAMS-D-18-0167.1>.  
1408

1409 Scholz, P., Sidorenko, D., Gurses, O., Danilov, S., Koldunov, N., Wang, Q., Sein, D., Smolentseva, M., Rakowsky, N., and  
1410 Jung, T.: Assessment of the Finite-volumE Sea ice-Ocean Model (FESOM2.0) – Part 1: Description of selected key model  
1411 elements and comparison to its predecessor version, *Geosci. Model Dev.*, 12, 4875–4899, <https://doi.org/10.5194/gmd-12-4875-2019>, 2019.  
1412  
1413

1414 Schulthess, T. C., P. Bauer, N. Wedi, O. Fuhrer, T. Hoefler, and C. Schär, 2019: Reflect- ing on the goal and baseline for  
1415 exascale computing: A roadmap based on weather and climate simulations. *Comput. Sci. Eng.*, 21, 30–41,  
1416 <https://doi.org/10.1109/MCSE.2018.2888788>.  
1417

1418 Sein, D. V., Koldunov, N. V., Danilov, S., Wang, Q., Sidorenko, D., Fast, I., ... Jung, T. (2017). Ocean modeling on a mesh  
1419 with resolution following the local Rossby radius. *Journal of Advances in Modeling Earth Systems*, 9, 2601–2614.  
1420 <https://doi.org/10.1002/2017MS001099>

1421  
1422 Selivanova, J., Iovino, D., and Cocetta, F.: Past and future of the Arctic sea ice in HighResMIP climate models, EGUsphere  
1423 [preprint], <https://doi.org/10.5194/egusphere-2023-1411>, 2023.

1424  
1425 Sidorenko, D., Goessling, H. F., Koldunov, N. V., Scholz, P., Danilov, S., Barbi, D., et al ( 2019). Evaluation of FESOM2.0  
1426 coupled to ECHAM6.3: Pre-industrial and HighResMIP simulations. *Journal of Advances in Modeling Earth Systems*, 11.  
1427 <https://doi.org/10.1029/2019MS001696>.

1428  
1429 Siebesma, A. P., Soares, P. M., & Teixeira, J. (2007). A combined eddy-diffusivity mass-flux approach for the convective  
1430 boundary layer. *J. Atmos. Sc*, 64(4), 1230-1248, <https://doi.org/10.1175/JAS3888.1>

1431  
1432 Simmons, A. J. and Strüfing, R.: Numerical forecasts of stratospheric warming events using a model with a hybrid vertical  
1433 coordinate, *Q. J. Roy. Meteor. Soc.*, 109, 81–111, <https://doi.org/10.1002/qj.49710945905>, 1983.

1434  
1435 Smart, S., Quintino, T., Quintino, T.: A Scalable Object Store for Meteorological and Climate Data. In *Proceedings of the*  
1436 *Platform for Advanced Scientific Computing Conference*, 1–8, 2017.

1437  
1438 Stephan, C. C., Strube, C., Klocke, D., Ern, M., Hoffmann, L., Preusse, P., & Schmidt, H. (2019). Gravity waves in  
1439 global high-resolution simulations with explicit and parameterized convection. *Journal of Geophysical Research:*  
1440 *Atmospheres*, 124, 4446–4459. <https://doi.org/10.1029/2018JD030073>

1441  
1442 Stephan, C.C., Žagar, N. & Shepherd, T.G.(2021) Waves and coherent flows in the tropical atmosphere: New  
1443 opportunities, old challenges. *Q J R Meteorol Soc*, 147: 2597–2624. Available from: <https://doi.org/10.1002/qj.4109>

1444  
1445 Stevens, B., Sherwood, S.C., Bony, S. and Webb, M.J. (2016), Prospects for narrowing bounds on Earth's equilibrium  
1446 climate sensitivity. *Earth's Future*, 4: 512-522. <https://doi.org/10.1002/2016EF000376>

1447  
1448 Stevens, B., Satoh, M., Auger, L., Biercamp, J., Bretherton, C.S., Chen, X., Düben, P., Judt, F., Khairoutdinov, M., Klocke,  
1449 D., Kodama, C., Kornbluh, L., Lin, S.-L., Putman, W., Shibuya, R., Neumann, P., Röber, N., Vannier, B., Vidale, P.-L.,  
1450 Wedi, N. and Zhou, L. (2019) DYAMOND: the DYnamics of the Atmospheric general circulation Modeled On Non-  
1451 hydrostatic Domains. *Progress in Earth and Planetary Science*, 6(1), 61. <https://doi.org/10.1186/s40645-019-0304-z>.

1452  
1453 Stockdale, TN, Kim, Y-H, Anstey, JA, et al. Prediction of the quasi-biennial oscillation with a multi-model ensemble of  
1454 QBO-resolving models. *Q J R Meteorol Soc*. 2022; 148(744), 1519–1540. <https://doi.org/10.1002/qj.3919>

1455  
1456 Streffing, J., Semmler, T., Zampieri, L., & Jung, T. (2021). Response of Northern Hemisphere Weather and Climate to  
1457 Arctic Sea Ice Decline: Resolution Independence in Polar Amplification Model Intercomparison Project (PAMIP)  
1458 Simulations, *Journal of Climate*, 34(20), 8445–8457. DOI:10.1175/JCLI-D-19-1005.1  
1459  
1460 Streffing, J., Sidorenko, D., Semmler, T., Zampieri, L., Scholz, P., Andrés-Martínez, M., Koldunov, N., Rackow, T.,  
1461 Kjellsson, J., Goessling, H., Athanase, M., Wang, Q., Hegewald, J., Sein, D. V., Mu, L., Fladrich, U., Barbi, D., Gierz, P.,  
1462 Danilov, S., Juricke, S., Lohmann, G., and Jung, T.: AWI-CM3 coupled climate model: description and evaluation  
1463 experiments for a prototype post-CMIP6 model, *Geosci. Model Dev.*, 15, 6399–6427, [https://doi.org/10.5194/gmd-15-6399-](https://doi.org/10.5194/gmd-15-6399-2022)  
1464 [2022](https://doi.org/10.5194/gmd-15-6399-2022), 2022.  
1465  
1466 Suematsu, T., & Miura, H. (2018). Zonal SST difference as a potential environmental factor supporting the longevity of the  
1467 Madden–Julian oscillation. *Journal of Climate*, 31(18), 7549-7564.  
1468  
1469 Takasuka, D., & Satoh, M. (2020). Dynamical roles of mixed Rossby–gravity waves in driving convective initiation and  
1470 propagation of the Madden–Julian oscillation: General views. *Journal of the Atmospheric Sciences*, 77(12), 4211-4231.  
1471  
1472 Takasuka, D., Kodama, C., Suematsu, T., Ohno, T., Yamada, Y., Seiki, T., et al. (2024). How can we improve the seamless  
1473 representation of climatological statistics and weather toward reliable global K-scale climate simulations? *Journal of*  
1474 *Advances in Modeling Earth Systems*, 16, e2023MS003701. <https://doi.org/10.1029/2023MS003701>.  
1475  
1476 Takayabu, Y. N. (1994). Large-scale cloud disturbances associated with equatorial waves Part I: Spectral features of the  
1477 cloud disturbances. *Journal of the Meteorological Society of Japan. Ser. II*, 72(3), 433-449.  
1478  
1479 Taylor, M., Peter M. Caldwell, Luca Bertagna, Conrad Clevenger, Aaron Donahue, James Foucar, Oksana Guba, Benjamin  
1480 Hillman, Noel Keen, Jayesh Krishna, Matthew Norman, Sarat Sreepathi, Christopher Terai, James B. White, Andrew G  
1481 Salinger, Renata B McCoy, Lai-yung Ruby Leung, David C. Bader, and Danqing Wu. 2023. The Simple Cloud-Resolving  
1482 E3SM Atmosphere Model Running on the Frontier Exascale System. In *Proceedings of the International Conference for*  
1483 *High Performance Computing, Networking, Storage and Analysis (SC '23)*. Association for Computing Machinery, New  
1484 York, NY, USA, Article 7, 1–11. <https://doi.org/10.1145/3581784.3627044>  
1485  
1486 Temperton, C., Hortal, M. and Simmons, A.J.: A two-time-level semi-Lagrangian global spectral model. *Quarterly Journal*  
1487 *of the Royal Meteorological Society*, 127, 111– 127. <http://dx.doi.org/10.1002/qj.49712757107>, 2001.  
1488

1489 Tiedtke, M. (1989). A comprehensive mass flux scheme for cumulus parametrization in large-scale models. *Mon. Wea. Rev.*,  
1490 117, 1779-1800, [https://doi.org/10.1175/1520-0493\(1989\)117<1779:ACMFSF>2.0.CO;2](https://doi.org/10.1175/1520-0493(1989)117<1779:ACMFSF>2.0.CO;2).  
1491

1492 Tiedtke, M. (1993). Representation of clouds in large-scale models. *Mon. Wea. Rev.*, 121, 3040-3061,  
1493 [https://doi.org/10.1175/1520-0493\(1993\)121<3040:ROCILS>2.0.CO;2](https://doi.org/10.1175/1520-0493(1993)121<3040:ROCILS>2.0.CO;2).  
1494

1495 Tomita, H., Miura, H., Iga, S.-I., Nasuno, T., & Satoh, M. (2005). A global cloud-resolving simulation: Preliminary results  
1496 from an aqua planet experiment. *Geophysical Research Letters*, 32(8), L08805. <https://doi.org/10.1029/2005gl022459>.  
1497

1498 Treguier, A. M., de Boyer Montégut, C., Bozec, A., Chassignet, E. P., Fox-Kemper, B., McC. Hogg, A., Iovino, D., Kiss, A.  
1499 E., Le Sommer, J., Li, Y., Lin, P., Lique, C., Liu, H., Serazin, G., Sidorenko, D., Wang, Q., Xu, X., and Yeager, S.: The  
1500 mixed-layer depth in the Ocean Model Intercomparison Project (OMIP): impact of resolving mesoscale eddies, *Geosci.*  
1501 *Model Dev.*, 16, 3849–3872, <https://doi.org/10.5194/gmd-16-3849-2023>, 2023.  
1502

1503 Trigo, I.F., Monteiro, I.T., Olesen, F., Kabsch, E.: An assessment of remotely sensed land surface temperature. *J. Geophys.*  
1504 *Res.* 113, 1–12. <https://doi.org/10.1029/2008JD010035>, 2008.  
1505

1506 Untch, A. and Hortal, M.: A finite-element scheme for the vertical discretization of the semi-Lagrangian version of the  
1507 ECMWF forecast model. *Quarterly Journal of the Royal Meteorological Society*, 130, 1505– 1530.  
1508 <http://dx.doi.org/10.1256/qj.03.173>, 2004.  
1509

1510 van Westen, R. M., and Dijkstra, H. A.: Ocean eddies strongly affect global mean sea-level projections. *Sci. Adv.* 7  
1511 , eabf1674(2021). DOI:10.1126/sciadv.abf1674  
1512

1513 Vivoda, J., P. Smolíková, and J. Simarro, 2018: Finite Elements Used in the Vertical Discretization of the Fully  
1514 Compressible Core of the ALADIN System. *Mon. Wea. Rev.*, 146, 3293–3310, <https://doi.org/10.1175/MWR-D-18-0043.1>.  
1515

1516 von Albedyll, L., Hendricks, S., Hutter, N., Murashkin, D., Kaleschke, L., Willmes, S., Thielke, L., Tian-Kunze, X., Spreen,  
1517 G., and Haas, C.: Lead fractions from SAR-derived sea ice divergence during MOSAiC, *The Cryosphere Discuss.* [preprint],  
1518 <https://doi.org/10.5194/tc-2023-123>, in review, 2023.  
1519

1520 Wang, C., Zhang, L., Lee, SK. et al.: A global perspective on CMIP5 climate model biases. *Nature Clim Change* 4, 201–205,  
1521 <https://doi.org/10.1038/nclimate2118>, 2014.  
1522



1523 Wedi, N. P.: Increasing horizontal resolution in numerical weather prediction and climate simulations: Illusion or panacea?,  
1524 Philos. T. Roy. Soc. A, 372, 20130289, <https://doi.org/10.1098/rsta.2013.0289>, 2014.  
1525

1526 Wedi, N.P., Polichtchouk, I., Dueben, P., Anantharaj, V.G., Bauer, P., Boussetta, S., Browne, P., Deconinck, W., Gaudin,  
1527 W., Hadade, I., Hatfield, S., Iffrig, O., Lopez, P., Maciel, P., Mueller, A., Saarinen, S., Sandu, I., Quintino, T. and Vitart, F.  
1528 (2020) A baseline for global weather and climate simulations at 1 km resolution. Journal of Advances in Modeling Earth  
1529 Systems, 12(11). <https://doi.org/10.1029/2020MS002192>.

1530

1531 Wedi, N. P., Bauer, P., Denoninck, W., Diamantakis, M., Hamrud, M., Kuhnlein, C., ... & Smolarkiewicz, P. K. (2015). The  
1532 modelling infrastructure of the Integrated Forecasting System: Recent advances and future challenges. European Centre for  
1533 Medium-Range Weather Forecasts. <https://doi.org/10.21957/thtpwp67e>

1534

1535 Wengel, C., Lee, SS., Stuecker, M.F. et al. Future high-resolution El Niño/Southern Oscillation dynamics. Nat. Clim. Chang.  
1536 11, 758–765 (2021). <https://doi.org/10.1038/s41558-021-01132-4>

1537

1538 Wheeler, M., & Kiladis, G. N. (1999). Convectively coupled equatorial waves: Analysis of clouds and temperature in the  
1539 wavenumber–frequency domain. Journal of the Atmospheric Sciences, 56(3), 374-399.

1540

1541 Wieners, Karl-Hermann; Ziemen, Florian Andreas; Koldunov, Nikolay; Pedruzo-Bagazgoitia, Xabier; Rackow, Thomas;  
1542 Redler, René; Sidorenko, Dmitry; Kölling, Tobias (2023). nextGEMS: output of the model development cycle 2 simulations  
1543 for ICON and IFS. World Data Center for Climate (WDCC) at DKRZ. [https://doi.org/10.26050/WDCC/nextGEMS\\_cyc2](https://doi.org/10.26050/WDCC/nextGEMS_cyc2)

1544 Yano, J.-I. and Wedi, N. P.: Sensitivities of the Madden–Julian oscillation forecasts to configurations of physics in the  
1545 ECMWF global model, Atmos. Chem. Phys., 21, 4759–4778, <https://doi.org/10.5194/acp-21-4759-2021>, 2021.

1546

1547 Zampieri, L., Goessling, H. F., & Jung, T. (2018). Bright prospects for Arctic sea ice prediction on subseasonal time scales.  
1548 Geophysical Research Letters, 45, 9731–9738. DOI: 10.1029/2018GL079394

1549

1550 Zampieri, L., Goessling, H. F., & Jung, T. (2019). Predictability of Antarctic sea ice edge on subseasonal time scales.  
1551 Geophysical Research Letters, 46, 9719–9727. DOI: 10.1029/2019GL084096

1552

1553 Zhang, C. (2013). Madden–Julian oscillation: Bridging weather and climate. Bulletin of the American Meteorological  
1554 Society, 94(12), 1849-1870.

1555

1556 Zsoter E, Arduini G, Prudhomme C, Stephens E, Cloke H. Hydrological Impact of the New ECMWF Multi-Layer Snow  
1557 Scheme. *Atmosphere*. 2022; 13(5):727. <https://doi.org/10.3390/atmos13050727>